

Università degli Studi di Bologna

FACOLTÀ DI SCIENZE MATEMATICHE, FISICHE E NATURALI

Dipartimento di Astronomia

ON THE NATURE OF HIGH FREQUENCY PEAKER

RADIO SOURCES

DOTTORATO DI RICERCA IN ASTRONOMIA

XIX CICLO - FIS/05

Coordinatore Chiar.mo Prof. LAURO MOSCARDINI

Tesi di Dottorato

di:

MONICA ORIENTI

Relatore:

Chiar.mo Prof.

DANIELE DALLACASA

**QUESTA TESI E' STATA SVOLTA
NELL'AMBITO DELLE ATTIVITA' DI RICERCA
DELL' ISTITUTO DI RADIOASTRONOMIA
DELL' ISTITUTO NAZIONALE DI ASTROFISICA
(BOLOGNA)**

Contents

Introduction	3
1 Young radio sources	7
1.1 Radio spectra	8
1.2 Radio morphology	10
1.3 Polarization	15
1.4 Host galaxy morphology	17
1.5 Models	18
1.5.1 The Frustration Scenario	18
1.5.2 The youth scenario	20
2 High Frequency Peakers	23
2.1 Complete samples of CSS and GPS radio sources	24
2.1.1 The bright GPS sample	24
2.1.2 The faint GPS sample	24
2.1.3 The bright CSS sample	25
2.1.4 The faint CSS sample	25
2.2 The Bright HFP sample	26
2.3 Contamination from blazar objects	27
3 Spectral variability	31
3.1 Multi-frequency VLA observations	31
3.2 Spectral analysis	35
3.2.1 Spectral shape	38
3.2.2 Variability	39
3.2.3 Peak frequency	40

4	Morphology	45
4.1	VLBA observations and data reduction	45
4.2	The parsec-scale structure	47
4.2.1	Source images	48
4.2.2	Notes on individual sources	50
4.3	Discussion	67
4.3.1	Radio structure and optical identification	67
4.3.2	Physical parameters	68
5	Polarization properties	73
5.1	Polarization observations and data reduction	74
5.2	Polarization analysis	79
5.2.1	Fractional polarization in HFPs	79
5.2.2	Depolarization and Rotation Measure	83
5.3	Polarimetry and the nature of the radio sources: summary	84
6	Young radio sources and their ISM	87
6.1	Young radio sources and HI absorption	88
6.1.1	WSRT observations of genuine HFPs	89
6.1.2	Results	91
6.1.3	Discussion	97
6.2	Extragalactic hydroxyl: jet-cloud interaction?	100
6.2.1	A WSRT search for OH-1720 MHz in HFPs	101
6.3	The X-ray emission in HFPs: the case of J1511+0518	103
6.4	Very asymmetric CSOs: influence of the ambient medium	105
6.4.1	Observations and data reduction	105
6.4.2	Multi-frequency spectral analysis	108
6.4.3	Constraining the age from the radio spectra	109
6.4.4	The radiative age	114
6.4.5	Influence of the ambient medium	116
7	What are High Frequency Peakers?	119
7.1	A connection between HFP and CSS/GPS sources?	120
7.2	Modeling the evolution of the radio emission	124

7.2.1	A simple self-similar evolution model	125
7.2.2	The source growth in a clumpy medium	127
7.2.3	Model versus observations: a double King-profile?	134
Conclusions		137
Bibliography		143

Introduction

Individual galaxies are the celestial bodies accounting for most of the visible matter in the Universe. Their emission properties are either dominated by their stars or by a significant non-stellar contribution from a central Active Galactic nucleus (AGN). In this work only extragalactic radio sources with powerful radio emission as the Fanaroff-Riley type II are considered.

The knowledge of the physical nature of radio-loud AGN was improved by means of the Unified Models developed in the last few decades (see e.g. Urry & Padovani 1995 for a review). These models predict that the difference among the various classes of AGN is not intrinsic, but depends on orientation effects. All AGN are generally accepted to be powered by the release of gravitational energy in a compact accretion disk surrounding a super-massive black hole. Such emission can be obscured to our view by optically thick circumstellar matter located in a torus close to the central engine. The accretion disk is the base of a relativistic, bipolar outflow of material, which gives origin to two symmetric jets ranging from parsec up to Mega-parsec scales.

Despite many aspects of the AGN phenomenon are currently well established (e.g. the discovery of megamaser emission from various spots in orbital motion on a disk proves the existence of a super-massive black hole of $3.8 \times 10^7 M_{\odot}$ in NGC 4258 (Miyoshi et al. 1995) at the center of the disk), the reason why the radio emission is found only in a small fraction of the AGN population and how such phenomenon evolves interacting with the host galaxy, are still a matter of debate. Indeed, only 10% of the AGN population display a powerful radio emission, which is likely a transient phenomenon in the life of galaxies.

The onset of radio activity is currently thought to be related to a merger and/or accretion events. The radio emission, at least in its first stages, evolves in a quite rich and dense ambient medium which can likely influence its growth.

Ideal targets to understand such phenomena are the young radio sources.

Since the orientation is fundamental to accurately determine the radio properties, in this work “young radio source” and “young radio galaxy” are used in an equivalent way, although quasar objects are not rejected *a-priori*.

In the early-stage of the radio source evolution, the jet has to make its way through the dense medium (likely coming from the merger which possibly triggered the radio emission) that surrounds the nucleus, before expanding within the interstellar matter of the host galaxy, and then plunging into the intergalactic medium to eventually originate the extended radio source population (i.e. Fanti et al. 1995).

The evolutionary stage of powerful radio sources can be related to their intrinsic linear sizes (Baldwin 1982).

The number of powerful and compact ($< 1''$) radio sources is rather conspicuous in all modern catalogues at centimeter-wavelengths. However, not all these objects are *intrinsically* small. A fraction of apparently compact sources are foreshortened by projection, when the relativistic jet happens to be aligned to the line of sight, making the source appear brighter as a consequence of Doppler boosting.

It is easy to see that the selection of a sample of intrinsically compact objects, is essential to study the physical nature of young radio sources.

The aim of this thesis is:

- The selection of a sample of genuine young radio sources, without any contamination from beamed objects;
- The study of the ambient medium in which genuine young radio sources evolve, to investigate whether the environment can play an important role on the fate of the radio emission;
- The development of a self-similar evolution model of the radio emission growth which takes into account both the characteristic of the radio source itself, and the properties of the surrounding environment.

The outline of the thesis is the following:

- **Chapter 1** provides a detailed description of the characteristics of young radio sources;

- **Chapter 2** describes the characteristics of the starting sample of sources analyzed in this work;
- **Chapter 3** presents simultaneous multi-frequency, low-resolution observations of the sample, carried out at different epochs in order to determine the correct radio spectral profile;
- **Chapter 4** presents a multi-frequency, high-resolution (milli-arcsecond) morphological study of the sample;
- **Chapter 5** presents a polarimetric analysis of the sample.
- **Chapter 6** investigates the properties of the Interstellar Medium of the host galaxy in order to understand a possible role played by the environment on the radio source growth;
- **Chapter 7** proposes a new analytical self-similar evolution model of the radio emission growth which takes into account the characteristics of a two-phase plasma made of both a clumpy medium and a smooth gas filling the inter-clump space, and compares the predicted results with the data available.

Chapters 3, 4 and 5 aim at constraining the nature of the sources in the sample, in order to find out possible contaminant objects. Once a sub-sample of genuine young radio sources is identified, we will try to understand the characteristics of the environment surrounding the radio emission, and hence to draw a complete picture able to describe the various stages in the radio source growth, reproducing the observed data.

Throughout all this thesis we define a transparent synchrotron emission as $S \propto \nu^{-\alpha}$, where S is the flux density at the frequency ν and α the spectral index. Furthermore, we assume $H_0 = 71 \text{ km s}^{-1} \text{ Mpc}^{-1}$, $\Omega_M = 0.27$ and $\Omega_\lambda = 0.73$, in a flat Universe.

Chapter 1

Young radio sources

Powerful ($P_{1.4\text{GHz}} > 10^{24}$ W/Hz) and compact ($< 1''$) extragalactic radio sources, with a rising radio spectrum peaking at frequencies between 100 MHz to ~ 1 GHz, represent a significant fraction ($\sim 15\text{--}30\%$) in flux density limited catalogues (Fanti et al. 1990). Depending on the turnover frequency ν_t , they are called either “Compact Steep Spectrum” (CSS; $\nu_t \sim 100\text{--}500$ MHz) or GHz-Peaked Spectrum (GPS; $\nu_t \sim 1$ GHz).

In the '80s, the advent of high resolution interferometry (VLA, VLBI and MERLIN), led to the systematic analysis of samples of such sources. It was found that, when imaged with pc-scale resolution, they often display a symmetric radio structure dominated by hot-spots and mini-lobes, namely a scaled-down version (from 0.1 to ~ 15 kpc) of the powerful, edge-brightened radio galaxies, known as the classical doubles, or Fanaroff-Riley type II (FR II, Fanaroff & Riley 1974).

The reason that makes these sources small, i.e. within the host galaxy, can be found in their early evolutionary stage.

In the early '70s Scheuer (1974) proposed a few models which investigate the physical properties of extragalactic radio sources with a continuous energy supply from a central object.

After a decade Baldwin (1982) pinpointed that the evolutionary tracks of extragalactic radio sources are strongly constrained by the distribution of sources in the Radio Luminosity - Linear Size diagram. He then modified the seminal work of Scheuer introducing the information on the ambient medium available at that time, and gave relations describing the source growth and luminosity change with time.

Phillips & Mutel (1982) studied a large number of “compact doubles” pointing out the similarities with the large size powerful radio sources and excluded the presence

of beaming effects. Taking into account the previous information a complete picture describing the individual source evolution, the *youth scenario* could be drawn: after the onset of the radio activity the relativistic plasma is channeled into two radio jets which start to dig their way through the Interstellar Medium (ISM) of the host galaxy, before plunging into the Intergalactic Medium (IGM), and eventually reaching projected linear sizes of hundreds of kpc, or even more. During its growth the radio source preserves its structure, likely evolving in a self-similar way (Fanti et al. 1995).

The alternative model, the “*frustration scenario*” (van Breugel et al. 1984), postulates that compact radio sources are as old as the extended radio source population ($\sim 10^7$ - 10^8 years), but still on small scales since they are trapped by an unusually dense ambient medium which confines the radio emission preventing its growth.

Nowadays there is evidence that at least the vast majority of CSS/GPS radio sources are young (§1.5.2).

In the following sections I describe in more detail the characteristics of CSS/GPS radio sources.

1.1 Radio spectra

The shapes of the radio spectra are one of the key characteristics defining the class of CSS/GPS sources.

The radio emission of extragalactic radio sources is synchrotron radiation originated by a population of relativistic electrons with a power-law energy particle distribution given by $N(E)dE \propto E^{-\delta}dE$. The radio spectra of most of the extragalactic radio sources are represented by power-laws, where the flux density S is directly related to the frequency according to:

$$S(\nu) \propto \nu^{-\alpha}, \quad (1.1)$$

where the spectral index α depends on the index of the energy distribution of the relativistic particles δ , as

$$\alpha = (1 - \delta)/2.$$

At frequencies well above the spectral peak, the power-law spectrum steepens. At high frequencies synchrotron losses prevail over the continuous injection of new

relativistic particles, causing a break in the spectrum. Such deviation occurs at frequencies higher than the *break frequency* ν_b which depends on the age t_{syn} of the electron population and on the magnetic field B :

$$\nu_b \propto B^{-3} t_{syn}^{-2}$$

As the electron population ages, the break frequency moves to lower and lower frequencies, becoming a strong indicator of the source age.

Several models have been developed to reproduce the evolution of relativistic electrons, and a proper description can be found in Murgia et al. (1999).

In CSS/GPS sources, the power-law spectrum turns over at frequencies lower than the turnover frequency ν_t , between 100 MHz and a few GHz, leading to the characteristic convex shape of the CSS/GPS radio spectra (Fig. 1.1).

The turnover frequency ν_t could be due to Synchrotron Self-Absorption (SSA; Kellerman & Pauliny-Toth 1981), i.e. the radio source becomes opaque to its own radiation, and it is related to the peak flux density S_{max} , to the source angular size θ , and the magnetic field B of the emitting region, by:

$$\nu_t \propto S_{max}^{2/5} \theta^{-4/5} B^{1/5} (1+z)^{1/5}, \quad (1.2)$$

where z is the source redshift. In this case, the flux density below the turnover frequency, i.e. in the optically-thick part of the spectrum, is expected from the theory to increase with $\alpha = -2.5$. However, such value is obtained only if the radio emission originates within a single homogeneous component. When observed with adequate resolution, CSS/GPS radio sources have a relatively complex structure made of several components/regions, each one with its own opacity and turnover frequency. Observations which are not able to resolve the source structure lead to an overall spectrum which is the superposition of the spectra of all the source components, and thus usually does not reproduce the $\alpha = -2.5$ slope.

To explain the spectral turnover, a different mechanism to the SSA has been suggested by Bicknell et al. (1997). In their model, the peak in the radio spectrum is explained in terms of Free-Free Absorption (FFA) by ionized gas produced by a radiative shock surrounding the lobes, induced by the supersonic expansion of the

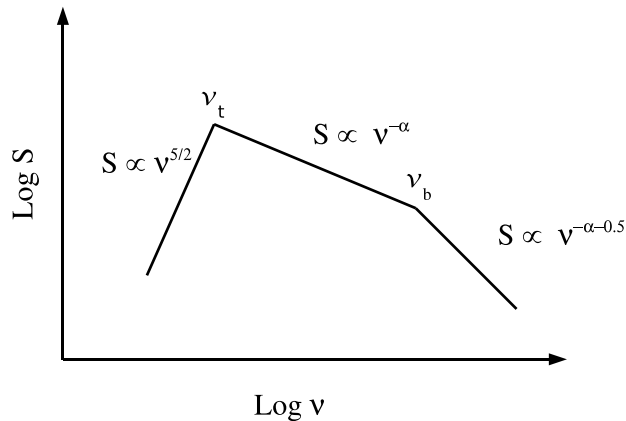


Figure 1.1: Theoretical synchrotron radio spectrum.

lobes themselves.

Although observations (Snellen et al. 2000) seem to support the synchrotron self-absorption as the origin of the turnover frequency, it is also possible that a combination of both mechanisms takes place (Kameno et al. 2000; Mutoh et al. 2002), the FFA becoming more important in the smallest sources.

Statistical studies of various samples of CSS/GPS sources (O’Dea & Baum 1997) have led to the empirical discovery of an anti-correlation between the turnover frequency and the projected linear size l (Fig. 1.2):

$$\nu_t \propto l^{-0.65}.$$

The fact that a simple physical relation exists strongly suggests that the mechanism responsible for the turnover in the spectrum depends on the source size, supporting the idea that it is due to the SSA, once a self-similar source growth has been taken into account.

However, also the FFA model can recover the anti-correlation (Bicknell et al. 1997), leaving the debate on the nature of the spectral turnover still open.

1.2 Radio morphology

The radio emission from extragalactic radio sources spans a wide range of linear sizes, from a few parsecs in the most compact radio sources (i.e. OQ 208) to a few Mpc in the giant radio galaxies (i.e. 3C 236). Although the range of observed sizes covers about 6 orders of magnitude, the morphological structure can be described

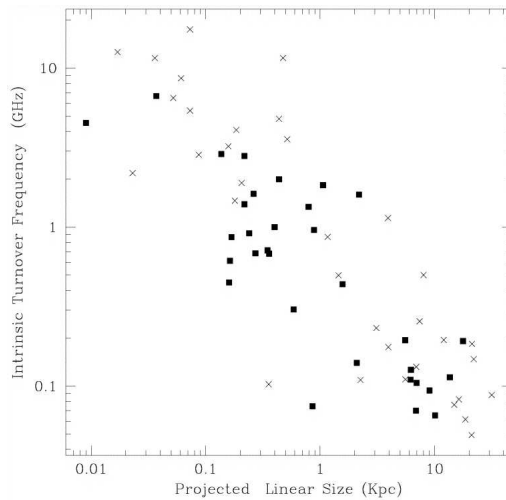


Figure 1.2: The plot from O’Dea (1998) of the turnover frequency vs. projected linear size for the Fanti et al. (1990) CSS sample and the Stanghellini et al. (1998) GPS sample. The quasars are represented by crosses, and the galaxies by solid squares.

by the same ingredients: core, jets, lobes and hot-spots (Fig. 1.3).

The *core* is the central component where relativistic particles, magnetic field and energy originate. It is compact ([sub-]pc-scale) with a flat or inverted radio spectrum.

The *jets* are bipolar outflows, often knotty, which carry out relativistic plasma from the core to the outer regions of the source. The spectral index is typically about $\alpha \sim 0.7$.

The *hot-spot* is the site where the jet interacts with the surrounding ambient medium. It is a compact region (up to a few kpc in the largest sources) with a typical spectral index $\alpha \geq 0.5$ which indicates the presence of particle re-acceleration.

The *lobes* are the place where the relativistic plasma is deposited after its last acceleration in the hot-spot. Their spectral index is ~ 0.7 -1.0, but sometimes even ~ 1.5 as a consequence of strong radiative losses, indicating the presence of old electron populations which are ageing in these structures. It is worth noting that the electron populations located at the inner edges of the lobes in the core direction, have the steepest spectral indices, and thus are older than those found closer to the hot-spots, as a consequence of the outward motion of the hot-spots through the ambient medium.

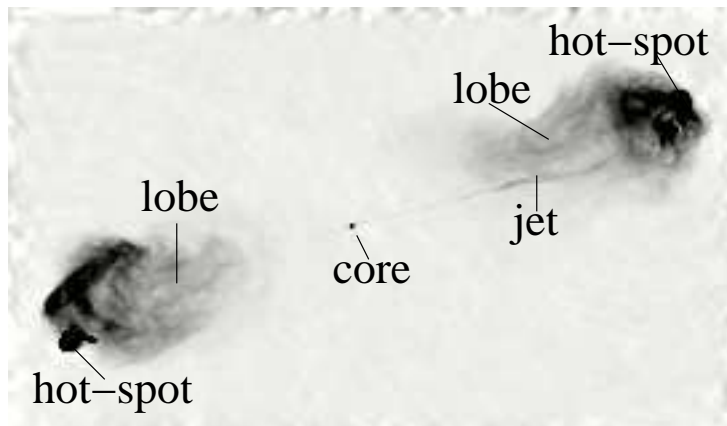


Figure 1.3: The radio source *Cygnus A* (Perley et al. 1984), as an example of the typical morphology of radio galaxies.

Given their compact sizes, the appearance of CSS/GPSs strictly depends on the resolution, the frequency and the sensitivity of the observations, making the correct morphological classification of individual sources rather difficult. Observations at low frequencies with low resolution and dynamic range are not adequate to detect compact and weak components, such as cores, hot-spots and knots in the jets, while high-frequency, low sensitivity measurements may miss low-surface brightness features, such as the outer regions of the lobes. Therefore, a physically meaningful classification requires a range of resolutions and frequencies in order to properly identify the whole source structure and not only a few details of the brightest regions. The first pioneering VLBI works on CSS/GPS sources revealed simple, relatively symmetric structures. Deeper images added new details on their structures and the CSS/GPS morphology can be divided into four main classes (Fig. 1.4; Fanti et al. 1990):

- Doubles: objects with two well-separated components, occasionally with a weak flat-spectrum unresolved component in between, detectable at high frequency only, accounting for a very small fraction ($< 1\%$) of the total flux-density.
- Triples: objects with three well-separated components, not necessarily aligned,

where the central one, usually with a steep spectrum, may contain the source core and the jet base.

- Core-Jets: objects with a straight or bent structure, always with a visible core. The core is located at one end of the source. The characteristics of the jet, such as its linear size and orientation, strictly depend on the resolution of the observations.
- Complex: objects with more complicated structures, which cannot be included in the previous categories.

A significant fraction of the sources classified as “Triple”, with radio jets and lobes on both sides of the core, present very asymmetric morphologies, with different arm-length and flux density ratios (Saikia et al. 2001). CSS/GPSs optically identified with galaxies tend to be (sometimes asymmetric) Doubles and Triples, where their radio emission mainly originates within the mini-lobes and/or the hot-spots. Cores and jets are weak and rare amongst galaxies.

On the other hand, CSS/GPS quasars usually display a Core-Jet or Complex structure, with a single bright jet which dominates the radio emission (Stanghellini 2003).

The existence of two-sided “Double/Triple” CSS/GPS radio sources has two important implication:

- 1) they are in sharp contrast to the one-sided “Core-Jet” structures usually found in powerful compact flat-spectrum sources whose radio emission comes from relativistically boosted jets, but they share the same “compact” property. For these flat-spectrum sources, projection effects substantially foreshorten the source size.
- 2) there is a continuity in morphology between the CSS/GPSs and the large-scale radio sources with similar radio power (FR II), suggesting a self-similar scenario for the source growth.

Statistical study on the CSS sample from Fanti et al. (1990) has shown that CSSs are intrinsically compact sources, and not foreshortened by orientation as in flat-spectrum objects, and represent a young stage in the individual radio source evolution.

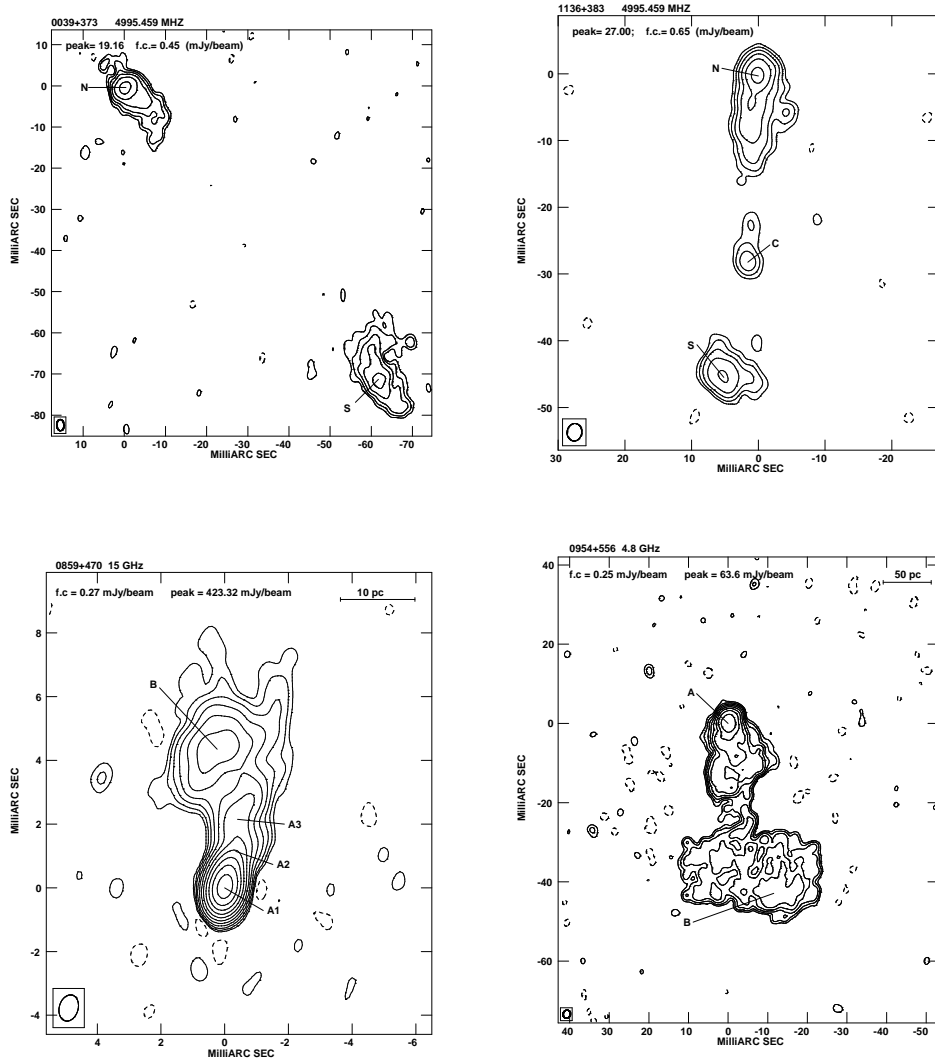


Figure 1.4: Examples of radio source morphologies. *Upper panel:* the Double source B0039+373 (*left*) and the Triple source B1136+383 (*right*) from Orienti et al. (2004). *Lower panel:* The Core-Jet source 0859+470 (*left*) and the Complex source 0954+556 (*right*) from Rossetti et al. (2005).

1.3 Polarization

The synchrotron radiation is intrinsically polarized with the orientation of the electric vector perpendicular to the orientation of the local magnetic field. The fractional polarization we observe depends on the degree of homogeneity of the projected magnetic field and on the spectral index. The maximum degree of polarization expected is:

$$m = \frac{3 + 3\alpha}{5 + 3\alpha} \quad (1.3)$$

which corresponds to $m \sim 70\%$ in case of a homogeneous magnetic field and $\alpha=0.7$. However, depolarization of the synchrotron radiation usually occurs in case of (1) tangled magnetic field in the source, (2) large Faraday Rotation in or around the radio source. If the magnetic field has an isotropic random component within the telescope beam size, this gives rise to a *frequency-independent* depolarization. In case of Faraday Rotation, the measured degree of polarization may be reduced by a differential rotation of the polarization angle across the observing band, implying a *frequency-dependent* depolarization.

Early multi-wavelengths observations have shown that radio sources tend to have very low fractional polarization at decimeter-wavelength, which increases with decreasing wavelength. This monotonic decrement of the polarized emission with wavelength is consistent with Faraday effects. As the radiation passes through a magneto-ionic medium (Faraday Screen) either internal or external to the source, its polarization properties change. The influence produced by the Faraday Screen on the polarization properties depends basically on the characteristics of the magneto-ionic medium, such as the linear sizes of its inhomogeneities (“cells”). When the cells are very small as compared to the linear size, the fractional polarization is strongly related to λ^2 (Burn 1966; Tribble 1991), and little or no rotation is expected.

Given their compact sizes, CSS/GPS entirely resides within the dense Interstellar Medium of the host galaxy. This gas can act as a Faraday Screen causing substantial Faraday Rotation and Depolarization of the synchrotron radiation. These processes are more effective in the innermost and denser regions of the host galaxy, and thus their maximum effects are observed in the smallest sources.

Statistical studies of the CSS/GPS radio sources from the B3-VLA CSS sample

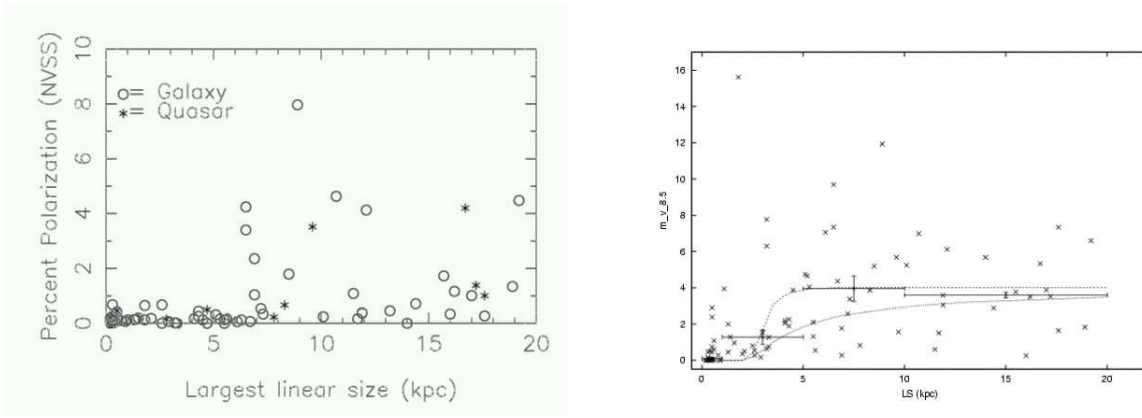


Figure 1.5: The percentage polarization (y -axis) vs the projected linear size (x -axis) at 1.4 GHz (*left panel*; Cotton et al. 2003) and at 8.4 GHz (*right panel*; Fanti et al. 2004) for the sources from the B3-VLA CSS sample (Fanti et al. 2001).

(Fanti et al. 2001) which covers a linear-size range from sub-kpc to several kpc, have led to the discovery of a correlation between the fractional polarization and the source size: the larger the source, the higher the polarized emission is (Fig. 1.5, Cotton et al. 2003; Fanti et al. 2004).

There is also a λ -dependence of this correlation. At 1.4 GHz all the sources in the sample with a projected linear size smaller than 6 kpc are completely depolarized, while those larger than 6 kpc show some degree of polarization up to 8% (Cotton et al. 2003). At higher frequencies, only those sources smaller than 3 kpc are entirely depolarized, while larger sources have substantial fractional polarization, up to 16% (Fanti et al. 2004). Such a result can be explained by either a Faraday Screen with a King-like profile, denser in the inner region and more diluted moving toward the outer regions, or an inhomogeneous magnetic field which is more tangled and stronger in the central regions.

The encounter between a linearly polarized wave and a Faraday Screen produces a rotation of the polarization angle PA χ_λ depending on λ^2 :

$$\Delta\chi = RM \cdot \lambda^2$$

and the Rotation Measure RM is defined as

$$RM(\text{rad m}^{-2}) = 0.81 \int_L n_e B_{\parallel} dl \text{ rad m}^{-2} \quad (1.4)$$

where n_e is the density of the electrons in the magneto-ionic plasma in cm^{-3} , B_{\parallel} the magnetic field component along the line-of-sight in μG , and L the effective path length in parsec.

From multi-wavelength observations of the PA (Saikia & Salter 1988) it has been found that a majority of sources have measured PAs that vary over a wide range of wavelength as

$$\Delta\chi = \chi(\lambda) - \chi(0) = RM\lambda^2$$

where the intrinsic position angle $\chi(0)$ is the zero-wavelength value.

Therefore, the polarization angle (χ) measured at different frequencies permits us to derive the RM as the slope of such a relation. From equation 1.4 we can infer the density of the thermal plasma which produces the Faraday Rotation, once B is known. However, given the low polarization percentage usually displayed by compact CSS/GPS sources, it is not easy to detect polarized emission over a wide range of frequencies, hence to constrain the Rotation Measure. In the few cases where it has been possible to carry out this work, very high ($> 1000 \text{ rad/m}^2$) intrinsic Rotation Measures have been found, implying that the small radio sources are generally surrounded by a very dense ionized medium (Fanti et al. 2004; O’Dea 1998).

The depolarization parameter DP is defined by:

$$DP = \frac{m_{\nu_1}}{m_{\nu_2}} \quad \text{with } \nu_1 < \nu_2 \quad (1.5)$$

where m_{ν_1} and m_{ν_2} are the degrees of polarization at the frequencies ν_1 and ν_2 . $DP \sim 0$ indicates that a strong depolarization of the synchrotron radiation occurs between the two frequencies, while $DP \sim 1$ means that no depolarization is taking place.

1.4 Host galaxy morphology

In contrast to the large amount of information on the radio properties of the GPS/CSS sources, little is known about their optical properties.

CSS/GPS sources are usually associated with objects with $z > 0.1$.

In general, the colors of CSS/GPS galaxies are consistent with those of early-type galaxies with an old stellar population that is either not evolving or passively evolving, i.e. without active star formation (O’Dea et al. 1996a). However, there are a very few examples of merging galaxies (e.g. 4C 12.50; Tadhunter et al. 2005) where induced star formation is taking place. The host galaxies of many CSS/GPS sources exhibit features attributed to mergers such as double nuclei, curved tidal tails and distorted optical morphologies, suggesting that these sources have recently experienced a major merger, involving two or more galaxies (Heckman et al. 1986). The absolute magnitudes found are in the range $-22.0 \leq R_C \leq -24.0$, consistent with the hosts of powerful extended radio galaxies (O’Dea et al. 1996a).

1.5 Models

Since the discovery of the class of CSS/GPS objects, different models to describe their nature have been developed. Such models try to explain the physical properties of this class of radio sources such as their compactness, their high radio luminosity and the significant fraction that they represent in flux density limited catalogues.

So far the proposed models can be sorted into two different categories:

- 1) Old, Confined Sources, i.e. “the frustration scenario”;
- 2) Young evolving Sources, i.e. “the youth scenario”.

1.5.1 The Frustration Scenario

Following the life-cycle of the radio source phenomenon (birth-growth-death), after the onset of the radio emission the radio source linear size grows from very small linear sizes ($< \text{pc}$) to hundreds of kpc. The expected number of radio sources with different dimensions is thus related to the time elapsed since the radio emission has been originated.

It is clear that the number density of intrinsically small radio sources is too large when compared to the population of extended radio sources in flux-limited catalogues. This may be a problem in the “youth scenario” (see § 1.5.2).

The large fraction of small objects is easily explained in case they have ages similar

to the large classical doubles. This requires that CSS/GPS sources are forced to remain compact for a significant fraction of their lifetimes. Given the complex and distorted morphologies found in a few CSS/GPS sources, interpreted as the signature of strong source-cloud interaction, it was suggested that these objects are confined by a particularly dense gas (van Breugel et al. 1984).

Several numerical hydrodynamical simulations (De Young 1993) of a jet propagating either in a smooth medium or in a clumpy one (with cloud radius of 1 pc), have shown that typical CSS/GPS sources can be confined only in the case in which the average density in the ISM is $\sim 1 - 10 \text{ cm}^{-3}$. The most powerful and compact sources would require even higher densities for confinement.

The same results can be obtained by means of a simple one-dimensional ram-pressure argument. The advance speed of the lobes v_l is determined by the equilibrium between the internal pressure p_i and the ram-pressure of the external medium:

$$p_i \sim n_e m_p v_l^2 \quad (1.6)$$

where n_e is the particle density of the external medium, m_p is the proton mass. This allows the determination of the source size as a function of time, once the external density as a function of distance from the centre is known. We assume a typical age of $\sim 2 \times 10^7$ years, as in the larger radio sources. For a range of size of 10 - 15 kpc, the ISM is expected to play the main role in the confinement of the radio emission. A King-type density profile is assumed, as found by X-rays observations in elliptical galaxies (Trinchieri et al. 1986), where $n_e \sim n_0$ is constant up to the core radius (~ 1 kpc), and $n_e \propto r^{-\beta}$ beyond the core radius, with $1.5 \leq \beta \leq 2.0$. This means that to confine CSS/GPS radio sources the density of the external medium must be $n_e \sim 1 - 10 \text{ cm}^{-3}$ or even higher on scales as large as the host galaxy, in agreement with the simulations by De Young (1993).

Are there any observational indication of such a dense ambient medium?

Fanti et al. (1995) have investigated the possibility that during its expansion the source interacts, though occasionally, with the clouds of the Narrow Line Region. In this case the line-luminosities expected are a few orders of magnitude higher than what inferred from the observations.

Different studies in the X-band (O'Dea et al. 2000; Siemiginowska et al. 2005) have not shown any evidence of an anomalously dense and hot ($T \geq 10^7$ K) medium.

Infra-red (IR) observations have been performed by the ISO satellite on a

representative sample of CSS/GPS sources and on a control sample of extended radio galaxies spanning similar ranges of redshift and luminosity (Fanti et al. 2000). From the comparison of the two samples no evidence of different FIR luminosity between the CSS/GPS and extended objects has been found, indicating that CSS/GPS are not frustrated by an abnormally dense cold ambient medium.

1.5.2 The youth scenario

The competing scenario is based on the idea that CSS/GPSs represent an early stage in the individual radio source evolution. After the onset of radio activity, the relativistic plasma is channeled into two bipolar jets which start to dig their way through the Interstellar Medium (ISM) of their host galaxy, before plunging into the Intergalactic Medium (IGM), and reaching projected linear sizes of hundreds of kpc, or even more (Fanti et al. 1995; Readhead et al. 1996; Snellen et al. 2000).

However, it has also been claimed (Alexander 2000; Marecki et al. 2003) that a fraction of young and compact radio sources would die in an early evolutionary stage, without becoming large scale objects. The idea that CSS/GPS are young radio sources is based on their peaked spectra, compact sizes and the symmetric structures similar to those found in large classical doubles (Phillips & Mutel 1982; Carvalho 1985). Furthermore, the lack of any compelling evidence of an ambient medium dense enough to trap the radio source growth for its whole lifetime, indirectly supports the youth scenario.

However, the simplest youth scenario is unable to reproduce the high fraction ($\sim 15\text{-}30\%$) of CSS/GPS found in flux density limited catalogues.

To solve this problem, evolutionary models which take into account changes in both the growth velocity and luminosity are required (i.e. Fanti et al. 1995).

So far strong support to the youth scenario comes both from the determination of hot-spot separation velocity in a dozen of the most compact CSOs (Owsianik & Conway 1998a; Polatidis & Conway 2003), and from the derivation of the radiative age from the analysis of the source integrated spectra (Murgia et al. 1999; Murgia 2003), showing that sources with sizes of $\sim 100\text{-}500$ pc are typically $\sim 10^3$ years old. These two pieces of evidence, in addition to the lack of a dense ambient medium able to confine the source growth, makes the “youth scenario” the currently most

accepted model used to interpret the nature of CSS/GPS radio sources.

A realistic model for the “youth scenario”

In this discussion we describe the model proposed by Fanti et al. (1995) as an example of a self-similar evolution model. This model has many aspects in common with the evolutionary models proposed by other authors (i.e. Readhead et al. 1996; Snellen et al. 2000), and they all follow the original idea from Baldwin (1982).

We assume that the linear size distribution for CSS/GPS is of the type:

$$\frac{dN(LS)}{d(LS)} \propto (LS)^{-m}.$$

As the time passes the linear size LS increases:

$$\frac{dN(LS)}{d(LS)} \propto \frac{dt}{d(LS)}$$

which means:

$$\left[\frac{dN(LS)}{d(LS)} \right]^{-1} \propto v(LS) \propto (LS)^m$$

This implies that the growth velocity increases with the source size, i.e. with the time.

During the radio source evolution the radio luminosity P is described by a power-law of the type:

$$P \propto \left(\frac{r}{r_0} \right)^{-h} \quad (1.7)$$

where r_0 is the core radius which is related to the ambient gas distribution. For $r \gg r_0$ we have $P \propto (LS)^{-h}$.

Furthermore, the luminosity function observed is:

$$\frac{dN(P)}{d(P)} \propto P^{-b}.$$

We obtain that the size distribution at a given observed P is:

$$\frac{dN(LS, P)}{d(LS)} \propto (LS)^{-m} \times (LS)^{hb}.$$

which means:

$$v(LS) \propto (LS)^{hb-m}$$

However the source expansion is slowed down by the interaction with the environment enshrouding the radio emitting plasma. We assume that the ambient medium has a density profile of King type (Trinchieri et al. 1986):

$$n_e \propto n_0 \left(1 + \frac{r^2}{r_0^2}\right)^{-\frac{\beta}{2}} \quad (1.8)$$

where the density up to the core radius r_0 can be considered almost constant $n_e \sim n_0$, while beyond r_0 smoothly decreases as $n_e \propto (LS)^{-\beta}$.

In a ram-pressure model (Eq. 1.6) we find that the source is growing with an expansion velocity

$$v(LS) \propto (LS)^{\frac{\beta}{2}-1} \quad (1.9)$$

Equating the two expressions of the expansion velocity we find:

$$-(hb - m) = \frac{\beta}{2} - 1.$$

From the best fit to the bright CSS sample, Fanti et al. (1995) obtained $b \sim 1.5$ and $m \sim 0.65$. From spectral studies of large-size radio sources, it seems that v is roughly independent from LS, which means that:

$$\frac{\beta}{2} - 1 \sim 0 \sim hb - m$$

which gives $\beta \sim 2$ and $h \sim 0.5$.

If in Eq. 1.7 we consider the values derived above, we find that for sources with $LS \gg r_0$ the luminosity decreases:

$$P \propto (LS)^{-0.5}.$$

A different behavior is expected if the radio emission is embedded within the core radius $LS \ll r_0$, where n_e can be considered constant. In this case, from equation 1.6 we infer that the advance velocity decreases as:

$$v(LS) \propto (LS)^{-1}$$

while the luminosity increases (Eq. 1.7) up to the maximum value reached when $LS = r_0$.

Chapter 2

High Frequency Peakers

The anti-correlation found between the projected linear size and the turnover frequency (O’Dea & Baum 1997) implies that the smallest and thus youngest objects must be sought out among those with the spectral peak above a few GHz. “High Frequency Peaker” radio sources, characterized by the same properties displayed by CSS/GPSs but with turnover frequency well above 5 GHz (Fig. 2.1), are the best candidate to be *newly born* radio sources.

The existence of such *extreme* GPS sources with peak frequency above 10 GHz is expected from all the models on radio source evolution. It is only observational limitations that have prevented their selection. For a source to be recognized as an HFP the characteristic turnover must lie within the spectral range sampled in the surveys used. This constraint occurs only in very few cases with the spectral peak above 5 GHz, i.e. the highest frequency survey available. Furthermore, the timescales of evolution of these extreme sources appear to be of the order of a few tens of years, making their selection rather difficult.

Edge et al. (1996) first noted the existence of these extreme GPS sources with a turnover frequency higher than a few GHz. In particular, they studied the radio source RXJ1459.9+3337 which has the rest-frame turnover frequency at about 30 GHz, and it shows a steady increasing flux density at 5 GHz, in agreement with what expected in the optically thick part of the spectrum of an expanding source.

2.1 Complete samples of CSS and GPS radio sources

The availability of several flux-limited radio surveys with different selection frequencies allowed the construction of various CSS and GPS samples. Catalogues selected at low-frequency with high flux-density limit, such as the 3CR sample (Jenkins et al. 1977), have led to the selection of samples of bright CSS sources. On the other hand, a selection at high frequency, (e.g. 1-Jy sample; Kühr et al. 1981) allows the selection of GPS sources.

In the following discussion I briefly describe the CSS and GPS samples used as reference during this work.

2.1.1 The bright GPS sample

A sample of radio bright GPS sources has been constructed by Stanghellini et al. (1998). As GPS candidates they selected from the 1-Jy catalogue of Kühr et al. (1981) all those sources with declination $> -25^\circ$, $|b| > 10^\circ$ and $S_{5\text{GHz}} > 1$ Jy. Then the sample was cleaned by means of simultaneous multi-frequency VLA and WSRT observations, supplemented with data from the literature. They chose sources with turnover frequency between 0.4 and 6 GHz, and an optically thin spectral index $\alpha_{\text{thin}} > 0.5$.

The final sample consists of 33 objects, of which 19 are identified with galaxies.

2.1.2 The faint GPS sample

Snellen et al. (1998) constructed a sample of faint GPS candidates using the flux density measurements in the optically-thick part of the spectra from the Westerbork Northern Sky Survey (WENSS) at 325 MHz (Rengelink et al. 1997). The sources are located in two regions of the sky: one at $15^{\text{h}} < \text{RA} < 20^{\text{h}}$ and $58^\circ < \text{DEC} < 75^\circ$, which is called the *mini-survey* region (Rengelink et al. 1997), and the other at $4^{\text{h}}00^{\text{m}} < \text{RA} < 8^{\text{h}}30^{\text{m}}$ and $58^\circ < \text{DEC} < 75^\circ$.

The 325-MHz sample was then cross-correlated with the Greenbank 5 GHz survey (Gregory & Condon 1991; Gregory et al. 1996). Only those sources with an inverted spectrum between 325 MHz and 5 GHz were selected. In the case in which data at 609 MHz were also available, an inverted spectrum between 325 and 609 MHz was

used as the selection criterion.

In total, 117 objects with an inverted spectrum were selected as candidate GPS sources.

Additional multi-frequency VLA and WSRT observations were carried out, yielding to a sample of 47 genuine GPS sources with peak frequencies ranging from ~ 500 MHz to more than 15 GHz, and peak flux-density from ~ 30 mJy to ~ 900 mJy.

2.1.3 The bright CSS sample

Fanti et al. (1990) constructed a sample by integrating the 3CR sample (Jenkins et al. 1977) with sources from the Peacock and Wall (PW) sample (1982) which would be stronger than 10 Jy at 178 MHz (the limiting flux-density of the 3CR catalogue), if corrected for the low-frequency absorption by extrapolation of the straight high-frequency part of the spectrum. The resulting representative sample is made of sources with linear sizes < 15 kpc, (corrected) flux-density at 178 MHz > 10 Jy, $P_{178} > 10^{26.5}$, and located in a well-defined area of the sky ($|b| > 10^\circ$ and $\delta > 10^\circ$). The final sample consists of 47 objects.

2.1.4 The faint CSS sample

The B3-VLA CSS sample (Fanti et al. 2001) is a sub-sample of the B3-VLA catalogue (Vigotti et al. 1989). The B3-VLA consists of 1049 objects from the B3 catalogue at 408 MHz (Ficarra et al. 1985) and observed with the VLA at 1.5 GHz in both C and A configuration, with a resolution of ~ 14 and 1.4 arcsecond respectively.

They are located in two well-defined regions of the sky with RA between $23^{\text{h}}00^{\text{m}}$ - $03^{\text{h}}00^{\text{m}}$ and $07^{\text{h}}00^{\text{m}}$ - $15^{\text{h}}00^{\text{m}}$ and DEC $37^\circ 15'$ - $47^\circ 37'$.

All those sources with a projected linear size < 20 kpc and an optically thin spectral index $\alpha > 0.5$ were selected as candidate CSS sources.

In order to obtain more information on the structure of these sources all the candidates CSS were re-observed at 5.0 and 8.5 GHz with the VLA in A configuration. Given the better sensitivity achieved by the higher frequencies (0.4 arcsecond at 5.0 GHz and 0.2 arcsecond at 8.5 GHz), these observations led to the

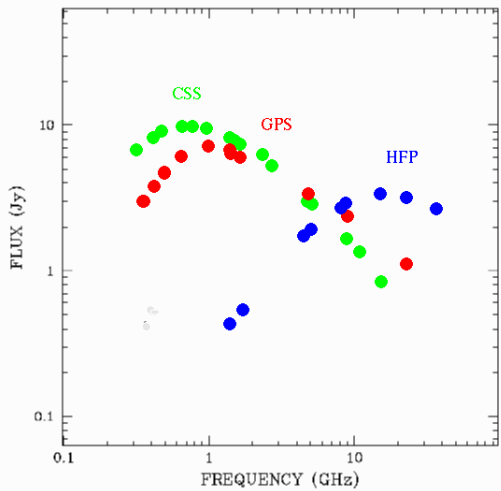


Figure 2.1: The position of the turnover frequency in CSS, GPS and HFP radio sources.

detection of low-brightness extended features in a few sources which then have been rejected from the sample.

The final sample consists of 87 sources.

2.2 The Bright HFP sample

This is the main sample used throughout the whole thesis work.

So far, catalogues of radio sources have been selected at frequencies ranging from 178 MHz (3C sample, Jenkins et al. 1977) to 5 GHz (i.e. S4 survey, Pauliny-Toth et al. 1978). Such low selection frequencies imply that sources with spectral peak occurring at frequencies higher than 5 GHz are largely under-represented in these samples, since their flux density is already declining at 5 GHz and rapidly goes down as the frequency decreases.

Dallacasa et al. (2000) selected a sample of HFP candidates by cross-correlating the Green Bank survey (87GB) at 4.9 GHz (Gregory et al. 1996) and the NRAO VLA Sky Survey (NVSS) at 1.4 GHz (Condon et al. 1998). Only the sources with flux density brighter than 300 mJy at 4.9 GHz and with an inverted synchrotron spectrum steeper than $\alpha = -0.5$ have been selected as HFP candidates. Sources with $|b_{\text{II}}| < 10^\circ$ have been excluded to avoid the galactic plane.

With these selection criteria 102 sources were selected as HFP candidates.

To tackle the contamination of variable sources, such as blazars, all the candidates have been simultaneously observed with the VLA at eight different frequencies from 1.4 to 22 GHz. Only those sources still preserving the convex radio spectrum have been selected.

The final sample consists of 55 objects ($\sim 3\%$ of the 1795 sources exceeding 300 mJy in the 87GB): 10 galaxies with redshifts ranging from 0.02 to 0.67; 34 quasars with higher redshifts, typically between 0.9 and 3.5; 5 BL Lac objects, while 6 sources still lack an optical identification (Dallacasa et al. 2002). In a few objects the optical identification has been carried out on photometric data and no redshift information is available (Dallacasa et al. 2002)

For all the 55 objects of the sample Table 2.1 reports:

- Column 1: source name (J2000);
- Column 2: optical identification. G = Galaxy; Q = Quasar; BL = BL Lac; EF = Empty Field;
- Column 3: redshift;
- Column 4: flux density at 1.4 GHz from the NVSS in mJy;
- Column 5: flux density at 4.9 GHz from the 87GB in mJy;
- Column 6: spectral index between 1.4 and 4.9 GHz;
- Column 7: the turnover frequency (from Dallacasa et al. 2000)

2.3 Contamination from blazar objects

As described in Section 2.2, the Bright HFP sample was constructed on the basis of the radio spectral properties. Such selection tools can introduce a contamination of flat-spectrum beamed radio sources which occasionally match the selection criteria during particular phases of their characteristic variability.

However, for most of their lifetime genuine young radio sources and beamed blazar objects do show very different radio properties.

In the following chapters I will discuss in more detail the differences occurring

Source J2000	ID	z	S _{1.4GHz} mJy	S _{4.9GHz} mJy	$\alpha_{1.4}^{4.9}$	ν_t GHz
J0003+2129	G	0.452	83.7	352	-1.17	6.2
J0005+0524	Q	1.887	127.1	300	-0.70	3.4
J0037+0808	EF		96.9	320	-0.97	4.9
J0111+3906	G	0.668	429.0	1321	-0.92	4.2
J0116+2422	EF		154.8	457	-0.88	4.9
J0217+0144	Q	1.715	750.8	1608	-0.62	>22
J0329+3510	Q	0.50	262.4	545	-0.60	5.5
J0357+2319	Q		176.6	327	-0.50	>22
J0428+3259	G	0.479	152.3	589	-1.10	7.2
J0519+0848	EF		202.8	420	-0.59	>22
J0625+4440	BL		122.7	369	-0.90	14.5
J0638+5933	EF		254.2	482	-0.52	12.9
J0642+6758	Q	3.180	192.9	499	-0.77	3.7
J0646+4451	Q	3.396	452.8	1191	-0.79	15.5
J0650+6001	Q	0.455	472.7	920	-0.54	6.8
J0655+4100	G	0.02156	226.1	425	-0.51	7.8
J0722+3722	Q	1.63	150.2	306	-0.58	4.3
J0927+3902	Q	0.6948	2885.1	7480	-0.78	8.5
J1016+0513	Q		401.7	745	-0.50	7.1
J1045+0624	Q	1.507	157.3	457	-0.87	3.7
J1148+5254	Q	1.632	93.4	304	-0.96	8.7
J1335+4542	Q	2.449	251.0	598	-0.71	4.2
J1335+5844	EF		292.7	820	-0.84	4.9
J1407+2827	G	0.0769	817.1	2421	-0.88	4.9
J1412+1334	EF		196.6	399	-0.58	4.2
J1424+2256	Q	3.626	268.4	503	-0.51	4.0
J1430+1043	Q	1.710	290.0	1236	-1.18	4.9
J1457+0749	BL		234.7	618	-0.79	4.7
J1505+0326	Q	0.411	395.4	991	-0.75	6.2
J1511+0518	G	0.084	60.6	501	-1.72	11.0
J1526+6650	Q	3.02	88.3	417	-1.26	5.8
J1603+1105	BL		195.5	831	-1.18	6.8
J1616+0459	Q	3.197	352.0	918	-0.78	4.1
J1623+6624	G	0.203	156.0	520	-0.98	5.1
J1645+6330	Q	2.379	218.2	444	-0.58	>22
J1717+1917	Q	1.81	124.6	346	-0.83	11.5
J1735+5049	G		432.0	798	-0.50	5.9
J1751+0939	BL	0.322	623.1	2283	-1.06	8.5
J1800+3848	Q	2.092	326.9	722	-0.65	17.8
J1811+1704	BL		132.5	314	-0.70	14.7
J1840+3900	Q	3.095	143.2	476	-0.98	4.5
J1850+2825	Q	2.560	230.7	999	-1.19	8.3
J1855+3742	G		176.1	341	-0.54	4.5

Table 2.1: The sample of HFP candidates (Dallacasa et al. 2000).

Source J2000	ID	z	S _{1.4GHz} mJy	S _{4.9GHz} mJy	$\alpha_{1.4}^{4.9}$	ν_t GHz
J2021+0515	Q		333.5	684	-0.58	3.7
J2024+1718	Q	1.05	279.5	586	-0.60	14.5
J2101+0341	Q	1.013	590.9	1307	-0.65	>22
J2114+2832	Q	2.345	396.7	773	-0.54	9.8
J2123+0535	Q	1.878	794.0	2523	-0.94	>22
J2136+0041	Q	1.932	3473.0	10467	-0.90	4.5
J2203+1007	G		114.6	316	-0.83	4.2
J2207+1652	Q	1.64	208.9	384	-0.50	6.3
J2212+2355	Q	1.125	557.0	1212	-0.63	12.6
J2257+0243	Q	2.081	209.4	426	-0.58	19.5
J2320+0513	Q	0.622	541.9	1180	-0.63	4.1
J2330+3348	Q	1.809	199.2	497	-0.74	5.6

Table 2.1: Continued.

between these two classes of radio sources. Then, by means of such differences contaminant objects which are affecting the Bright HFP sample will be identified and then rejected in order to obtain a selection of objects which are genuine young radio sources.

Chapter 3

Spectral variability

The spectral shape and the absence of significant variability are key elements for the selection of genuine young radio sources. The overall shape of their radio spectra is convex with a peak at high frequencies which is likely due to synchrotron self-absorption (§ 1.1). Also blazar objects, which usually show a flat spectrum may display now and then a convex spectrum as a consequence of an increment of the flux density, when a single, roughly homogeneous and boosted component at the jet base temporarily dominates the radio emission. As this component adiabatically expands, the flux density decreases leading the spectrum back to the usual flat shape.

Therefore multi-epoch observations are necessary to distinguish between these two classes of objects.

Simultaneous multi-frequency VLA observations carried out at different epochs have been used to determine the nature of all the objects of the sample by means of flux density and spectral variability.

3.1 Multi-frequency VLA observations

Multi-frequency VLA observations of the 51 (out of 55) candidate HFPs visible during the allocated observing runs were carried out in different runs from September 2003 and March 2004 (Table 3.1). 25 objects have been observed twice, in order to catch short-period variability. A previous epoch of simultaneous multi-frequency VLA data of 45 out of the 55 objects from the HFP sample, observed in July 2002, was already analyzed and published by Tinti et al. (2005).

Date	Conf	Obs Time	code
Sep 12 2003	AnB	240	a
Sep 13 2003	AnB	240	b
Sep 14 2003	AnB	240	c
Sep 15 2003	AnB	620	d
Jan 22 2004	BnC	120	e
Jan 26 2004	BnC	180	f
Jan 28 2004	BnC	240	g
Jan 30 2004	BnC	120	h
Mar 21 2004	CnD	120	i

Table 3.1: VLA observations and configurations.

The VLA allows the observations of 100 MHz bandwidth separated into two sub-bands (IFs) 50-MHz wide each. They can be tuned independently within the frequency coverage of each receiver which is typically 500 MHz.

The HFP candidates have been observed at 1.465 and 1.665 GHz (the L band), 4.565 and 4.935 (C band), 8.085 and 8.465 GHz (X band), 14.96 GHz (U band), 22.46 GHz (K band) and 43.34 GHz (Q band). In U, K and Q bands the two IFs have been taken adjacent in order to increase the sensitivity.

Each source was observed typically for 50 seconds in each band. For each observing run, about 3 minutes were spent on the primary flux density calibrator either 3C 286 or 3C 48. Secondary calibrators chosen to minimize the telescope slewing time were observed for 1.5 min at each frequency every ~ 20 minutes. This implies that the observations do not have astrometric accuracy. However, accurate radio position (few tens of mas) can be found in the Jodrell Bank VLA Astrometric Survey, JVAS catalogue (Patnaik et al. 1992a; Browne et al. 1998; Wilkinson et al. 1998), for all the sources with the exception of two for which we have the FIRST position, whose accuracy is about a fraction of arcsec.

The data reduction was carried out following the standard procedures for the VLA data, implemented in the NRAO AIPS package. Images for each independent frequency were produced. In order to obtain accurate flux-density measurements in the L band, it was necessary to image several confusing sources falling within the primary beam. During some observing runs strong Radio Frequency Interference

Source	Id.	z	code	S _{1.4}	S _{1.7}	S _{4.5}	S _{4.9}	S _{8.1}	S _{8.4}	S _{15.3}	S _{22.2}	S _{43.2}
J0003+2129	G	0.452	d	100	125	258	262	233	227	146	70	
			e	84	-	251	255	226	220	134	70	16
J0005+0524	Q	1.887	c	166	174	212	206	169	165	122	84	-
			e	168	-	213	207	170	168	129	90	46
J0037+0808	EF		c	98	119	287	290	273	267	197	139	-
			e	95	-	287	293	278	274	210	148	79
J0111+3906	G	0.668	c	509	597	1319	1301	965	918	449	273	111
J0116+2422	EF		c	106	122	245	244	240	226	177	121	-
			e	99	-	258	238	240	225	177	129	-
J0217+0144	Q	1.715	c	577	514	337	326	268	263	244	239	-
			e	571	-	326	315	257	264	256	254	-
J0329+3510	Q	0.5	d	410	443	603	611	586	578	523	447	
			g	563	-	644	625	540	535	468	401	302
J0357+2319	Q		d	116	124	242	255	309	312	382	373	
			g	-	-	185	187	208	210	239	232	212
J0428+3259	G	0.479	d	148	195	513	524	539	531	421	269	
			g	172	199	497	512	522	520	394	253	104
J0519+0848	EF		c	269	263	394	393	373	372	365	336	-
			g	262	273	314	320	322	321	372	382	348
J0625+4440	BL		c	173	186	223	222	219	218	197	174	-
			g	121	131	180	182	187	187	180	161	121
J0638+5933	EF		c	249	315	605	619	680	678	701	653	-
			g	300	325	597	608	649	651	706	643	412
J0642+6758	Q	3.180	c	226	272	436	429	343	332	205	131	-
			g	190	238	405	402	320	312	204	123	44
J0646+4451	Q	3.396	c	444	660	2860	3071	4068	4124	3944	3184	-
			g	586	717	2894	3103	4064	4094	4039	3175	1996
J0650+6001	Q	0.455	c	507	633	1161	1150	994	975	674	467	-
			g	480	626	1150	1106	958	935	798	466	204
J0655+4100	G	0.02156	c	209	232	323	330	354	354	319	268	-
			g	198	233	351	341	369	369	360	307	226
J0722+3722	Q	1.63	d	148	180	199	199	178	174	138	99	
			g	171	188	203	203	176	172	125	83	44
J0927+3902	Q	0.6948	d	2810	3615	9545	9760	10027	9937	8813	7237	
J1016+0513	Q		d	633	711	489	478	428	420	388	327	
J1045+0624	Q	1.507	d	185	245	296	289	268	266	226	152	
J1148+5254	Q	1.632	a	108	-	396	414	460	450	411	277	-
J1335+4542	Q	2.449	a	267	-	821	821	666	646	392	263	-
J1335+5844	EF		a	299	-	745	744	727	726	585	449	-

Table 3.2: The VLA flux density of candidates HFPs. Col. 1: source name (J2000); Col. 2: optical identification; Col. 3: redshift; Col. 4: the observation code, from Tab. 3.1; Col. 5, 6, 7, 8, 9, 10, 11, 12, and 13: VLA flux density in mJy at 1.4, 1.7, 4.5, 4.9, 8.1, 8.4, 15.3, 22.2 and 43.2 GHz respectively.

Source	Id.	z	code	S _{1.4}	S _{1.7}	S _{4.5}	S _{4.9}	S _{8.1}	S _{8.4}	S _{15.3}	S _{22.2}	S _{43.2}
J1407+2827	G	0.0769	b	865	1133	2519	2532	2147	2071	1027	542	-
J1412+1334	EF		b	191	248	346	341	286	277	189	121	-
J1424+2256	Q	3.626	b	371	480	652	637	-	394	247	144	-
J1430+1043	Q	1.710	b	321	423	865	861	780	767	582	473	-
J1505+0326	Q	0.411	b	382	428	608	620	620	610	515	468	-
J1511+0518	G	0.084	b	92	123	569	608	801	811	763	290	-
J1526+6650	Q	3.02	d	109	-	426	440	380	369	211	104	-
J1623+6624	G	0.203	d	154	-	282	281	257	254	191	123	-
			i	162	179	265	263	227	221	164	122	80
J1645+6330	Q	2.379	d	280	-	419	430	464	463	410	273	-
			i	270	288	391	399	430	432	401	322	192
J1717+1917	Q	1.81	h	211	211	232	232	210	208	174	144	124
J1735+5049	G		h	445	-	925	943	898	888	678	485	262
			i	436	479	935	945	886	873	623	408	140
J1751+0939	BL	0.322	h	980	1120	2714	2848	3825	3897	4556	4583	4642
J1800+3848	Q	2.092	f	262	326	793	836	1109	1128	1249	1147	758
J1840+3900	Q	3.095	f	123	147	161	163	165	165	165	164	140
J1850+2825	Q	2.560	f	235	280	1097	1185	1515	1520	1402	1132	605
J1855+3742	G		f	180	181	360	344	215	206	123	86	50
J2021+0515	Q		f	360	442	520	506	407	397	285	206	100
J2024+1718	Q	1.05	f	307	324	594	609	623	619	519	403	242
J2101+0341	Q	1.013	c	483	493	497	498	552	555	704	724	-
			f	431	-	498	508	665	687	954	1031	883
J2114+2832	Q	2.345	d	414	493	612	599	545	535	458	357	-
J2123+0535	Q	1.878	c	-	-	2471	2520	2691	2699	2623	2237	-
			f	2185	2260	2831	2879	3054	3057	3021	2740	1992
J2136+0041	Q	1.932	c	4234	5231	10284	10225	8763	8601	6252	4401	-
			f	3752	4823	10193	10150	8779	8599	6343	4720	2578
J2203+1007	G		c	107	156	315	311	240	231	125	67	21
J2207+1652	Q	1.64	d	177	206	220	224	227	226	214	177	-
			e	268	-	242	248	246	246	218	183	151
J2212+2355	Q	1.125	d	490	576	659	651	629	625	631	547	-
			e	507	-	634	644	682	684	695	624	517
J2257+0243	Q	2.081	c	199	199	280	295	400	408	480	426	-
			e	180	-	291	306	420	432	517	466	330
J2320+0513	Q	0.622	c	526	541	968	1006	1144	1148	1114	936	-
			e	615	-	1060	1076	1098	1094	996	844	616
J2330+3348	Q	1.809	d	274	-	498	511	596	603	620	525	-

Table 3.2: Continued

(RFI) affected the 1.665 GHz data, precluding the flux density measurements for a few sources at such frequency.

The final images were produced after a few phase-only self-calibration iterations, and source parameters were measured by means of the task JMFIT, which performs a Gaussian fit, and TVSTAT which derives the total flux density on the image plane.

The flux density measurements are reported in Table 3.2.

Apart from a few sources which were already known to possess an extended emission (Tinti et al. 2005), the majority of the HFPs are unresolved with the VLA even at the Q band and no morphological information at such scale could be provided.

The r.m.s. noise level on the image plane is not relevant for bright sources as our targets. In the majority of cases, the main uncertainty comes from the amplitude calibration errors, which are (1σ) 3% at L, C and X bands, 5% at U band, and 10% at K and Q bands.

With these new multi-frequency observing runs, 48 out of the 55 sources from the Bright HFP sample have at least three epochs of VLA data. The comparison between each epoch will allow the determination of the variability properties of each single source.

3.2 Spectral analysis

The lack of any detectable spectral variability is one of the key identifying characteristics of young radio sources. In the previous work by Tinti et al. (2005), 7 objects did not show the convex spectrum any longer and they were therefore rejected from the sample. These new epochs of VLA observations, in addition to that from Tinti et al. (2005) and carried out 5 years after the first observing run (Dallacasa et al. 2000), provide new information on the flux-density and spectral shape variability of the candidate HFPs, allowing a better discrimination between genuine young radio sources and blazar objects.

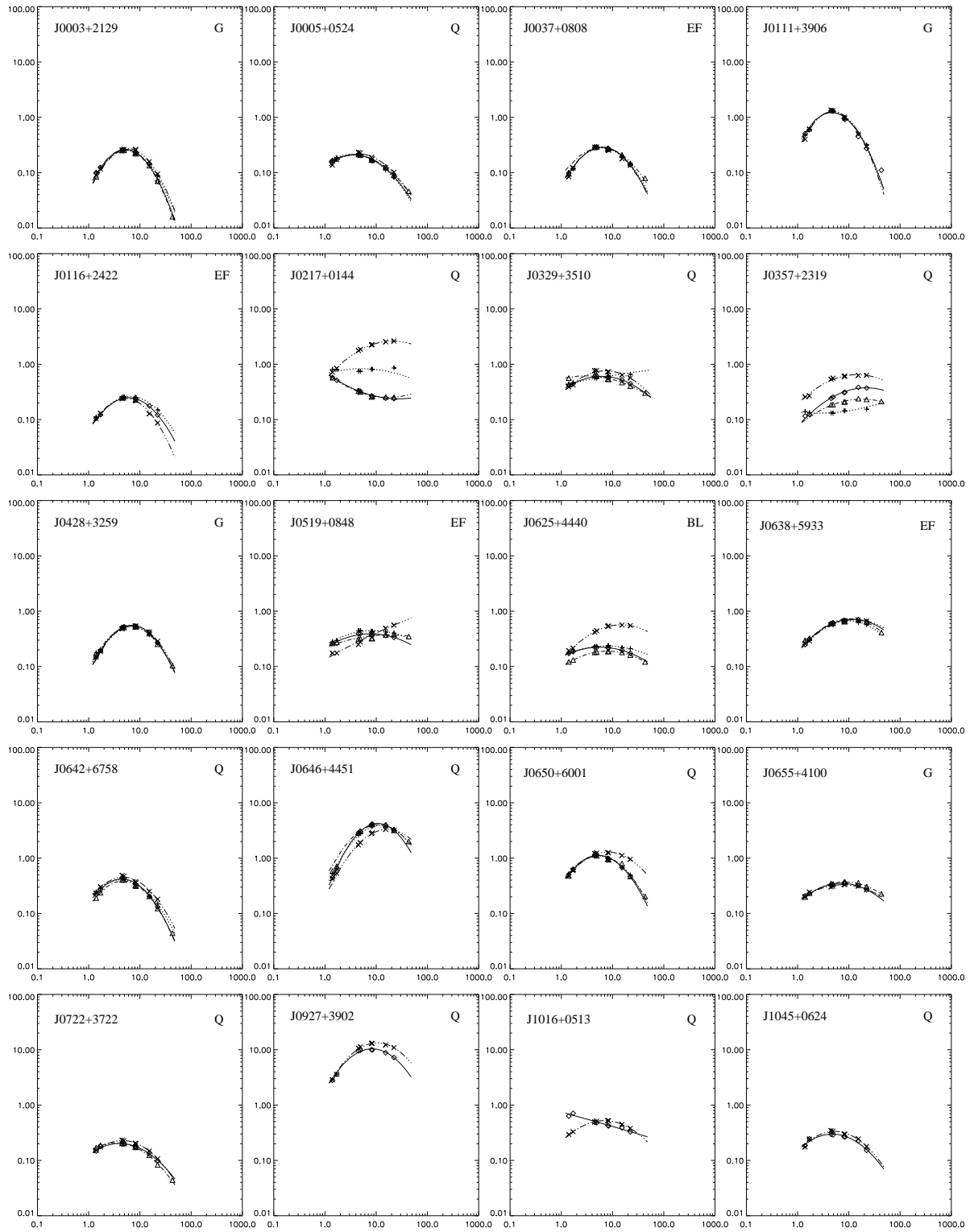


Figure 3.1: Radio spectra of the HFPs: flux density (y -axis) is in Jy, frequency (x -axis) is in GHz. Crosses, plus signs and diamonds refer to the first (Dallacasa et al. 2000), second (Tinti et al. 2005), and this third epoch of simultaneous VLA observations, respectively, while the dashed alternated by three dots, the dotted and the solid lines indicate the corresponding fits. When a fourth epoch is available, it is represented by triangles and a dash-dot line.

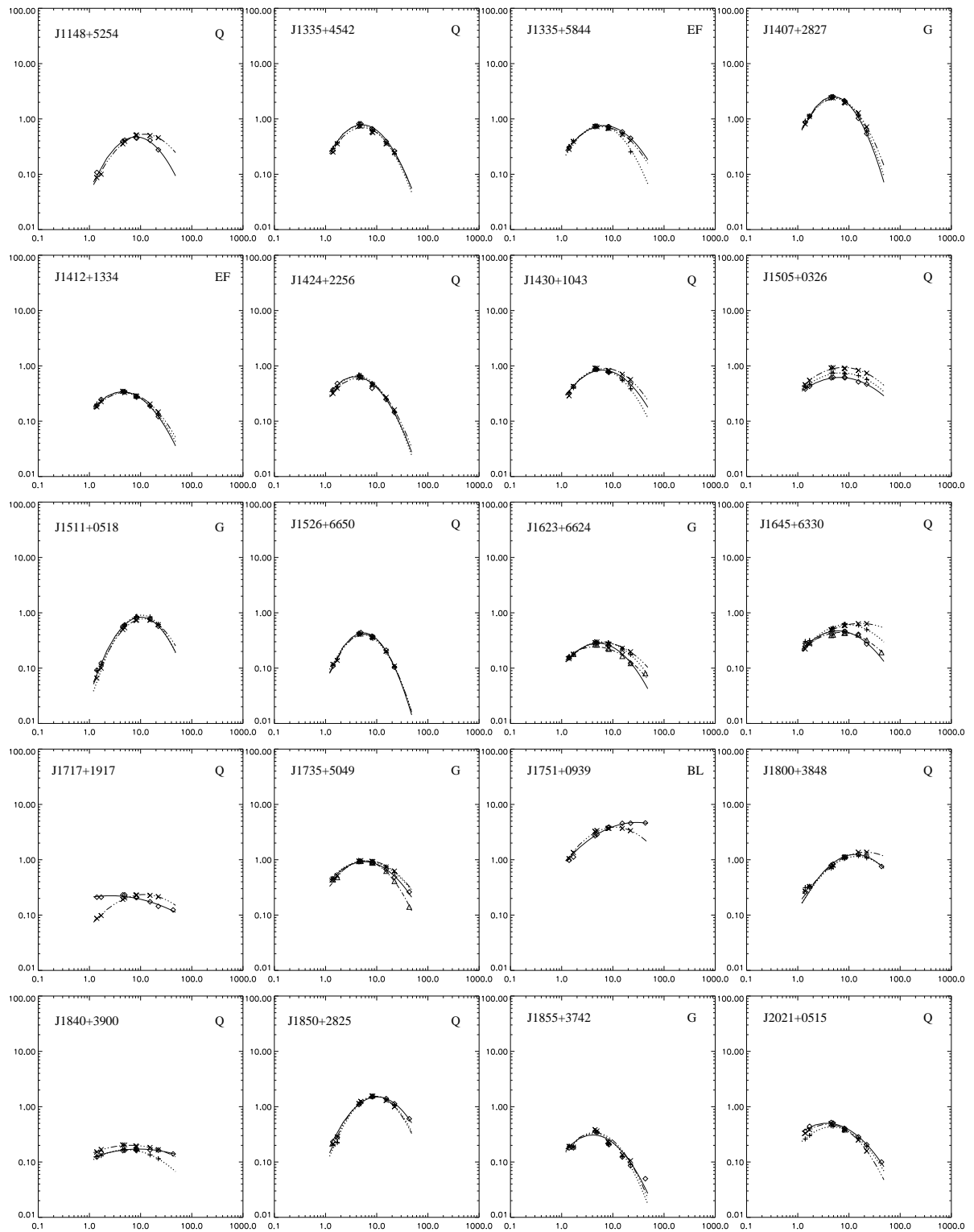


Figure 3.1: Continued.

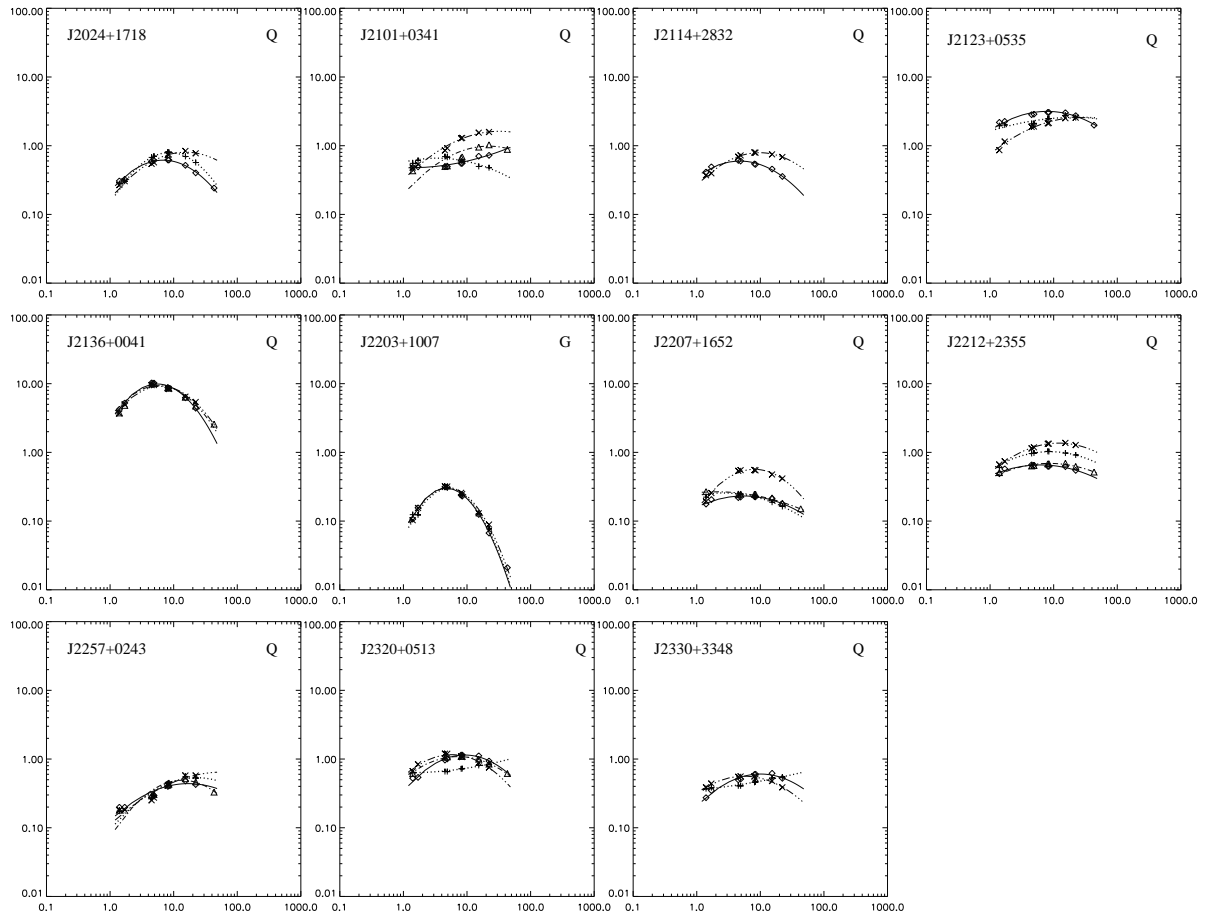


Figure 3.1: Continued.

3.2.1 Spectral shape

One of the main ingredients used to determine whether a radio source actually is a young object is the convex shape of its radio spectrum. On the other hand, blazar objects usually display a flat spectrum.

Following the approach from Dallacasa et al. (2000) and Tinti et al. (2005), the simultaneous radio spectra have been fitted with a mathematical function that provides the flux density and the frequency of the peak. Since most of the sources are optically thin at 43 GHz, the availability of the flux density at such frequency provides very tight constraints on the spectral fit and a better determination of the peak parameters (S_p , ν_p).

Fig. 3.1 shows the radio spectra of all the sources observed at the various

epochs (Oriente, Dallacasa & Stanghellini 2007a). 8 objects (J0217+0144, J0519+0848, J1016+0513, J1717+1917, J1840+3900, J2101+0341, J2207+1652 and J2212+2355), all identified with quasars do not show the convex spectrum anymore. Such sources are labeled “flat” in Columns 4 and 5 of Table 3.3 and are then definitely classified as “blazars”. One of these sources (J0217+0144) was already found with a flat spectrum in the observations carried out by Tinti et al. (2005) and already rejected from the sample of candidate HFPs.

3.2.2 Variability

Given the large Doppler factors which characterize the blazar jets, the flux density variability can substantially modify the observed spectrum of blazars on short timescales.

On the contrary, young radio sources should not display any significant flux-density variability and can be considered the least variable class of extragalactic objects (O’Dea 1998), with a mean variation of $\sim 5\%$ (Stanghellini et al. 2005). Therefore, genuine HFP objects, considered to be newly born radio sources, should not display significant variability.

We analyze the variability of the sources in terms of the quantity:

$$V = \frac{1}{m} \sum_{i=1}^m \sum_{j=1}^n \frac{(S_i - \overline{S}_{i,j})^2}{\sigma_{i,j}^2} \quad (3.1)$$

which is a multi-epoch generalization of the variability index defined by Tinti et al. (2005). S_i is the flux density at the i -th frequency measured at the first and, when available, second epoch of the data presented here, while $\overline{S}_{i,j}$ is the mean value computed averaging the flux density at the i -th frequency at all the available epochs, $\sigma_{i,j}$ is the error on $S_i - \overline{S}_{i,j}$, m the number of sampled frequencies and n the number of available epochs.

Columns 6 and 7 of Table 3.3 report the variability index computed between the new epoch(s) and the mean value obtained by averaging all the available epochs. The variability index V has been computed for each single new epoch, rather than considering all the epochs together. In this case the availability of two distinct values better indicates the presence of flux-density bursts.

A Kolmogorov-Smirnov (KS) test does not detect any significant difference ($>99\%$)

among the variability distributions computed between different epochs. This means that the flux-density of the majority of the observed sources has not changed its frequency dependence with time.

From the comparison of the radio spectra of these 51 observed objects, we find:

- 12 sources with a convex spectrum during the first observations (Dallacasa et al. 2000) show a flat spectrum in at least one of the subsequent observing epochs, and they are rejected from the sample;
- 5 out of the aforementioned 12 sources show a continuous alternation between a flaring-phase with a convex-shape spectrum and a quiescent-phase with a flat spectrum. In particular, during the second-epoch observations (Tinti et al. 2005) the source J2320+0513 was characterized by a flat spectrum, while during the last observing run its spectrum becomes convex again with almost the same flux density displayed during the first epoch (Dallacasa et al. 2000). This example points out the importance of a multi-epoch, multi-frequency flux density monitoring in order to reveal blazar objects.
- 18 sources keep a convex spectrum at the various observing epochs, although with a significant flux density variability ($V > 3$);
- 21 sources preserve the convex spectrum and do not show any significant flux density variability ($V < 3$).

When we compare the variability index V between sources with different optical identification by means of the KS test, we find that there is likely a difference (>90%) between galaxies and quasars, supporting the idea that radio sources identified with galaxies and quasars represent different radio source populations (i.e. Stanghellini et al. 2005).

3.2.3 Peak frequency

So far the anti-correlation (O’Dea & Baum 1997) between the peak frequency and the projected linear size is mainly explained in terms of SSA: as the radio source expands the peak moves to lower frequencies as the result of a decreased energy density within the emitting region.

Source	Morph.	ν_{ep1}	ν_{ep2}	ν_{ep3}	ν_{ep4}	V_{ep1}	V_{ep2}	Var.
J0003+2129	CSO	5.7±0.1	5.4±0.1	5.2±0.9	5.29±0.02	2.67	3.32	HHHH
J0005+0524	CSO	4.13±0.09	3.40±0.09	3.6±0.7	3.5±0.7	1.65	2.16	HHHH
J0037+1109	CSO	5.9±0.1	6.2±0.2	6.2±0.7	6.0±0.7	1.03	1.47	HHHH
J0111+3906	CSO	4.76±0.06	4.68±0.07	4.66±0.19		4.63		HHH
J0116+2422	Un	5.1±0.1	6.3±0.3	6.0±0.8	6.0±1.1	4.93	3.73	HVHH
J0217+0144	Un	18±1	flat	flat	flat	94.72	94.10	HFFF
J0329+3510	CJ	6.7±0.3	flat	6.1±0.3	2.90±0.17	4.31	24.43	HFVV
J0357+2319	Un	12±1	flat	21.8±0.7	17.7±0.8	12.67	42.48	HFHV
J0428+3259	CSO	7.3±0.2	6.8±0.2	6.9±0.5	6.55±0.38	1.12	2.40	HHHH
J0519+0848	Un	>22	7.4±0.6	7.26±0.01	flat	13.28	19.84	HVVF
J0625+4440	Un	13±2	7.4±1.0	5.60±0.63	7.86±0.54	18.18	62.38	HVVV
J0638+5933	CSO	12±2	9.2±0.7	11.35±0.30	10.22±0.20	1.79	3.74	HHHH
J0642+6758	Un	4.5±0.1	4.08±0.08	4.41±0.46	4.41±0.54	0.71	9.18	HVHV
J0646+4451	MR	15±2	11.2±0.6	10.36±0.09	10.65±0.05	19.19	32.44	HVVV
J0650+6001	CSO	7.6±0.3	5.2±0.2	5.23±0.18	5.45±0.15	2.89	3.12	HVHH
J0655+4100	Un	7.8		7.05±0.47	8.27±0.31	0.46	3.73	H-HH
J0722+3722	MR	4.3		4.0±0.7	3.4±0.6	2.67	4.76	H-HH
J0927+3902	CJ	6.9		8.3±0.1		15.45		H-V
J1016+0513	Un	7.1		flat		72.80		H-F
J1045+0624	Un	3.7		4.7±0.5		5.75		H-H
J1148+5254	CSO	8.7		7.9±0.7		9.74		H-V
J1335+4542	CSO	5.1±0.1	4.9±0.1	5.1±0.4		4.64		HHH
J1335+5844	CSO	6.0±0.2	5.5±0.1	6.50±0.34		2.84		HHH
J1407+2827	CSO	5.34±0.05	5.01±0.08	4.95±0.01		2.02		HHH
J1412+1334	Un	4.7±0.1	4.18±0.09	4.3±0.5		0.97		HHH
J1424+2256	Un	4.13±0.07	3.94±0.06	3.7±0.3		8.80		HHV
J1430+1043	MR	6.5±0.2	5.7±0.1	6.2±0.1		1.37		HHH
J1505+0326	Un	7.1±0.4	6.8±0.4	6.6±0.1		30.13		HVV
J1511+0518	CSO	11.1±0.4	10.8±0.4	10.10±0.04		10.24		HVV
J1526+6650	MR	5.7±0.1	5.5±0.1	5.5±0.9		2.04		HHH
J1623+6624	Un	6.0±0.2	6.0±0.2	5.1±0.8	4.5±0.5	0.87	11.16	HHHV
J1645+6330	Un	14±2	10.1±0.7	6.0±0.1	6.8±0.3	12.38	21.61	HHVV
J1717+1917	Un	11.5		flat		81.23		H-F
J1735+5049	CSO	6.4±0.2	6.3±0.3	5.6±0.2	5.6±0.2	0.27	2.07	HHHH
J1751+0939	CJ	8.5		29.02±0.04		8.75		H-V
J1800+3848	Un	17±3	13±1	13.1±0.1		1.92		HHH
J1840+3900	Un	5.7±0.5	5.2±0.4	flat		6.87		HVF
J1850+2825	MR	9.1±0.3	9.5±0.3	9.9±0.4		2.15		HVH
J1855+3742	CSO	4.00±0.07	3.81±0.06	4.0±0.5		1.32		HHH
J2021+0515	CJ	3.75±0.08	4.5±0.1	3.7±0.3		9.94		HVV
J2024+1718	Un	14±2	8.6±0.4	6.6±0.4		14.51		HVV
J2101+0341	Un	17±2	3.7±0.2	flat	>22	28.29	17.00	HVVF
J2114+2832	CJ	9.8		4.8±0.3		34.76		H-V
J2123+0535	CJ	18±4	flat	7.85±0.03		112.74		HFV
J2136+0041	CJ	5.0		5.52±0.01	5.73±0.02	2.88	0.37	H-HH
J2203+1007	CSO	4.86±0.07	5.0±0.1	4.6±0.7		1.94		HHH
J2207+1652	Un	7.4±0.3	3.5±0.3	5.5±0.1	flat	36.01	35.45	HVVF
J2212+2355	Un	13±2	9±1	6.2±0.2	flat	43.10	40.29	HVVF
J2257+0243	Un	>22	>22	17.0±0.4	13.6±0.3	3.27	1.92	HHHH
J2320+0513	Un	5.4±0.2	flat	9.2±0.2	7.3±0.2	23.84	5.75	HFVV
J2330+3348	MR	5.6±0.3	flat	10.0±0.3		18.84		HFV

Table 3.3: Peak frequencies and flux density variability between the different epochs. Col. 1: source name (J2000); Col. 2: Morphological classification from pc-scale information (Orienti et al. 2006a) Col. 3 and 4: peak frequency of the first two epochs (Dallacasa et al. 2000; Tinti et al. 2005); Col. 5 and 6: peak frequency from these new VLA data. Col. 7, 8: flux density variability of the third and, when available, the fourth epoch presented here. Col. 9: The variability classification of the source spectra at the four different epochs available: H= HFP candidate; V= variable; F= flat spectrum.

Table 3.3 reports the peak frequency measured at the various epochs. A KS test does not detect any significant (>99%) difference of the peak frequency at the various epochs. This result is quite expected since the time elapsed between the observing runs is too short to detect a modification in the source spectra of the growing sources. However, if we consider each single object we find that most of them have a smaller ν_p at the subsequent epochs, consistent with the evolution models. The median value of the peak frequency has continuously decreased: $\nu_p \sim 6.9 \pm 0.7$ GHz at the first epoch (Dallacasa et al. 2000), $\nu_p \sim 6.3 \pm 0.9$ GHz at the second epoch (Tinti et al. 2005), and $\nu_p \sim 6.0 \pm 0.5$ GHz at these new epochs.

A comparison between young HFP candidates and blazar objects has shown that the former have a decreasing peak frequency, from a median value of 6.0 ± 0.9 GHz at the first epoch (Dallacasa et al. 2000) to 5.5 ± 0.9 GHz at the subsequent epochs. The latter have a median peak frequency which does not follow a monotonic trend: $\nu_p = 7.4 \pm 1.1$ GHz at the first epoch, $\nu_p = 8.0 \pm 1.5$ GHz at the epoch of Tinti et al. (2005), $\nu_p = 6.2 \pm 1.3$ and 6.8 ± 1.6 GHz at the new observing epochs.

In general the observed peak frequencies $\nu_{p,\text{obs}}$ in galaxies and quasars are similar as a consequence of the selection criteria. However, if we consider the intrinsic peak frequency $\nu_{p,\text{int}}$ a KS test clearly indicates a difference between galaxies and quasars (>99%), which is easily explained in terms of redshift (quasars are found at higher redshifts than galaxies).

Among the 18 sources with $V > 3$ (§ 3.2.2), 8 objects have a peak frequency which shows a remarkable change, although the overall spectrum maintains the convex shape. Five of these sources (the BL Lac J0625+4440 and the quasars J1645+6330, J2024+1718, J2114+2832 and J2257+0243) show a huge decrement in the peak frequency (Orienti, Dallacasa & Stanghellini 2007a).

The size of the emitting region can be estimated by means of two independent methods, either using the relationship from O’Dea (1998)

$$\log \nu_t = -0.21 - 0.65 \log LS,$$

which relates the spectral peak ν_p and the linear size LS, or by means of the synchrotron self-absorption theory (Kellermann & Pauliny-Toth 1981), in which:

$$\theta = B^{\frac{1}{4}} S_p^{\frac{1}{2}} \nu_p^{-\frac{5}{4}} (1+z)^{\frac{1}{4}} \quad (3.2)$$

where B is the magnetic field, S_p is the flux density at the peak frequency and z is the redshift. For the magnetic field we consider the values reported by Orienti et al.

(2006a, § 4.3.2), and obtained assuming equipartition conditions (Pacholczyk 1970). If the magnetic field B is frozen in a homogeneous adiabatically-expanding region, we have

$$B = B_0 \left(\frac{t_0}{t} \right)^2$$

where B_0 is the magnetic field at the epoch t_0 and B at the time $t = t_0 + \Delta T$. Assuming that $\Delta T \ll t_0$ this implies that the value of the magnetic field can be considered constant during the $\Delta T = 5$ years elapsed between the farthest observing runs (typical ages of HFPs being $\sim 10^2$ – 10^3 years).

The increments in size obtained by both ways are in good agreement, and correspond to an expansion velocity $\geq c$, which is clearly unrealistic for unboosted young objects. We conclude that such sources are beamed objects and then rejected as genuine candidate HFPs.

The other object, the BL Lac J1751+0939, shows an increment of the peak frequency (from 8.5 to 29 GHz) which can be interpreted in terms of different knots in the jet that dominate the radio emission at the two epochs.

In order to analyze the spectral shape of the sources from the HFP sample, a “canonical” radio spectrum for sources with either $V < 3$ (Fig. 3.2a) or $V > 3$ (Fig. 3.2b) have been constructed.

Following the work from de Vries et al. (1997), the canonical radio spectra have been obtained normalizing the observed frequencies and flux densities by the source peak frequency and the peak flux density, computed averaging all the epochs:

$$\nu = \frac{1}{m} \sum_{i=1}^m \frac{\nu_i}{\nu_{pi}} \quad (3.3)$$

$$S = \frac{1}{m} \sum_{i=1}^m \frac{S_i}{S_{pi}} \quad (3.4)$$

where ν and S are the average normalized frequency and flux density respectively. ν_i and ν_{pi} are the observed frequency and the observed turnover frequency at the i -epoch, while S_i and S_{pi} the observed flux density and the observed peak flux density at the i -epoch, and m the available epoch.

Sources with $V < 3$ or $V > 3$ display different canonical spectral shape. The former

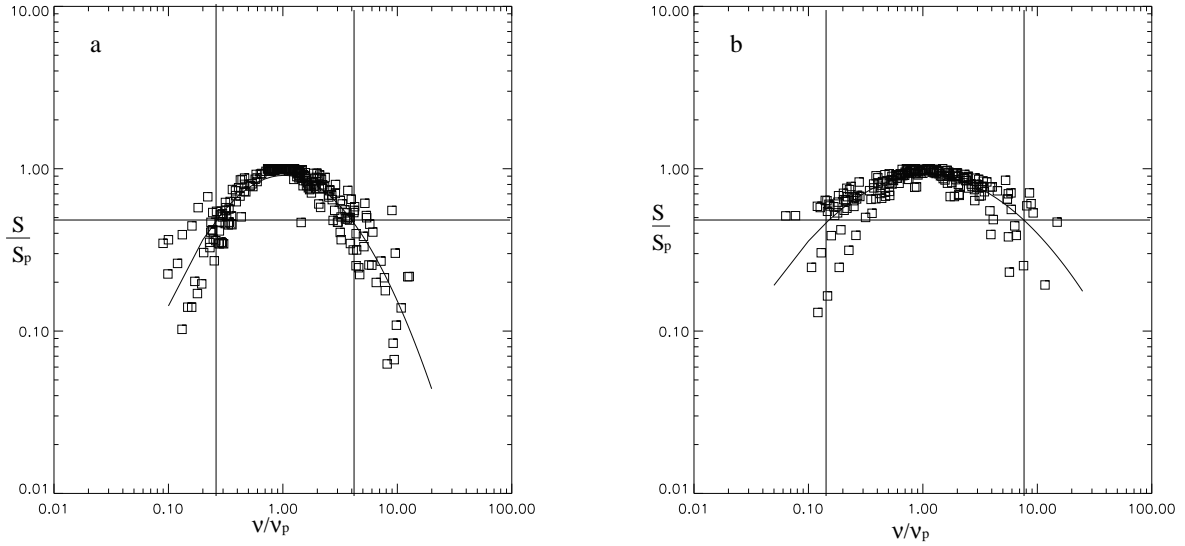


Figure 3.2: Canonical radio spectra computed for radio sources with $V < 3$ (*left panel*) and for radio sources with $V > 3$ (*right panel*). The continuum line indicates the least-square fit to the data. The horizontal line indicates the FWHM and the vertical lines define the corresponding width.

have a quite convex spectrum, with a narrow width (FWHM ~ 1.7) and spectral indices $\alpha_{\text{thick}} \sim -0.9 \pm 0.1$ and $\alpha_{\text{thin}} \sim 0.7 \pm 0.1$. The latter have a flatter spectral shape, with a FWHM ~ 3.6 and spectral indices $\alpha_{\text{thick}} \sim -0.4 \pm 0.1$ and $\alpha_{\text{thin}} \sim 0.4 \pm 0.1$

Chapter 4

Morphology

The pc-scale structure of young radio sources is one of the characteristics which inspired the youth scenario (Phillips & Mutel 1982). They are a scaled-down version of the large (hundreds of kpc) classical Doubles found in catalogues of powerful radio sources like 3C. In young radio sources the emission has a “Double/Triple” structure with a steep spectral index, since it mainly originates from electron populations located in the mini-lobes and/or hot-spots, contrary to what happens in blazar objects where the radio emission mainly comes from regions strictly related to the core and the jet-base, leading their morphology to have a “Core-Jet” structure and a flat/inverted spectral index due to relativistic beaming.

Pc-scale resolution images at two different frequencies in the optically-thin part of the spectra have been obtained for 51 out of the 55 candidate HFPs in order to discriminate the real nature of each source by means of their morphological properties.

The remaining 4 sources have plenty of VLBI observations and their morphological information can be considered complete.

4.1 VLBA observations and data reduction

Pc-scale resolution observations were carried out with the VLBA in 2002 (see Table 4.1) at 8.4, 15.3, 22.2 and 43.2 GHz, with a recording bandwidth of 32 MHz at 128 Mbps. The correlation was performed at the VLBA correlator in Socorro.

The target sources were observed at a pair of frequencies in the optically thin region of their synchrotron spectra, as determined in the VLA observations from Dallacasa

Exp. Code	Date	Obs. time	Notes
BD077A	11 Jan 2002	9h	Erratic T_{sys} values at LA
BD077B	10 Feb 2002	9h	-
BD077C	16 Feb 2002	9h	-
BD077D	02 May 2002	9h	-

Table 4.1: Log of the VLBA observations.

et al. (2000): for example, an object with turnover frequency at 5.0 GHz was observed at 8.4 and 15.3 GHz, while objects with turnover frequency above 15 GHz were observed at 22 and 43 GHz.

Each target was typically observed for 20/30 min at each frequency, spread into 4 to 7 scans at various Hour Angles (HA) in order to have a sufficiently homogeneous uv coverage.

The strong compact sources 3C 454.3, 3C 345 and J2136+0041 (an HFP quasar) were used as fringe finders, and a few more calibration sources (including the HFPs J0927+3902 and J1407+2827) were observed to verify the system performance during the experiments.

All the data reduction has been carried out by means of the NRAO AIPS package. A-priori amplitude calibration was derived by using measurements of the system temperatures and antenna gains. The error on the absolute flux density scale is generally within 5%, while it is about 10% at 43.2 GHz, as estimated from the variation of the gains during the observations.

Fringe fitting was carried out on each source with a short (down to 1 min) solution interval at 22.2 and 43.2 GHz in order to preserve phase coherence. In general all the sources were detected on all baselines, and the data turned out to have a good quality at all the frequencies, with the only exception of J1526+6650 which has not been detected at 43.2 GHz.

During the BD077A observations, the VLBA antenna located in Los Alamos was affected by technical problems that caused the system temperature to have erratic values at 15.3 and 22.2 GHz.

The final radio images were obtained after a number of phase-only self-calibration

iterations, and the source parameters (total flux density and deconvolved sizes) have been measured by means of the task JMFIT for marginally resolved components, and TVSTAT or IMSTAT when a component could not be fitted by a Gaussian profile.

In those cases where multiple components are present, the VLBA total flux density has been derived on the image plane by means of TVSTAT. All the values are reported in Table 4.2, 4.3 and 4.4.

Table 4.2 reports the flux density measured at each frequency for all the observed sources, while in Table 4.3 and 4.4 are reported the physical properties of those sources with a CSO or a Core-Jet morphology respectively.

4.2 The parsec-scale structure

Relatively low dynamic-range images are not the ideal tool to perform a very accurate morphological classification, and this is particularly true for complex sources. However, from short observations it is possible to derive indications on the nature of each source making use of the spectral information provided by the frequency pair data available.

Given the small source size, if compared to the resolution element, the observations are adequate for the purpose of morphological classification.

In these VLBA images thirteen (6 galaxies, 4 quasars and 3 Empty Fields) out of the 51 sources observed show a CSO-like morphology, seven (6 quasars and 1 BL Lac) present a Core-Jet structure and one (the quasar J1424+2256) has multiple images being a well known gravitational lens (Fig. 4.1).

Despite the high resolution achieved by these VLBA images, 30 sources ($\sim 60\%$) are unresolved or marginally resolved at the highest observing frequency. Marginally resolved (MR) are those sources whose largest angular size (LAS) is between 0.5 and 1 beam size at the highest frequency, while “Unresolved” are all the sources whose LAS is smaller than half of the beam size at both frequencies.

We classify as Unresolved 24 objects (2 galaxies, 16 quasars, 3 BL Lacs, and 3 Empty Fields), and Marginally Resolved 6 sources, all identified with quasars. The total spectral index of both Unresolved and Marginally Resolved sources is usually flat or inverted, despite we are observing the optically thin emission of each source as from

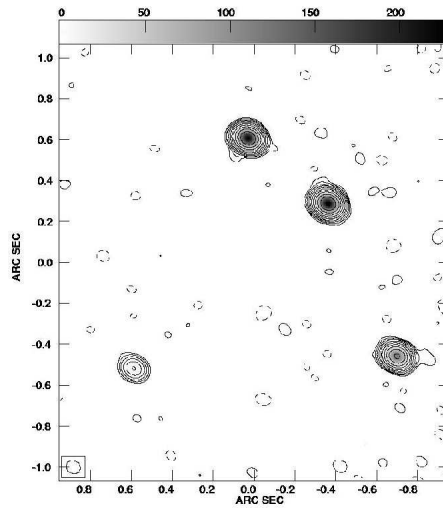


Figure 4.1: The gravitational lens J1424+2256 (Browne et al. 2003).

Dallacasa et al. (2000).

4.2.1 Source images

Full resolution images of the thirteen sources with a CSO-like morphology are presented in Fig. 4.2 and Fig. 4.3, while Fig. 4.4 and 4.5 show instead the images of the objects with a Core-Jet structure. Fig. 4.6 shows the multiple images of the gravitational lens. In general the sources are presented in increasing RA order and images at two frequencies are next to each other, the lowest frequency always on the left panel (Fig. 4.2 and 4.4). For the objects resolved at one frequency only, such image is shown (Fig 4.3 and 4.5). Images for the objects found to be unresolved at both frequencies are not presented.

Noise in the image plane is generally between 0.5 and 1 mJy, except for a few cases where bad weather conditions affected the observations implying substantially higher noise levels, particularly at high frequency.

For each image the following information is provided on the plot itself:

- a) the source name and the observing frequency on the top left corner;
- b) the peak flux density in mJy/beam;
- c) the first contour intensity (*f.c.* in mJy/beam), which is generally 3 times the off-source r.m.s. noise level measured on the image plane; contour levels increase by a factor 2;

Source	z	Id	S _{8.4} VLA mJy	S _{8.4} VLBA mJy	S ₁₅ VLA mJy	S ₁₅ VLBA mJy	S ₂₂ VLA mJy	S ₂₂ VLBA mJy	S ₄₃ VLBA mJy	α	H _{eq} mG	Morph
J0003+2129	0.452	G	227	228	140	131	86	-	-	1.0	17	CSO
J0005+0524	1.887	Q	166	163	111	105	82	-	-	0.8	36	CSO
J0037+0808		EF	262	256	190	173	143	-	-	0.7	31	CSO
J0111+3906	0.668	G										
J0116+2422		EF	248	237	128	173	149	-	-	0.5	68	Un
J0217+0144	1.715	Q	810	-	856	-	838	705	521	0.4	340	Un
J0329+3510	0.50	Q	578	472	659	525	702	-	-	-0.2	48	CJ
J0357+2319		Q	144	-	154	-	168	155	110	0.5	113	Un
J0428+3259	0.479	G	514	-	375	357	263	220		1.3	26	CSO
J0519+0848		EF	430	-	420	-	401	387	349	0.2	128	Un
J0625+4440		BL	238	-	219	-	210	143	60	1.3	167	Un
J0638+5933		EF	667	-	620	-	567	505	369	0.5	72	CSO
J0642+6758	3.180	Q	321	320	203	189	149	-	-	0.9	116	Un
J0646+4451	3.396	Q	3757	-	3691	-	3318	2953	1938	0.6	462	MR
J0650+6001	0.455	Q	964	-	671	650	495	406	-	1.3	27	CSO
J0655+4100	0.02156	G	335	-	313	272	271	214	-	0.6	94	Un
J0722+3722	1.63	Q	198	-	138	170	96	115	-	1.1	55	MR
J0927+3902	0.6948	Q	11859	-	10060	-	8660	-	-	-	-	CJ
J1016+0513		Q	522	-	449	-	379	253	227	0.2	106	Un
J1045+0624	1.507	Q	284	266	238	211	196	-	-	0.3	91	Un
J1148+5254	1.632	Q	512	-	501	355	458	238	-	1.0	106	CSO
J1335+4542	2.449	Q	592	526	359	307	234	-	-	0.9	187	CSO
J1335+5844		EF	671	604	531	449	253	-	-	0.5	17	CSO
J1407+2827	0.0769	G	2050	-	1139	-	604	-	-		-	CSO
J1412+1334		EF	267	251	185	140	130	-	-	1.0	39	Un
J1424+2256	3.626	Q	460	419	251	-	145	-	-		-	Un
J1430+1043	1.710	Q	752	709	546	519	385	-	-	0.6	112	MR
J1457+0749		BL	188	225	141	157	109	-	-	1.1	110	Un
J1505+0326	0.411	Q	710	573	665	509	567	-	-	0.2	420	Un
J1511+0518	0.084	G	861	-	843	693	617	457		1.2	40	CSO
J1526+6650	3.02	Q	341	-	193	-	107	48	-		-	MR

Table 4.2: The VLBA flux density of candidates HFP. Col. 1: source name (J2000); Col. 2: redshift; Col. 3: optical identification from Dallacasa et al. (2000), (2002); Col. 4, 5: VLA and VLBA 8.4 GHz flux density respectively; Col. 6, 7: VLA and VLBA 15.3 GHz flux density; Col. 8, 9: VLA and VLBA 22.2 GHz flux density; Col. 10: VLBA 43.2 GHz flux density; Col. 11: spectral index between the two frequencies where VLBA images are available; Col. 12: Equipartition magnetic field; we assume $\alpha = 0.7$; Col. 13: Morphological classification from VLBA images. The two sources J0111+3906 and J1751+0939 were not observed, since they are already plenty of information. The sources J0927+3902 and OQ 208 have been observed only for an extremely short period of time, to verify the system performance.

- d) the optical identification on the top right corner;
- e) the restoring beam, plotted on the bottom left corner of each image.

Source	z	Id	S _{8.4}	S _{8.4}	S ₁₅	S ₁₅	S ₂₂	S ₂₂	S ₄₃	α	H _{eq} mG	Morph
			VLA mJy	VLBA mJy	VLA mJy	VLBA mJy	VLA mJy	VLBA mJy	VLBA mJy			
J1603+1105		BL	225	176	234	176	217	-	-	0.0	94	Un
J1616+0459	3.197	Q	559	496	333	268	212	-	-	1.0	123	CJ
J1623+6624	0.203	G	283	296	224	216	175	-	-	0.5	49	Un
J1645+6330	2.379	Q	618		596		493	493	363	0.5	272	Un
J1717+1917	1.81	Q	229	-	227	167	215	97	-	1.5	145	Un
J1735+5049		G	920	875	740	672	587	-	-	0.4	27	CSO
J1751+0939	0.322	BL										
J1800+3848	2.092	Q	1063	-	1174	-	1076	768	537	0.5	277	Un
J1811+1704		BL	509	518	499	486	418	-	-	0.1	119	CJ
J1840+3900	3.095	Q	158	151	134	128	114	-	-	0.3	189	Un
J1850+2825	2.560	Q	1541	-	1318	1208	1045	867	-	0.8	150	MR
J1855+3742		G	212	189	124	87	91	-	-	1.3	19	CSO
J2021+0515		Q	368	359	267	242	191	-	-	0.7	43	CJ
J2024+1718	1.05	Q	800		697		569	495	294	0.8	74	Un
J2101+0341	1.013	Q	583	-	499	-	478	410	341	0.3	97	Un
J2114+2832	2.345	Q	792	-	749	466	685	373	-	0.6	40	CJ
J2123+0535	1.878	Q	2482	-	2755	-	2560	1719	1408	0.3	219	CJ
J2136+0041	1.932	Q	8940	-	7443	-	6169	3565	2218	0.8	71	CJ
J2203+1007		G	234	223	129	110	77	-	-	1.2	10	CSO
J2207+1652	1.64	Q	223	-	188	193	163	147	-	0.7	76	Un
J2212+2355	1.125	Q	1028	1242	975	1059	915	-	-	0.3	112	Un
J2257+0243	2.081	Q	450	-	558	-	528	427	272	0.7	212	Un
J2320+0513	0.622	Q	725	608	806	561	843	-	-	0.1	78	Un
J2330+3348	1.809	Q	463	408	532	431	548	-	-	0.1	141	MR

Table 4.2: Continued.

4.2.2 Notes on individual sources

The selection of young radio sources based only on the characteristics of the radio spectra has proved to be rather successful, although the presence of some contaminant objects cannot be avoided (see § 3; Orienti, Dallacasa & Stanghellini 2007a).

Flux-density and spectral shape variability is an important tool for a proper classification of the radio sources, but it must be complemented by accurate information on the pc-scale morphology. Intrinsically small and young radio sources are expected to have a “Double/Triple” structure like in CSOs, while a Core-Jet morphology can be taken as an indicator of blazar objects.

For a more reliable classification, both variability and morphology must be

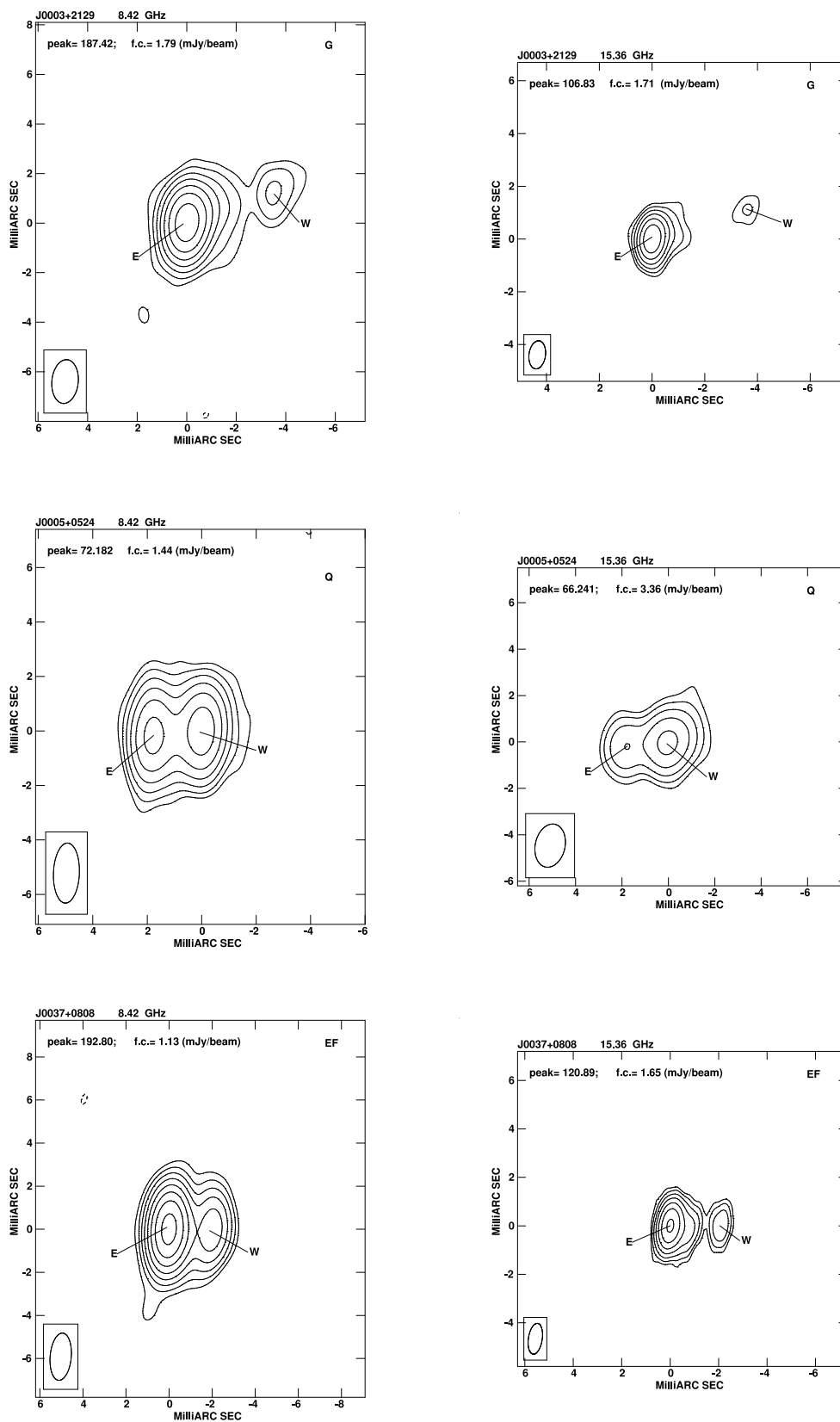


Figure 4.2: VLBA images at the two frequencies of candidates HFP with a CSO morphology. For each image we give the following information on the plot itself: a) Peak flux density in mJy/beam; b) First contour intensity (*f.c.*, in mJy/beam), which is generally 3 times the r.m.s. noise on the image plane; contour levels increase by a factor of 2; c) the optical identification; d) the restoring beam is plotted on the bottom left corner of each image.

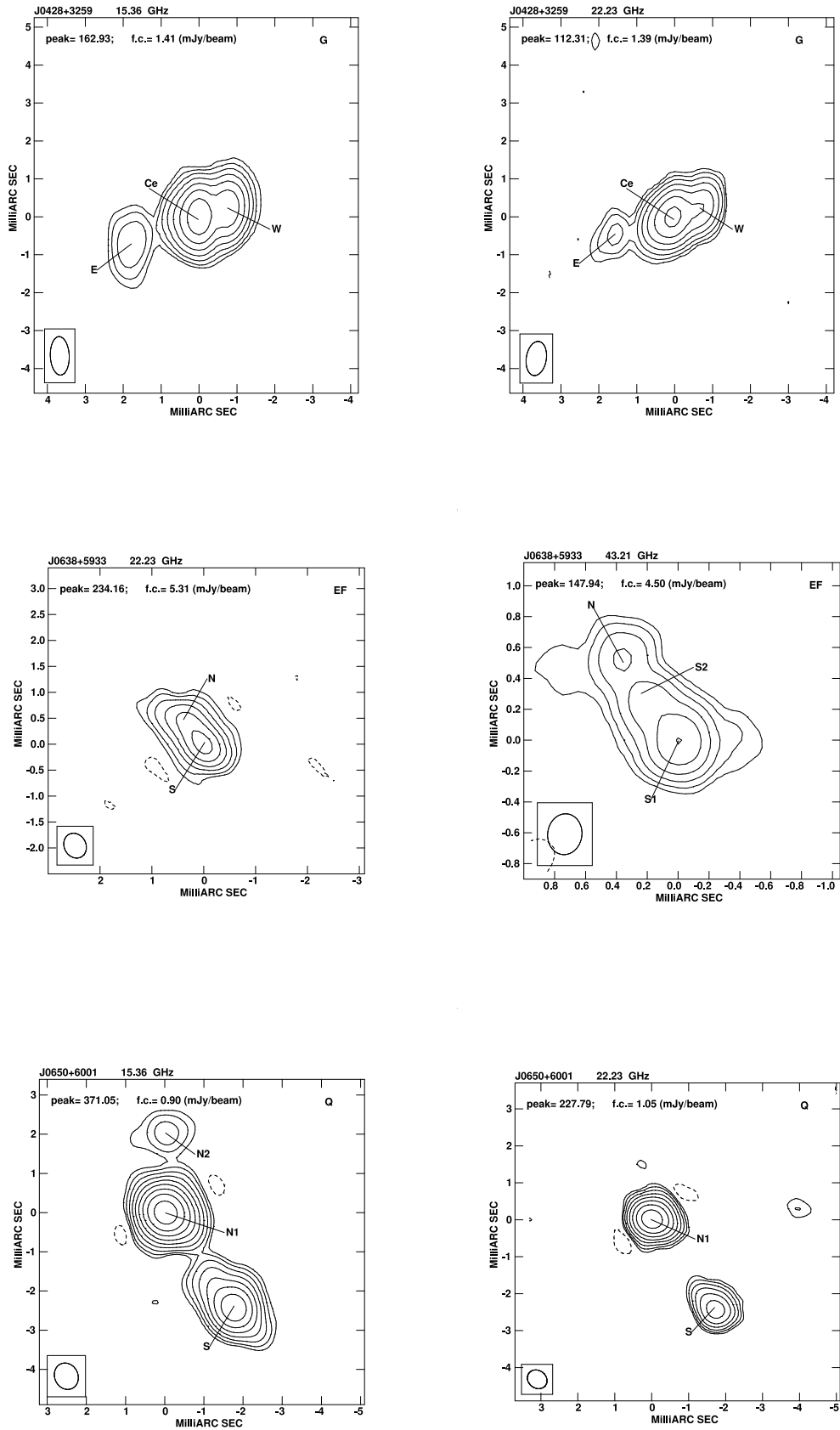


Figure 4.2: Continued.

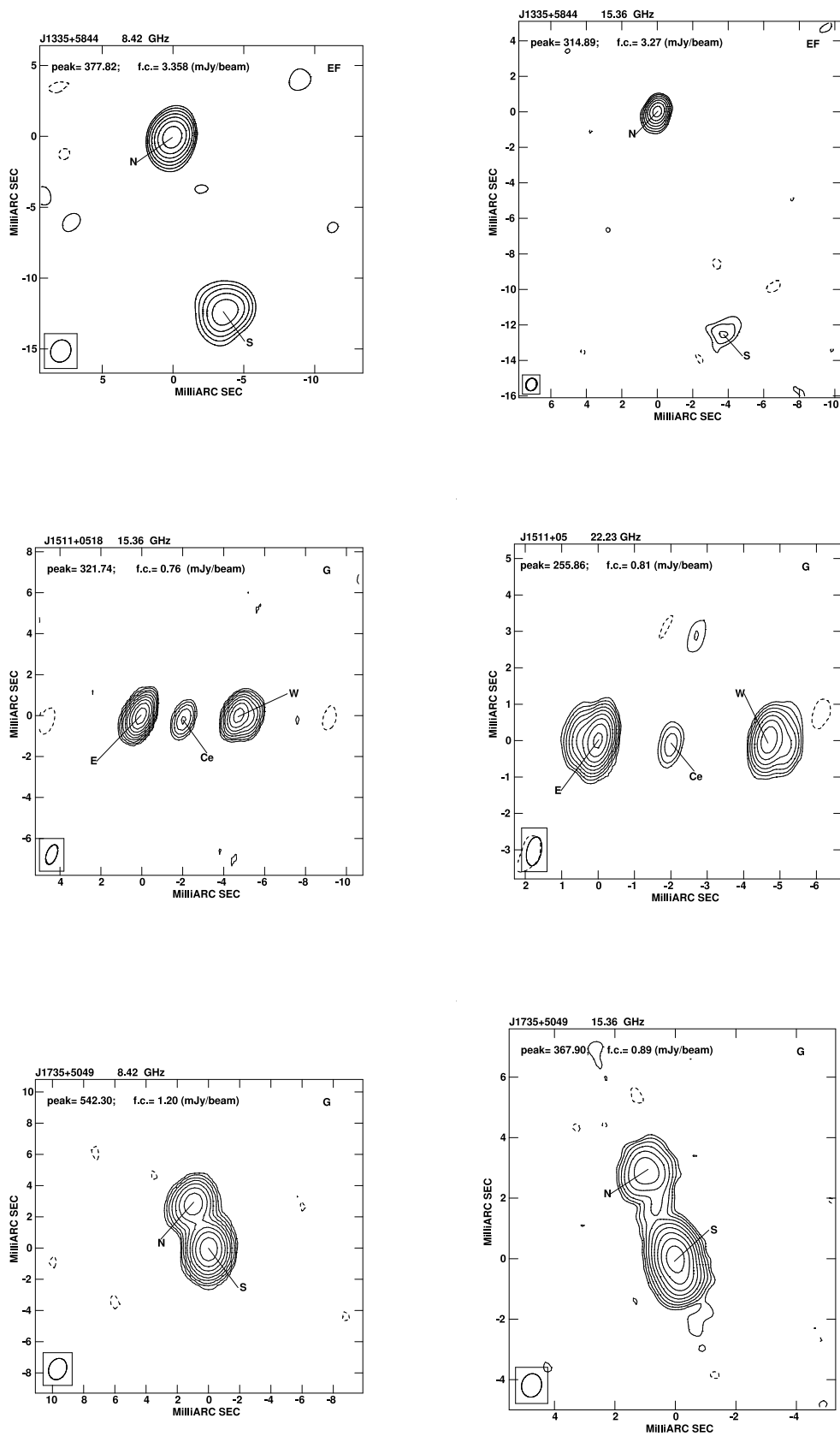


Figure 4.2: Continued.

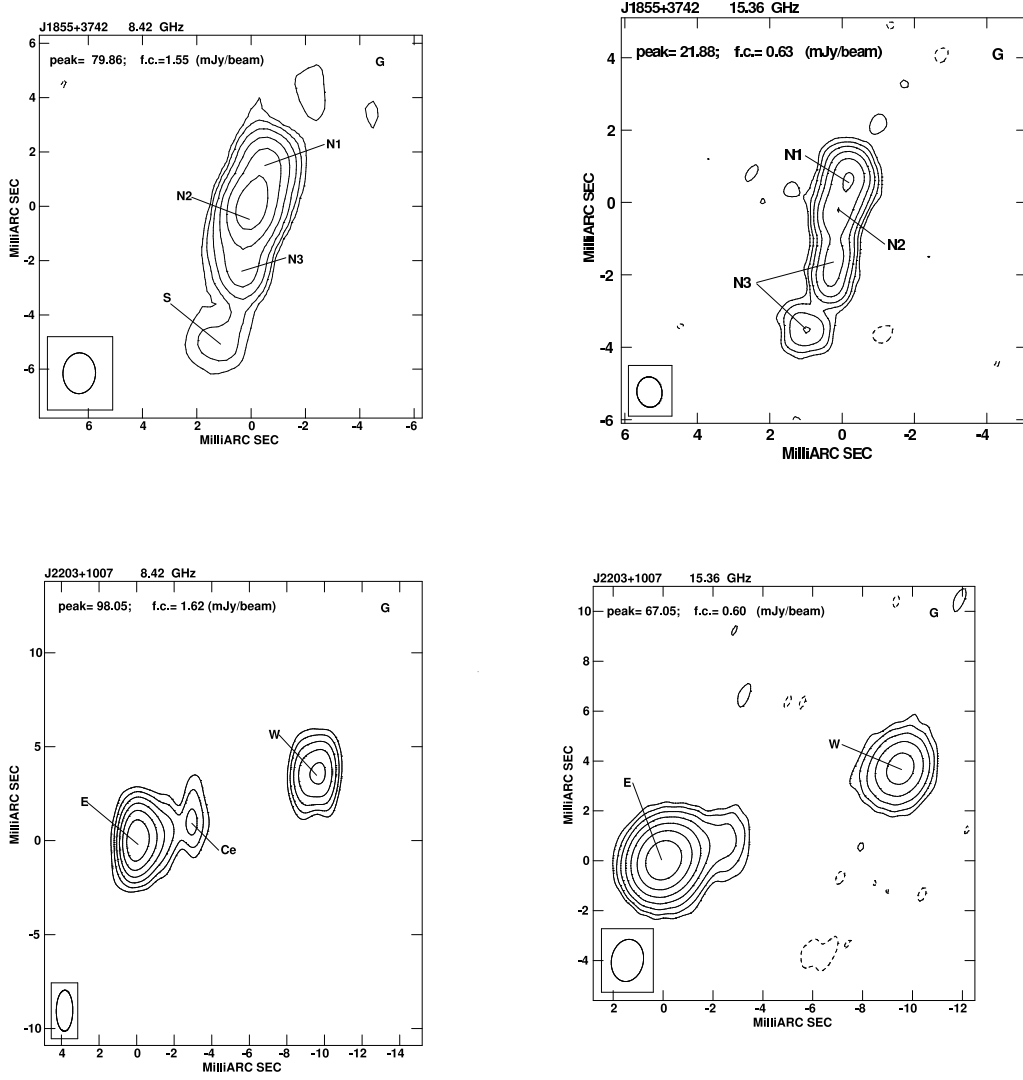


Figure 4.2: Continued.

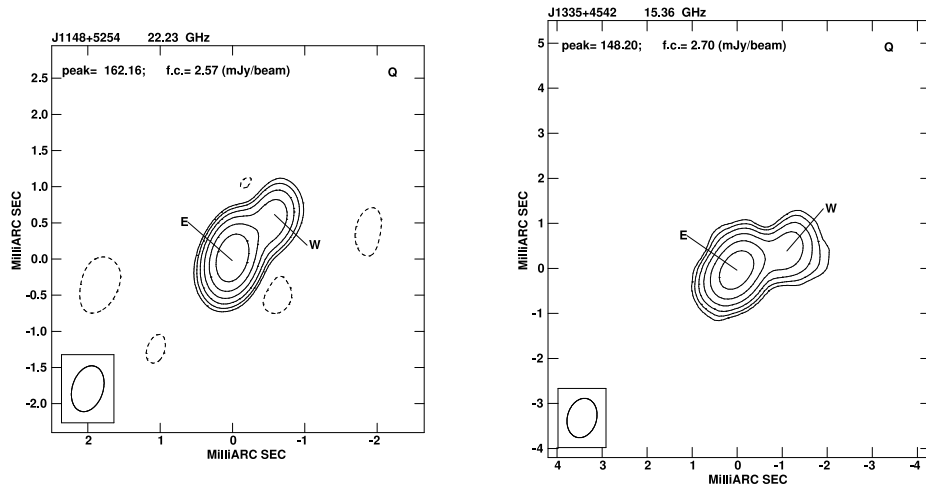


Figure 4.3: VLBA images of the sources with a CSO-like morphology, which are resolved at highest frequency only. For each image we give the following information on the plot itself: a) Peak flux density in mJy/beam; b) First contour intensity (*f.c.*, in mJy/beam), which is generally 3 times the r.m.s. noise on the image plane; contour levels increase by a factor of 2; c) the optical identification; d) the restoring beam is plotted on the bottom left corner of each image.

considered together.

In this section I discuss in detail the properties of the sources with a CSO-like or a Core-Jet structure, in the light of Fig. 4.2, 4.3, 4.4 and 4.5.

The total flux density inferred from these VLBA data is compared with the flux-density measured at the VLA and presented by Tinti et al. (2005) when available, since these observations have been carried out quite close in time.

To have a more complete information on the source structure, the availability of images at two frequencies allows the determination of the spectral properties. Typical errors on the determination of the spectral index are of the order of 0.1, being smaller on bright components and slightly larger on weak ones.

CSO candidates

CSO candidates are expected to have:

- “Double/Triple” structure in VLBA observations;
- no significant flux-density variability, that is values of the variability index, defined by Eq. 3.1, $V \leq 3$ and reported in Table 3.3;
- an overall spectrum with an optically-thin spectral index ≥ 0.5 (Table 4.2);
- source components with a steep optically-thin spectral index (Table 4.3).

The last two criteria are not always matched by young radio sources. If the source is observed at a frequency quite close to the turnover frequency of one of its components, the component spectral index will result flattish rather than steep as expected for its optically thin emission. In case that such a component also dominates the radio emission of the whole source at that particular frequency, even the overall spectrum will appear flat.

This phenomenon is particularly effective for sources with ν_t around or above 15 GHz.

Therefore, CSO candidates are considered all those sources which match only the first two selection criteria, while the remaining tools must be applied in relation to the actual ν_t value.

Thirteen sources (6 galaxies J0003+2129, J0428+3259, J1511+0518, J1735+5049, J1855+3742 and J2203+1007, 4 quasars J0005+0524, J0650+6001, J1148+5254 and J1335+4542, and 3 Empty Fields J0037+0808, J0638+5933 and J1335+5844) show a “Double/Triple” morphology similar to those found in CSO sources (Fig. 4.2, 4.3). Among them eight sources have a Double structure characterized by two separated components with significant flux-density asymmetry, like J0003+2129. Four sources show a Triple morphology (J0428+3259, J0650+6001, J1511+0518 and J2203+1007) where all the components have a steep spectrum. Since our VLBA observations have neither the dynamic range nor the resolution suitable to detect weak and flat component, no secure core identification could be provided based on the evidence coming out from our images only. J1855+3742 is the only source with a complex steep-spectrum structure.

All these 13 sources have not shown any significant amount of flux-density variability during the multi-epoch VLA monitoring program (Table 3.3), mainly showing variability indices $V \leq 3$.

In the following discussion I describe in more detail the characteristics of all the sources considered CSO-candidates.

- J0003+2129: galaxy at $z=0.452$. This source appears as a very asymmetric Double, with flux density ratio of $S_E/S_W \sim 25:1$ at both frequencies, making the two regions have almost the same spectral index of $\sim 0.8-0.9$. Most of the flux density originates within the Eastern component, while a weak feature, accounting for 8 and 5 mJy at 8.4 and 15 GHz respectively, is present to the West, ~ 4 mas apart. The total linear size is about 20 pc.

- J0005+0524: quasar at $z=1.887$. The radio emission originates within two well-resolved components, separated by 2 mas (~ 14 pc). Their flux density is quite similar at 8.4 GHz, while the asymmetry increases significantly at 15 GHz where $S_W/S_E \sim 3.6$.

The flattish spectrum ($\alpha \sim 0.2$) of the Western component may be consistent with self-absorption occurring at higher frequencies than in the Eastern component as a result of higher energy density. Such interpretation is also supported by the lack of any variability.

- J0037+0524: this source still lacks of optical identification (Dallacasa et al. 2002). It shows a Double morphology and the radio emission originates within two well-resolved components ~ 2 mas apart. Their flux density ratios are $S_E/S_W \sim 5$ and 10 at 8.4 and 15 GHz respectively, and both components have a steep spectrum.

- J0428+3259: galaxy at $z=0.479$ (Dallacasa et al. 2002; 2007). The images presented in Fig. 4.2 suggest that this source is an asymmetric Triple. The Eastern and Western components are 2 mas (11 pc) and 1 mas (5 pc) respectively from the central one, which is also the brightest emitting region. Their flux density ratios are $S_E:S_W:S_{Ce} = 1:4:10$ and $1:3.3:14$, at 15 and 22 GHz respectively. On arcsecond-scale there is a tentatively detection of an extended emission (Tinti et al. 2005), which has not been confirmed by the new observations (§ 3).

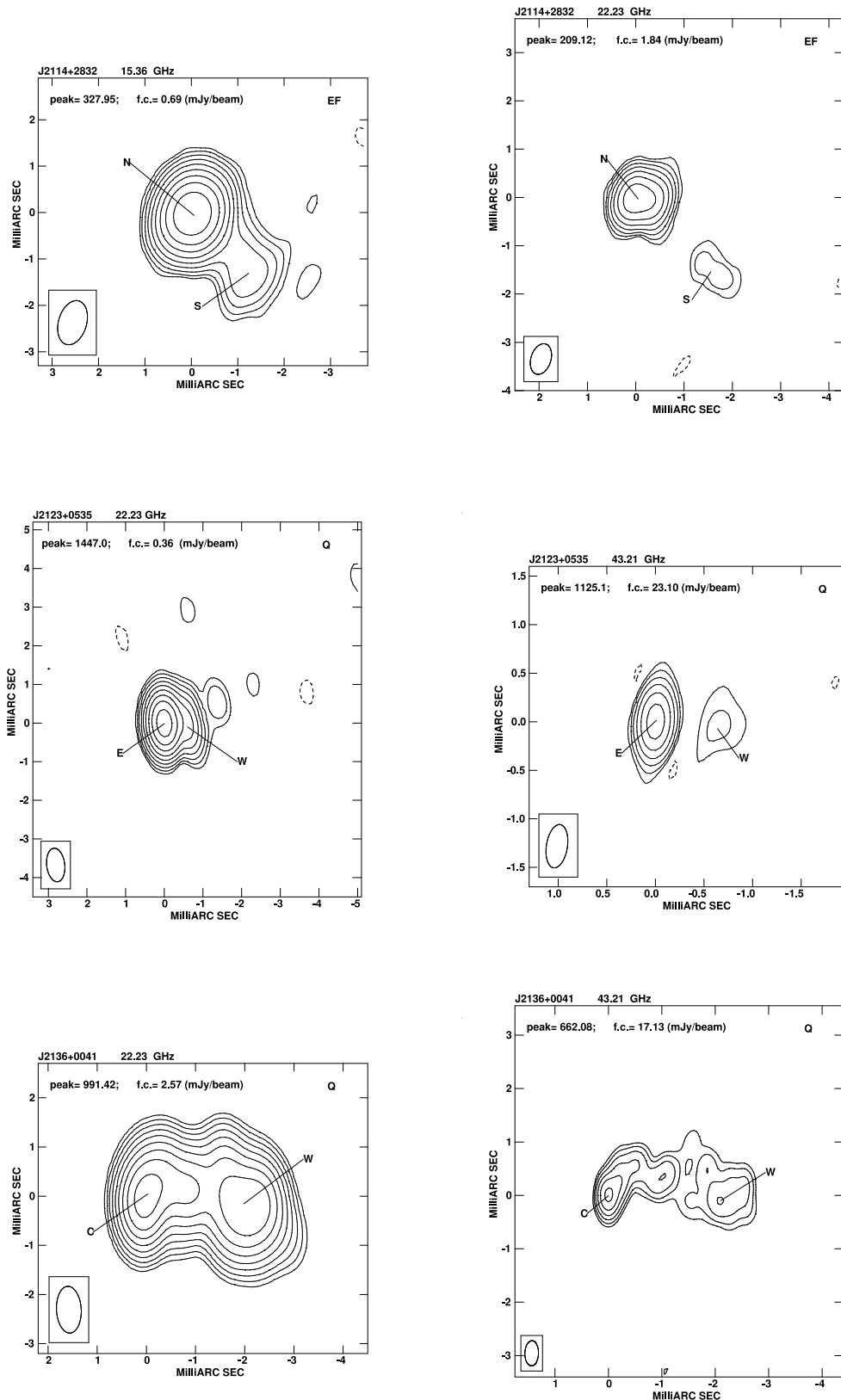


Figure 4.4: VLBA images at the two frequencies of the sources with a Core-Jet morphology. For each image we give the following information on the plot itself: a) Peak flux density in mJy/beam; b) First contour intensity (*f.c.*, in mJy/beam), which is generally 3 times the r.m.s. noise on the image plane; contour levels increase by a factor of 2; c) the optical identification; d) the restoring beam is plotted on the bottom left corner of each image.

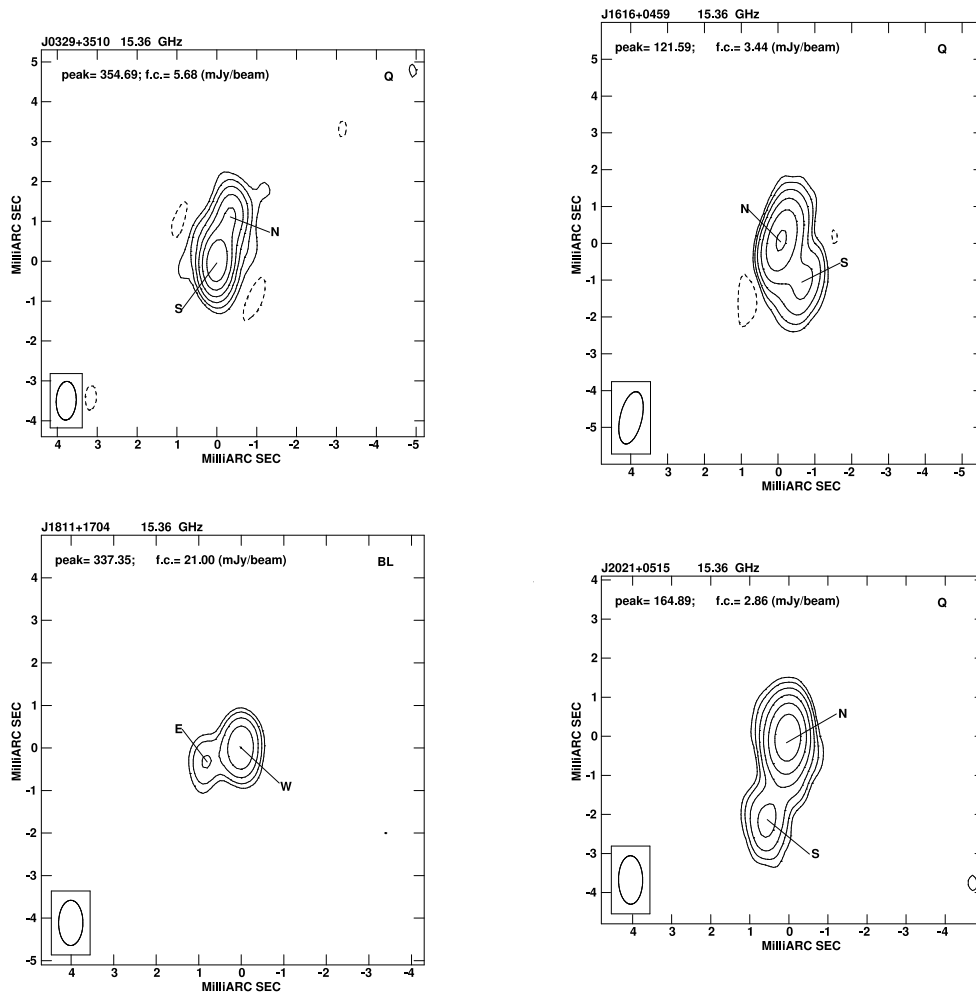


Figure 4.5: VLBA images of the sources with a Core-Jet morphology, which are resolved at highest frequency only. For each image we give the following information on the plot itself: a) Peak flux density in mJy/beam; b) First contour intensity (*f.c.*, in mJy/beam), which is generally 3 times the r.m.s. noise on the image plane; contour levels increase by a factor of 2; c) the optical identification; d) the restoring beam is plotted on the bottom left corner of each image.

- J0638+5933: no optical identification is available so far. This radio source is classified as a Triple. At the highest frequency the main component S is marginally resolved into two different regions with a flux density ratio $S_{S1}/S_{S2} \sim 4$. Since this component is unresolved at 22 GHz, in order to determine its spectral index the sum of the flux densities of S_{S1} and S_{S2} at 43 GHz must be taken into account. About 11% of the total flux density from the VLA is missing in the VLBA observations at 22 GHz.

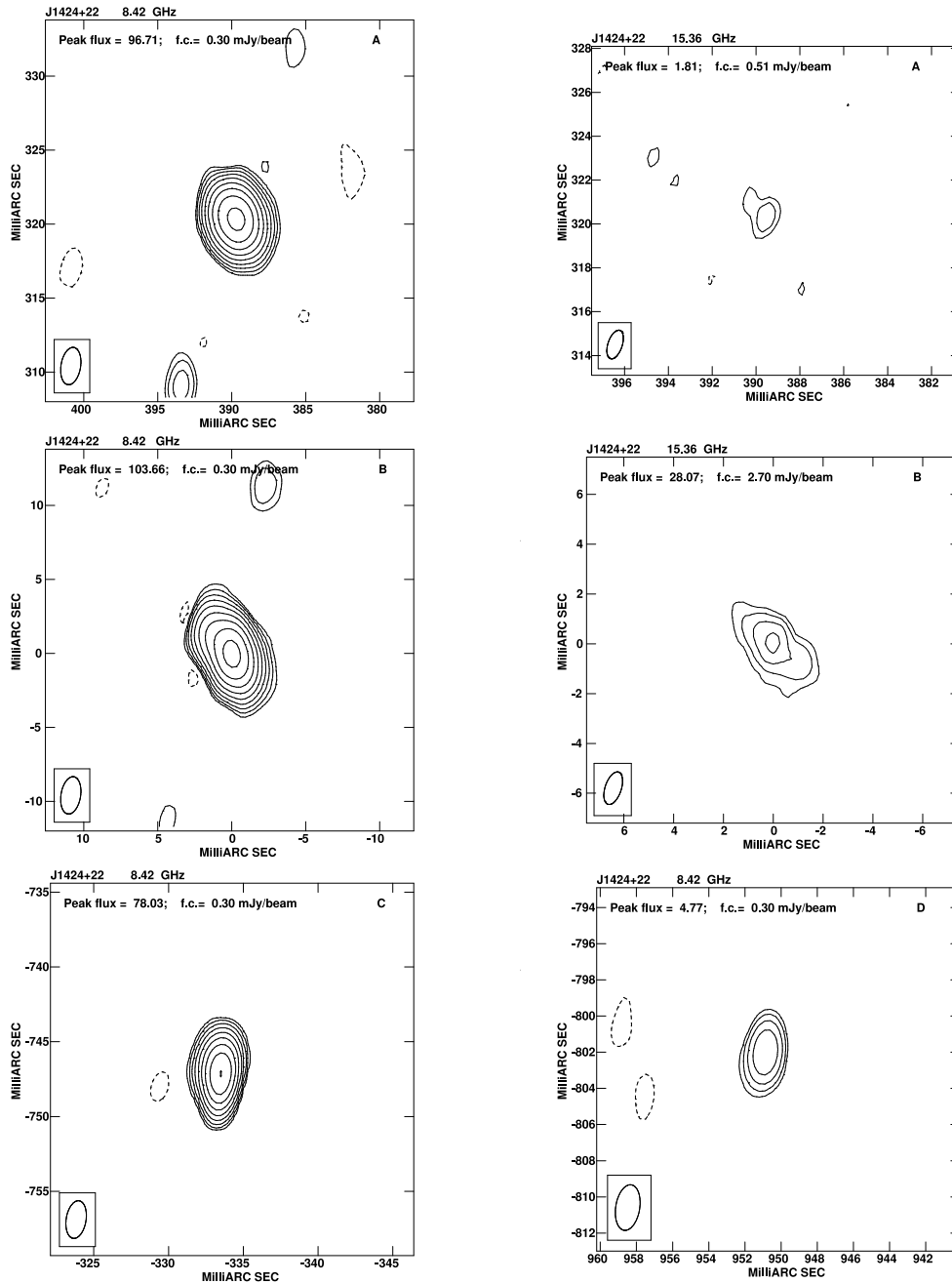


Figure 4.6: VLBA images of the gravitational lens system J1424+2256. *Top:* Images at 8.4 and 15 GHz of Component A. *Middle:* Images at 8.4 and 15 GHz of Component B. *Bottom:* Images at 8.4 of Component C (*left*) and D (*right*). For each image we give the following information on the plot itself: a) Peak flux density in mJy/beam; b) First contour intensity (*f.c.*, in mJy/beam), which is generally 3 times the r.m.s. noise on the image plane; contour levels increase by a factor of 2; c) the restoring beam is plotted on the bottom left corner of each image.

- J0650+6001: quasar at $z=0.455$. This source has been confirmed as a CSO by Polatidis et al. (1999). The radio emission originates within two components ~ 3 mas (~ 17 pc) apart. A weak feature, visible at 15 GHz only (Fig. 4.2) and accounting for 8 mJy is present to the North of the Northern component, in agreement with other works at lower frequencies (Stanghellini et al. 1999). Its nature is not well understood yet.

The Northern component is the most compact and brightest one, while the Southern one is clearly resolved N-S. Their flux density ratio is $S_N/S_S \sim 3.5$ and 4.2 at 15 and 22 GHz respectively. About 18% of the total flux density is missing in the VLBA image at 22 GHz.

A hint of flux-density variability, although at high frequency only, has been found. Flux-density measurements at the highest frequencies from Dallacasa et al. (2000) are systematically higher than those from subsequent epochs. However, no evidence of any further variability has been registered between data from Tinti et al. (2005) and new observations (§ 3; Orienti, Dallacasa & Stanghellini 2007a).

- J1148+5254: quasar at $z=1.632$. Although at 15 GHz it appears only marginally resolved in the NW direction, at 22 GHz (Fig. 4.3) it is clearly separated into two different asymmetric components. Their flux density ratio is $S_E/S_W \sim 5.8$ and 4.7 at 15 and 22 GHz respectively. We note that, although both components have steep spectra, the faintest is the flattest as well, with $\alpha_{15}^{22} \sim 0.6$, instead of 1.2 shown by the brightest component. About 14% of the total flux density is missing in the VLBA images at both frequencies. This comparison has been made with the flux density measured in 2003 (Orienti, Dallacasa & Stanghellini 2007a) and reported in § 3.

- J1335+4542: quasar at $z=2.449$. At 15 GHz (Fig. 4.3) the radio emission clearly comes from two different components, while at 8.4 GHz it appears marginally resolved in the NW direction. Their flux density ratio is $S_E/S_W \sim 4$ at 15 GHz. The Eastern component has a spectral index $\alpha_{8.4}^{15} \sim 0.6$, while the Western one has a very steep spectrum ($\alpha_{8.4}^{15} \sim 1.9$), although the fit to the images used to derive the flux density proved to be rather problematic at the lowest frequency.

About 11% and 14% of the total flux density is missing in the VLBA images at 8.4

and 15 GHz respectively.

- J1335+5844: there is an optical identification with a very weak red object likely a galaxy by Dallacasa et al. (2007). The optically thin spectral index of the source is 0.5. At 8.4 GHz the radio emission is clearly resolved into two compact regions in agreement with what found by Xiang et al. (2002), while at 15 GHz the southernmost component becomes weak and extended. The two components are separated by ~ 15 mas. Their flux density ratio is $S_N/S_S \sim 3$ and 8 at 8.4 and 15 GHz respectively. The Northern structure has a flattish spectrum ($\alpha_{8.4}^{15} \sim 0.1$), while the spectral index of the Southern component is very steep > 2 . For this reason Peck & Taylor (2000) did not consider this source as a CSO, and it was not included in the COINS sample. However, I still classify this source as a CSO candidate, since the flattish spectrum of the Northern region could be due to either an embedded core component or a very compact hot-spot whose turnover frequency ranges between 8.4 and 15 GHz (i.e. these VLBA observing frequencies). In VLBI images with a good dynamic range it was possible to identify the core component of the source (Dallacasa et al. 2005), which is located about midway between the outer regions. About 10% and 15% of the total flux density is missing in the VLBA images at 8.4 and 15 GHz respectively, most likely related to the Southern component.

- J1511+0518: optically identified with a Broad Line galaxy at $z=0.084$ (Chavushyan et al. 2001). The optically thin spectral index of the source is very steep with $\alpha_{15}^{22} \sim 1.2$.

At 15 GHz it is clearly resolved in three well-separated, aligned components. The flux density ratio of the outer components is $S_E/S_W \sim 2$ at both frequencies. On the other hand, the inner component accounts for 14 and 4 mJy at 15 and 22 GHz respectively, indicating a very steep spectral index $\alpha_{15}^{22} > 3$. The nature of this component has not been well understood yet. Although its location amongst the lobes may suggest that this component is the source core, its extremely steep spectral index makes such interpretation quite unlikely. About 30% of the total flux density is missing in the VLBA images at both frequencies.

New multi-frequency VLBA observations with longer integration times are necessary to understand this enigmatic object.

- J1735+5049: optically identified with a very faint object tentatively classified as a galaxy by Stickel & Kühr (1996). Information on the redshift is not available so far. This source shows a Double morphology, in agreement with what found by Xiang et al. (2002). The Southern component has a flattish spectrum of about 0.3, while the Northern is steeper ~ 1.2 . For this reason Peck & Taylor (2000) did not consider this source as a CSO, and it was not included in the COINS sample. However, I still classify this source as a CSO candidate, since the flattish spectrum could arise from a self-absorbed compact hot-spot with the turnover frequency between 8.4 and 15 GHz (i.e. these VLBA observing frequencies). New multi-frequency and high-resolution observations are necessary to unambiguously determine the nature of such source. About 9% of the total flux density is missing in the VLBA image at 15 GHz.

- J1855+3742: galaxy (Dallacasa et al. 2007). No redshift information is available. The pc-scale structure is quite different from all the other sources discussed so far. It presents a complex and elongated structure which is well resolved in the 15 GHz image. At 8.4 GHz the flux density is clearly peaked on the source centre, while at 15 GHz is more uniformly distributed. About 14% and 33% of the total flux density is missing in the VLBA images at 8.4 and 15 GHz respectively.

- J2203+1007: galaxy (Dallacasa et al. 2002). No redshift information is available. This source has been confirmed as a CSO by Gugliucci et al. (2005). It shows a Triple morphology, but the radio emission mainly originates in the outer components, located about 10 mas apart. Their flux density ratio is $S_E/S_W \sim 2.2$ and 4.8 at 8.4 and 15 GHz respectively. As in J1511+0518, the central component, which accounts for 11 mJy at 8.4 GHz, is completely resolved out at 15 GHz, indicating a very steep spectral index. About 19% of the total flux density is missing in the VLBA image at 15 GHz.

Core-Jet structures

Here I describe the properties of the seven objects with a Core-Jet structure. I consider Core-Jet those sources with significant amount of variability ($V > 3$, Table 3.3) and an elongated structure comprising a compact component (containing the source core) with a possibly flat spectrum which dominates the radio emission (from 70% up to 90%), and other structures with steeper spectra (Table 4.4).

However, it is possible that the structure embedding the core component comprises also some emission from the jet-base. This causes the spectral index of such component to become steeper than expected.

Seven objects (6 quasars J0329+3510, J1616+0459, J2021+0515, J2114+2832, J2123+0535 and J2136+0041 and one BL Lac J1811+1704) show a clear Core-Jet morphology. Three of these sources (J0329+3510, J1811+1704 and J2123+0535) did not show the inverted spectrum during the second-epoch of VLA observations (Tinti et al. 2005), which actually turned out to be flat. Furthermore, when imaged with high-sensitivity VLA observations, these three sources do show some amount of extended emission on the arcsecond-scale.

- J0329+3510: quasar at $z=0.50$ (Dallacasa et al. 2007). The pc-scale radio structure of this source is characterized by a compact and bright component, and a second one located at ~ 1 mas (7 pc) apart in the NW direction. Although at 8.4 GHz this source appears only marginally resolved, it has been possible to fit the parameters of both components. Their flux density ratio is $S_S/S_N \sim 2$ at both frequencies and both the radio components have an inverted spectral index $\alpha_{8.4}^{15} \sim -0.2$. Extended emission has been detected on the arcsecond-scale with the VLA at 1.4, 1.7 and 4.9 GHz (Tinti et al. 2005). In the VLA second epoch observations it does not show the convex spectrum anymore, indicating that this is a blazar object, and it will be rejected from the final sample of genuine young and small radio sources.

- J1616+0459: quasar at $z=3.197$. Although the source structure can be interpreted in terms of either a CSO-like source or a Core-Jet blazar, I consider this source as a blazar objects since it has a high percentage of polarized emission ($> 2\%$) which is a typical characteristic of beamed objects (see § 5; Orienti & Dallacasa 2007b), and a variability index ~ 15.2 (Tinti et al. 2005). At 15 GHz the radio emission clearly

originates within two different regions ~ 1.4 mas (11 pc) apart (Fig. 4.3), while at 8.4 GHz it is only marginally resolved in the SW direction. Their flux density ratio is $S_N/S_S \sim 3.5$ at both frequencies. The total flux density measured by the VLBA is about 11% and 21% lower than that from the VLA at 8.4 and 15 GHz respectively.

- J1811+1704: optically identified with a stellar object by Dallacasa et al. (2002). Since its optical spectrum has been found featureless, it has been considered as a BL Lac (Dallacasa et al. 2007).

This source is characterized by a Double morphology at the highest frequency, while at 8.4 GHz it is only marginally resolved in the E-W direction. The brightest component has an inverted spectrum ($\alpha_{8.4}^{15} \sim -0.1$), suggesting the presence of the source core. It shows an arcsecond-scale structure in the VLA images at 1.4 and 1.7 GHz (Tinti et al. 2005). In the VLA second epoch observations it does not show the convex spectrum anymore, indicating that this source is actually a blazar, and it will be rejected from the sample of candidate HFPs.

- J2021+0515: stellar object (Dallacasa et al. 2002). At 15 GHz the radio emission originates within two well-resolved components, ~ 2 mas apart, while at 8.4 GHz it is only marginally resolved. Super-resolving the lower-frequency image in the N-S direction, there is an indication that the overall structure might be an asymmetric Double. Although the radio emission mainly comes from the brightest component (labeled N in Fig. 4.5), its spectrum is steeper than the Southern component ($\alpha_{8.4}^{15} \sim 0.8$ instead of -0.4 for the N and S components respectively). The total flux density measured by the VLBA at 15 GHz is about 10% lower than that from the VLA.

- J2114+2832: quasar at $z=2.345$. At 15 GHz this source is characterized by a compact and bright component which accounts for 93% of the total flux density and with a spectral index of $\alpha_{15}^{22} \sim 0.6$. At 22 GHz such component is marginally resolved in the E-W direction, suggesting that we are looking at the jet-base. Another extended low-brightness structure with a steep spectral index ($\alpha_{15}^{22} \sim 1.0$) is located ~ 2 mas apart (~ 16 pc).

- J2123+0535: quasar at $z=1.878$. The radio emission of this source mainly

originates within a compact region (E component) which accounts for $\sim 90\%$ of the total flux density. A weak feature visible in the VLBA image at 43 GHz only is located to the Western part of the main component, leading the radio morphology to be considered as a Double. Both spectral indices are quite flattish ($\alpha_{22}^{43} \sim 0.3$ and 0.5 for the E and W components respectively). About 33% of the total flux density is missing in the VLBA image at 22 GHz. This source was a GPS candidate observed by the ATCA monitoring program. Despite its convex spectrum, it has been rejected as a new GPS candidate for the evidence of significant variability (Edward et al. 2004). Furthermore, in the second epoch of VLA observations its radio spectrum turned out to be flat (Tinti et al. 2005), indicating that this source is a blazar and it will be dropped from the sample of candidate HFP.

- J2136+0041: quasar at $z=1.932$. This object was early recognized as a GPS source by Shimmins et al. (1968). It has a Core-Jet morphology, although at low frequencies it may appear as a Double with components of similar flux density. Stanghellini et al. (2001) found polarization percentage of 2-3% at 15 GHz. The source core (labeled as C) is located in the South end of the easternmost component. The jet is initially directed to the North, then bends to the West. The spectral index of the jet is rather steep $\alpha_{22}^{43} \sim 1.3$, while the core has a flatter spectrum ($\alpha_{22}^{43} \sim 0.7$), although this value may be slightly increased by some emission from the steep-spectrum jet-base. This source maintains the GPS spectral shape at the various epochs, although with a significant amount of flux density variability. Extended emission has been detected on the arcsecond-scale with the VLA (Stanghellini et al. 2005). About 57% of the total flux density is missing in the VLBA image at 22 GHz. It is worth noting that the VLA observations considered as a comparison between the total flux densities are those from Dallacasa et al. (2000), and it is possible that some amount of the missing flux density could be related to an intrinsic variability.

The gravitational lens J1424+2256

The gravitational lens J1424+2256 is associated with a quasar of 16.5 magnitude at $z=3.62$. For this reason it is one of the lens systems with the highest apparent luminosity (Patnaik et al. 1992b). The lensing object belongs to a group of galaxies

at $z=0.338$ (Kudnic et al. 1997).

In these VLBA observations the lens system consists of four components (Fig. 4.6). From the Position Angle (PA) of the three brightest component, $PA_A=56^\circ$, $PA_B=43^\circ$ and $PA_C=14^\circ$, we see that these components are tangentially elongated as expected from the lens models. Component D is unresolved in these observations. Their flux density at 8.4 GHz, accounting for S_A 156 mJy, S_B 169 mJy, S_C 89 mJy and S_D 4.6 mJy, as well as their PA, are in good agreement with what found in a previous work by Patnaik et al. (1999) based on VLBI images at the same frequency. At 15 GHz only the two brightest components have been detected. Component B shows the same elongation as at lower frequency, while component A is almost resolved out.

From previous works based on both VLA and VLBA data, some amount of polarized emission has been found in the three brightest components, accounting for 2.5%, 1.8% and 1.2% in A, B and C respectively. Component D was too faint to detect any polarization (Patnaik et al. 1999, 1992b).

4.3 Discussion

4.3.1 Radio structure and optical identification

There is a clear separation in radio morphology between quasars and galaxies. The majority of galaxies ($\sim 78\%$) show a “Double/Triple” morphology, while quasars are generally either Core-Jet ($\sim 16\%$) or Unresolved ($\sim 71\%$).

This is consistent with the idea that the HFP spectrum in galaxies and quasars comes from intrinsically different emitting regions: mini-lobes and/or hot-spots in galaxies; compact regions related to the core and the jet-base in quasars. This is in agreement with other results obtained by comparing the properties of galaxies and quasars in GPS (Stanghellini et al. 2005) and bright CSS samples (Fanti et al. 1990). It is likely that HFP quasars (as well as GPS quasars) are intrinsically similar to the flat-spectrum radio sources, and their convex spectrum is due to a single homogeneous component, like a knot in the jet, which temporarily dominates the radio emission, although some HFP quasars can still be genuine young radio sources.

As largely discussed in § 3, strong support to the idea that a significant fraction of

HFP quasars represent a different population of beamed objects, i.e. blazars, comes from the detection of substantial flux density and spectral shape variability (Oriente, Dallacasa & Stanghellini 2007a; Tinti et al. 2005). All the sources found to display a Core-Jet morphology do present these characteristics.

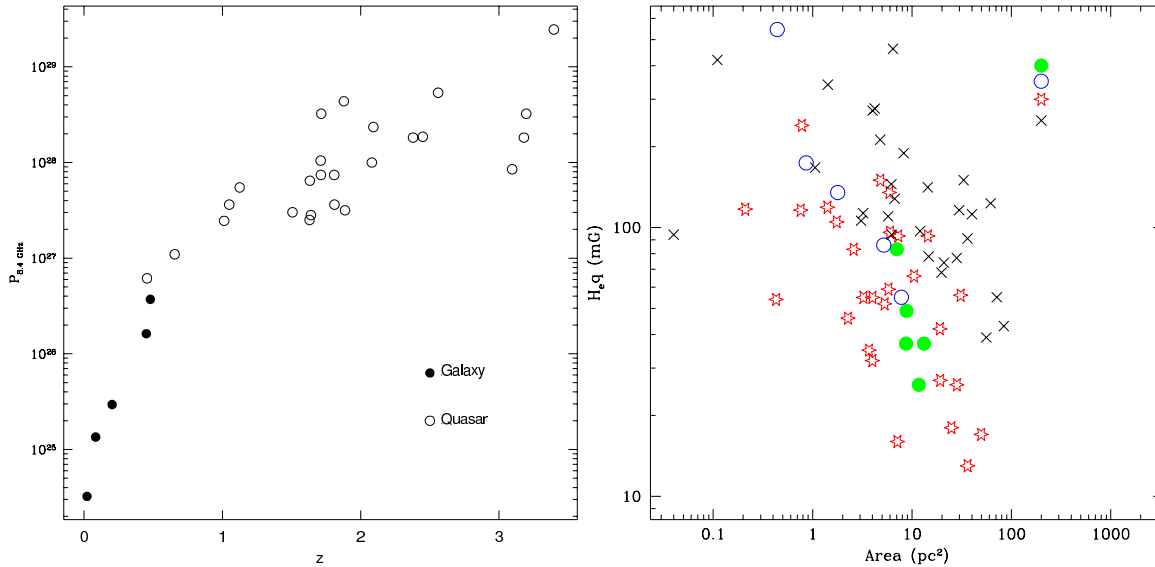


Figure 4.7: *Left*: Distribution of the monochromatic luminosity at 8.4 GHz (W/Hz) versus the redshift, for the HFP objects with known z . The apparent luminosity has been computed on the basis of the VLA flux density. There is a clear influence of the redshift: galaxies, characterized by low redshift, are located in the bottom left part of the plot, while quasars dominate the upper right region. *Right*: Distribution of the emitting area versus the equipartition magnetic field.

4.3.2 Physical parameters

For each radio source component physical parameters have been computed assuming equipartition condition and using standard formulae (Pacholczyk 1970). Proton and electron energies have been assumed equal with a filling factor of unity. Ellipsoidal geometry and an average optically thin spectral index of 0.7 have been adopted.

The average luminosity of the sources is $P \sim 10^{27.5}$ W/Hz with a clear influence of the redshift, being the most distant sources (quasars) the most luminous as well (Fig. 4.7a).

In the components of candidate CSOs, typical values obtained for the minimum total energy (U_{\min}), minimum energy density (u_{\min}), equipartition magnetic field

(H_{eq}), and brightness temperature (T_{b}) are:

$$U_{\text{min}} \sim 10^{53} - 10^{54} \text{ erg};$$

$$u_{\text{min}} \sim 10^{-4} - 10^{-5} \text{ erg/cm}^3;$$

$$H_{\text{eq}} \sim 10^{-2} \text{ G};$$

$$T_{\text{b}} \sim 10^8 - 10^{11} \text{ K};$$

Very similar values are found in the jet components of the HFPs with a Core-Jet morphology, while the core regions are generally characterized by higher energy density and brightness temperature, as they have larger luminosities and smaller sizes.

If we compare these results with what obtained in CSS radio sources with similar radio power (Fanti et al. 1990), we find that the minimum energies stored in CSSs are 2 - 3 orders of magnitude larger than in CSO-like HFPs, but the corresponding energy densities are 2 - 3 orders of magnitude lower due to larger volumes occupied. Fig. 4.7b plots the equipartition magnetic field versus the emitting area. There is a clear segregation among the different morphologies. The bottom right part of the plot is dominated by CSO and jet components, while the core components and the unresolved sources are mainly located in the upper part. This result may be very useful to better classify CSO candidates. Indeed, as Core and Jet structures have deep differences in their equipartition magnetic field and emitting area, if such a trend is found also in a CSO candidate, this may suggest a possible wrong classification.

Following the definition by Readhead (1994), the *equipartition brightness temperature* for each source has been computed. Since this parameter mainly depends on the redshift and marginally on the observed parameters, such as the observed peak frequency and the corresponding flux density, it can be determined with high precision, becoming a good observable quantity against which to test theoretical models.

Values ranging from 7×10^{10} K up to 2.5×10^{11} K have been obtained, in agreement with what found in previous works by Readhead (1994).

Then the *maximum brightness temperature* $T_{\text{b,max}}$, which is the brightness temperature computed with the parameters of the spectral peak (i.e. ν_t , S_t), has

been estimated. The comparison between T_{eq} and $T_{\text{b,max}}$ is an important tool to investigate a possible departure from the minimum energy and equipartition conditions, since $T_{\text{b,max}}/T_{\text{eq}}$ is an independent way to derive the equipartition Doppler factor (Readhead 1994). For an object in which the equipartition condition applies, the equipartition Doppler factor computed using the flux density at the peak of the spectrum is equal to the true Doppler factor. If flux density concerns the optically-thin part of the spectrum (as in the case of these VLBA measurements), the equipartition Doppler factor is a lower limit to the true Doppler factor.

The use of the equipartition Doppler factor provides a method to identify boosted components in powerful extragalactic radio sources which slightly depends on observable quantities. In this context, a $T_{\text{b,max}} \gg T_{\text{eq}}$ is a strong indication that the source is a boosted blazar.

In all the unresolved sources, in the core components and in a few of the brightest CSO components we find $T_{\text{b,max}}/T_{\text{eq}} \sim 2-3$, while for the majority of CSOs such ratio is ≤ 1 . This result is a further indication that those sources with CSO-like characteristics are not beamed objects, while Core-Jet objects display some amount of boosted flux-density.

Source	Comp	S _{8.4} mJy	S _{15.3} mJy	S _{22.2} mJy	S _{43.2} mJy	α	$\theta(1)$ mas	$\theta(2)$ mas	P.A.	H _{eq} mG	ν_{\max} GHz	LAS mas	LLS pc
J0003+2129	E	214	126			0.9	0.32	0.28	150	46	4.8		
	W	8	5			0.8	0.95	0.22	120	52	1.3	3.8	22
J0005+0524	W	90	82			0.2	0.97	0.27	95	56	4.0		
	E	73	23			1.9	0.64	0.53	92	42	3.0	1.7	14
J0037+0808	E	215	150			0.6	0.44	0.26	80	59	5.3		
	W	41	15			1.7	0.37	0.21	75	32	2.9	2.1	17 ¹
J0428+3259	E		23	12		1.7	1.01	0.26	100	16	1.8	1.9	11
	Ce		233	168		0.9	0.63	0.19	109	55	5.3		
	W		93	40		2.2	0.20	0.08	147	54	4.9	0.8	5
J0638+5933	S			313	236	0.4	0.22	0.16	91	105	11.4		
	N			179	60	1.6	0.19	0.08	104	116	10.0		
	N1				73		0.26	0.20	-	83	7.03	0.76	-
J0650+6001	N		479	327		1.0	0.40	0.39	95	55	6.5		
	S		144	78		1.6	0.45	0.32	37	35	3.9	3.2	18
J1148+5254	E		306	199		1.2	0.23	0.06	3	240	13.9		
	W		53	42		0.6	0.25	0.10	9	119	7.2	0.8	7
J1335+4542	E	345	242			0.6	0.67	0.17	125	135	7.7		
	W	188	60			1.9	0.67	0.30	130	66	4.2	1.3	11
J1335+5844	N	422	388			0.1	0.44	0.22	161	150	7.5		
	S	165	46			2.1	1.19	0.84	121	17	1.9	14.8	118 ¹
J1511+0518	E		415	285		1.0	0.24	0.06	-	114	7.7	2.1	3
	Ce		15	4		3.5	0.23	0.11	177	35	2.3		
	W		256	150		1.4	0.55	0.21	130	117	4.6	2.8	4
J1735+5049	N	182	87			1.2	0.69	0.56	33	27	3.1	3.4	27 ¹
	S	692	573			0.3	0.91	0.16	18	93	7.6		
J1855+3742	N1	43	29			0.7	0.58	0.41	179	26	2.0	1.9	15 ¹
	N2	106	25			2.1	0.67	0.15	157	43	3.2		
	N3	29	33			-0.2	1.27	0.64	137	16	1.5	2.4	19 ¹
	S	10					1.91	1.19	131	8	0.8	5.3	42 ¹
J2203+1007	E	129	92			0.6	0.98	0.58	112	26	2.7	3.2	25 ¹
	W	58	18			2.0	1.09	0.46	110	18	1.7	7.3	58 ¹
	Ce	11					1.30	0.56	170	13			

Table 4.3: The VLBA flux density of each component, for the sources with a CSO-like morphology. Columns 1 and 2: source name and sub-component label; Columns 3, 4, 5 and 6: VLBA flux density at 8.4, 15.3, 22.2 and 43.2 GHz respectively; Column 7: spectral index between the two frequencies where VLBA images are available; Columns 8, 9 and 10: Deconvolved angular sizes of major and minor axis of the best-fitting Gaussian component and the position angle of major axis as estimated on the most suitable images at the different frequency, using JMFIT. Column 11: Equipartition magnetic field; we assume $\alpha = 0.7$. Column 12: Turnover frequency; Columns 13 and 14: the angular and linear distance between the components. ¹For the sources with redshift unknown, we adopt $z=1.00$.

Source	Comp	S _{8.4} mJy	S _{15.3} mJy	S _{22.2} mJy	S _{43.2} mJy	α	$\theta(1)$ mas	$\theta(2)$ mas	P.A.	H _{eq} mG	ν_{\max} GHz	LAS mas	LLS pc
J0329+3510	S	340	374			-0.2	0.30	0.12	173	107	9.0		
	N	126	143			-0.2	0.57	0.31	163	39	4.1	1.2	7
J1616+0459	N	390	208			1.1	0.74	0.43	157	93	5.8		
	S	106	60			1.0	0.46	0.29	123	96	5.2	1.4	11
J1811+1704	W	342	367			-0.1	0.178	0.097	168	174	12.1		
	E	176	119			0.7	0.54	0.49	173	37	3.17	0.84	7 ¹
J2021+0515	N	327	202			0.8	0.49	0.32	156	55	5.3		
	S	32	40			-0.4	0.76	0.23	147	37	3.1	2.4	27 ¹
J2114+2832	N		447	360		0.6	0.55	0.19	81	86	7.9		
	S		19	13		1.0	0.84	0.28	47	26	2.3	1.9	15 ¹
J2123+0535	E			1528	1269	0.3	0.16	0.05	18	545	36.1		
	W			191	139	0.5	0.37	0.34	50	83	7.6	0.68	6
J2136+0041	C			1614	1038	0.7	0.54	0.15	146	230	16.5		
	W			1695	718	1.3	1.24	0.71	65	76	8.0	2.2	19

Table 4.4: The VLBA flux density of Core-Jet source components. Columns 1 and 2: source name and sub-component label; Columns 3, 4, 5 and 6: VLBA flux density at 8.4, 15.3, 22.2 and 43.2 GHz respectively; Column 7: spectral index between the two frequencies where VLBA images are available; Columns 8, 9 and 10: Deconvolved angular sizes of major and minor axis of the best-fitting Gaussian component and the position angle of major axis as estimated on the image at the highest frequency, using JMFIT. Column 11: Equipartition magnetic field; we assume $\alpha = 0.7$. Column 12: Turnover frequency; Columns 13 and 14: the angular and linear distance between the components.

¹For the sources with redshift unknown, we adopt $z=1.00$.

Chapter 5

Polarization properties

Given their intrinsically small linear sizes, young radio sources are entirely contained within the Interstellar Medium (ISM) of the host galaxy.

The most compact (< 1 kpc) objects completely reside within the innermost part of the Narrow-Line Region (NLR) of the parent galaxy. The environment of this region is characterized by a two-phase plasma: the clumpy component, with high density $n_e \sim 10^2 \text{ cm}^{-3}$ and temperature $T \sim 10^2 \text{ K}$, but small filling factors $\phi < 10^{-4}$ (McCarthy 1993), and a diffuse component, less dense $n_e \sim 10^{-1} \text{ cm}^{-3}$ and hotter $T \sim 10^4 \text{ K}$, which fills the inter-cloud space. Both components can act as a Faraday Screen, causing significant Faraday Rotation and Depolarization in presence of magnetic field.

As a consequence, if the structure of the Faraday Screen (i.e. the magnetic field geometry and local variations in n_e) is not resolved by the observations, extragalactic radio sources entirely embedded in such an ambient medium are expected to show some Rotation Measure (RM) and strong Depolarization, able to reduce or even cancel a linear polarization which intrinsically would amount to a few percent.

As the source expands (> 1 kpc), its radio emission emerges from NLR and reaches the outer regions of the ISM where a smoother environment may substantially reduce the Faraday Rotation and depolarization effects.

The evidence of a relationship between the fractional polarization and the linear sizes has been pinpointed by Cotton et al. (2003) and Fanti et al. (2004) by studying the sources from the B3-VLA CSS sample (§ 2.1.4; Fanti et al. 2001) which span linear sizes from a fraction of kpc to a few kpc. In their work Cotton et al. (2003) found that at 1.4 GHz almost all the sources smaller than 6 kpc are completely unpolarized. Moving to 5.0 and 8.4 GHz, Fanti et al. (2004) found the same behaviour, but the

complete depolarization of the radiation happens at progressively smaller linear sizes ($< 3\text{-}5$ kpc).

The dependence of the polarization degree on the frequency is expected if the depolarization is actually due to Faraday Effects.

From the anti-correlation between the peak frequency and the linear sizes (O’Dea & Baum 1997), genuine young HFP radio sources should extend on sub-kpc scales. Following the results from Fanti et al. (2004), with such linear sizes they are likely to be found completely unpolarized at cm-wavelengths.

On the other hand, blazar objects usually are large radio sources which appear foreshortened due to orientation effects together with some amount of beaming which enhances the core region making the large-scale low-surface brightness emission hardly visible in low dynamic range observations. Since their synchrotron radiation actually originates outside the Faraday Screen, significant amount of linearly polarized emission is expected.

The tight relationship found between circular polarization (CP) and flat-spectrum objects only (Homan & Wardle 1999; Gilbert & Conway 1970) makes the detection of CP an unambiguous blazar-identifier.

Therefore a possible further diagnostic in order to recognize blazar objects among HFPs is the search for circularly polarized emission. This task is rather difficult and requires a very careful analysis of the data and will be one of the further development of the thesis work.

5.1 Polarization observations and data reduction

Simultaneous multi-frequency observations of the 45 (out of the 55) candidate HFPs that were visible during the allocated observing time, were carried out in July 2002 with the VLA in B configuration, in full polarization mode, with a bandwidth of 50-MHz, and with typical observing time of 60 seconds per source, per frequency.

HFP candidates were observed at 1.465 and 1.665 GHz (the L band), 4.565 and 4.935 (C band), 8.085 and 8.465 GHz (X band), 14.96 GHz (U band), and 22.46 GHz (K band). In U and K bands the two IFs have been taken adjacent in order to increase the sensitivity.

Since the sources are relatively strong and generally unresolved with the VLA, snap-

shot observing mode was considered adequate. Secondary calibrators were observed for 1.5 min at each frequency every 25 min; they were chosen to minimize the telescope slewing time. The data reduction followed the standard procedures for the VLA, implemented by the NRAO AIPS software.

After the standard amplitude and phase calibration, the instrumental polarization has been determined by means of the observation of an unresolved and unpolarized source over a wide range of parallactic angles.

The absolute orientation of the electric vector has been determined from the data of the primary flux density calibrator 3C 286, which was observed twice. The residual instrumental polarization is evaluated to be 0.1% (C and X bands), and 0.3% (U and K bands), with a residual uncertainty on the intrinsic orientation of the electric vector of about 2° - 3° , depending on the observing bands.

Measurements in the L band are less sensitive than those from the NVSS (Condon et al. 1998) due to the less accurate calibration of the instrumental polarization, mainly caused by some RFI which affected some scans of the calibrator for the instrumental polarization. Therefore, these data were complemented with the polarization measurements available from the NVSS at 1.4 GHz.

Besides the total intensity (Stokes' I parameter), polarization images in the Stokes' U and Q parameters were then produced with the AIPS task IMAGR for each frequency, with the only exception of the L band. Since such observations were not suitable to detect circular polarization, no images in the Stokes' V parameter have been created.

In the polarization images the final noise (1σ) is usually of ~ 0.1 mJy for C and X bands, and ~ 0.2 mJy for U and K bands, although in a few cases higher noise has been found in these latter bands precluding the detection of the polarized emission due to low signal-to-noise ratio. Technical problems in the X, U and K bands were present during the observations of three sources (J1335+4542, J1335+5844 and J1407+2827), and no polarization information at such frequencies could be provided.

Then images of polarization intensity and polarization angle have been produced by combining the Stokes' U and Q images with the AIPS task COMB using the options 'POLC', 'POLA' respectively. The percentage polarization image was then obtained by combining the polarization intensity and the total intensity with the

same task but with the option 'DIV'.

Polarization measurements on the Stokes' U, Q and on the polarization intensity images have been obtained with the AIPS verb IMSTAT by setting a window on the total intensity image of each source.

Since the polarized flux density S_p has been computed from the Stokes' Q and U maps, its value and the corresponding error σ_p have been determined taking into account the correction to the positive noise bias (Condon et al. 1998):

$$S_p = \sqrt{S_Q^2 + S_U^2 - (1.2\sigma_{QU})^2} \quad \text{with} \quad \sigma_{QU} = \sqrt{\sigma_Q^2 + \sigma_U^2},$$

$$\sigma_p = \frac{\sqrt{(S_Q \cdot \sigma_Q)^2 + (S_U \cdot \sigma_U)^2}}{S_p}.$$

where S_Q and S_U are the flux density measured on the Stokes' Q and U images by the AIPS verb IMSTAT, and σ_Q and σ_U their corresponding errors.

The fractional polarization m and its error σ_m have been computed by:

$$m = S_p/S_I \quad \sigma_m = \sqrt{(S_p/S_I)^2 + (S_p \cdot \sigma_I/S_I^2)^2},$$

where S_I and σ_I are the total intensity flux density measured on the images and the correspondent error.

The polarization angle χ is obtained as:

$$\chi = 0.5 \cdot \arctan \frac{S_U}{S_Q} \quad \sigma_\chi = 0.5 \cdot \frac{\sigma_{QU}}{S_p}.$$

In Table 5.1, for all the 45 observed sources we report:

- Column 1: the source name (J2000);
- Column 2: the optical identification. G = Galaxy; Q = Quasar; BL = BL Lac; EF = Empty Field.
- Column 3: redshift;
- Column 4: VLBI morphology (§ 4; Orienti et al. 2006a).

- Columns 5, 7, 9, 11, 13: polarization percentage m and errors σ_m at K, U, X, C and L (from the NVSS, Condon et al. 1998) bands respectively;
- Columns 6, 8, 10, 12, 14: polarization angle χ and errors σ_χ at K, U, X, C and L (from the NVSS, Condon et al. 1998) bands respectively;

For unpolarized sources and for those with a signal-to-noise ratio below 2σ in the polarized emission, the polarization angle is not provided.

Source	Id.	z	Morph.	Sm ^K	χ ^K	m ^U	χ ^U	m ^X	χ ^X	m ^C	χ ^C	m ^L	χ ^L
J0003+2119	G	0.452	CSO	0.67±0.20	-34.8±10.8	0.58±0.14	15.7±9.6	<0.01	-	<0.08	-	<0.01	-
J0005+0524	Q	1.887	CSO	-	-	-	-	0.49±0.10	14.5±4.2	<0.05	-	0.39±0.01	55.5±17.7
J0037+0808	EF		CSO	<0.1	-	0.2±0.2	-	<0.04	-	<0.01	-	<0.01	-
J0111+3906	G	0.668	CSO	<0.1	-	<0.1	-	0.17±0.10	-68.0±3.0	<0.01	-	0.13±0.01	49.7±14.7
J0116+2422	EF		Un	<0.1	-	-	-	<0.08	-	<0.06	-	2.82±0.01	-78.2±1.8
J0217+0144	Q	1.715	Un	1.02±0.11	71.4±2.7	2.2±0.11	73.2±2.5	2.73±0.08	87.3±2.5	1.70±0.05	83.8±2.5	1.53±0.01	42.0±0.8
J0329+3510	Q	0.5	CJ	1.64±0.16	-0.5±2.6	1.62±0.08	34.6±2.6	0.49±0.02	59.2±2.7	1.03±0.03	-75.0±2.6	4.98±0.01	-45.9±0.7
J0357+2319	Q		Un	3.19±0.33	88.5±2.7	2.15±0.17	-86.8±3.5	1.74±0.07	-80.5±2.7	1.48±0.07	-68.1±2.9	0.78±0.01	-16.2±6.3
J0428+3259	G	0.479	CSO	<0.1	-	<0.1	-	0.12±0.01	72.4±5.1	0.04	-	<0.01	-
J0519+0848	EF		Un	1.58±0.16	54.9±2.6	-	-	0.98±0.03	89.2±2.6	2.00±0.06	86.6±2.5	2.30±0.01	-6.3±2.2
J0625+4440	BL		Un	0.72±0.10	-74.9±4.4	-	-	2.09±0.07	-87.2±2.6	2.38±0.08	-85.5±2.6	4.70±0.01	-79.2±1.4
J0638+5933	EF		CSO	<0.1	-	-	-	0.13±0.01	32.0±4.1	0.03	-	<0.01	-
J0642+6758	Q	3.180	Un	<0.3	-	0.82±0.10	-43.1±5.5	0.60±0.03	-68.8±2.9	1.62±0.05	-81.2±2.5	<0.01	-
J0646+4451	Q	3.396	MR	2.49±0.25	19.5±2.5	3.56±0.18	17.4±2.5	3.14±0.09	29.9±2.5	1.62±0.05	29.0±2.5	0.80±0.01	44.2±2.2
J0650+6001	Q	0.455	CSO	<0.1	-	-	-	<0.1	-	0.03	-	0.02±0.01	24.9±78.5
J1335+4542	Q	2.449	CSO	-	-	-	-	-	-	<0.01	-	<0.01	-
J1335+5844	EF	-	CSO	-	-	-	-	-	-	<0.01	-	0.25±0.01	12.8±30.7
J1407+2827	G	0.0769	CSO	-	-	-	-	-	-	<0.06	-	0.86±0.01	-33.8±9.7
J1412+1334	EF		Un	<0.1	-	-	-	0.23±0.03	-9.6±5.1	0.03	-	0.37±0.01	2.9±11.6
J1424+2256	Q	3.626	Un	0.2	-	-	-	3.41±0.10	3.1±2.5	0.40±0.02	61.8±2.7	0.57±0.01	2.5±5.1
J1430+1043	Q	1.710	MR	-	-	-	-	<0.1	-	0.07	-	0.47±0.01	-71.0±6.3
J1457+0749	BL		Un	-	-	2.83±0.21	-39.2±3.3	5.28±0.16	-35.3±2.5	5.71±0.17	-33.2±2.5	-	-
J1505+0326	Q	0.411	Un	1.09±0.12	-43.4±2.9	-	-	0.98±0.03	-44.1±2.5	0.24±0.01	-40.6±3.0	1.62±0.01	55.7±1.4
J1511+0518	G	0.084	CSO	<0.1	-	-	-	0.21±0.01	-13.6±3.0	0.07	-	<0.01	-
J1526+6650	Q	3.02	MR	<0.1	-	<0.1	-	<0.01	-	<0.10	-	0.57±0.01	-23.4±16.4
J1603+1105	BL		Un	<0.2	-	0.3	-	0.93±0.04	-35.7±2.9	1.79±0.06	-3.1±2.6	-	-
J1616+0459	Q	3.197	CJ	2.26±0.24	89.8±3.0	-	-	2.91±0.09	-86.2±2.5	0.40±0.01	-40.6±2.7	0.05±0.01	-44.3±60.7
J1623+6624	G	0.203	Un	<0.1	-	<0.1	-	<0.01	-	<0.06	-	0.23±0.01	-81.6±22.5
J1645+6330	Q	2.379	Un	2.91±0.29	77.9±2.6	2.69±0.14	72.7±2.6	3.04±0.09	63.1±2.5	1.30±0.04	46.2±2.5	2.35±0.01	-15.2±1.6
J1735+5049	G		CSO	<0.1	-	<0.1	-	0.10±0.01	-87.3±3.8	0.07	-	0.10±0.01	43.8±18.1
J1800+3848	Q	2.092	Un	0.62±0.06	-83.6±2.7	-	-	0.25±0.01	-24.4±2.7	0.13±0.01	39.6±3.9	0.57±0.01	56.0±4.7
J1811+1704	BL		CJ	7.12±0.71	-49.6±2.6	6.68±0.34	-41.8±2.5	1.79±0.06	8.7±2.5	2.30±0.07	-19.4±2.5	-	-
J1840+3900	Q	3.095	Un	0.97±0.21	85.3±7.7	-	-	0.32±0.05	-36.3±6.0	<0.10	-	0.36±0.01	88.9±16.7
J1850+2825	Q	2.560	MR	0.1	-	<0.1	-	<0.06	-	<0.01	-	0.28±0.01	41.0±15.0
J1855+3742	G		CSO	<0.1	-	<0.1	-	<0.01	-	<0.01	-	0.47±0.01	30.8±10.4
J2021+0515	Q		CJ	1.65±0.19	46.7±3.4	1.36±0.10	-76.3±3.3	<0.05	-	0.30±0.02	43.5±3.3	0.26±0.01	7.4±10.4
J2024+1718	Q	1.05	Un	0.85±0.09	44.8±2.9	0.59±0.04	-32.5±3.0	0.80±0.03	44.9±2.6	0.19±0.01	-4.9±3.3	0.28±0.01	-53.4±11.2
J2101+0535	Q	1.013	Un	2.53±0.26	-67.8±2.6	3.53±0.18	-68.9±2.6	4.49±0.14	-67.8±2.5	3.74±0.11	-59.7±2.5	0.05±0.01	13.4±29.8
J2123+0535	Q	1.878	CJ	3.67±0.37	-0.9±2.5	2.74±0.14	1.0±2.5	0.81±0.02	22.3±2.5	1.08±0.03	81.8±2.5	2.02±0.01	53.2±0.5
J2203+1007	G		CSO	<0.1	-	<0.1	-	<0.01	-	<0.01	-	0.40±0.01	49.5±18.4
J2207+1652	Q	1.64	Un	<0.1	-	<0.1	-	1.55±0.06	86.7±2.6	1.32±0.05	-72.0±2.7	3.64±0.01	55.3±1.1
J2212+2355	Q	1.125	Un	8.61±0.86	35.8±2.5	7.88±0.40	38.2±2.5	6.82±0.20	28.0±2.5	5.66±0.17	-3.8±2.5	2.03±0.01	43.1±0.8
J2257+0243	Q	2.081	Un	<0.2	-	<0.2	-	0.30±0.01	-52.3±2.8	<0.1	-	0.91±0.01	43.8±0.8
J2320+0513	Q	0.622	Un	0.92±0.09	69.3±2.6	1.36±0.07	44.4±2.6	2.74±0.08	58.6±2.5	4.33±0.13	70.6±2.5	2.31±0.01	58.8±0.7
J2330+3348	Q	1.809	MR	1.12±0.12	44.5±2.7	<0.2	-	0.53±0.02	-32.9±2.8	1.43±0.05	-17.0±2.6	1.21±0.01	-39.3±3.5

Table 5.1: Polarization properties.

5.2 Polarization analysis

The intrinsic radio linear polarization, the Rotation Measure and the Depolarization are discriminant ingredients in the determination of different classes of extragalactic radio sources.

Our multi-frequency VLA polarization measurements, in addition to the information from the NVSS data allow us to identify and remove contaminant objects from the HFP sample.

5.2.1 Fractional polarization in HFPs

As seen in the previous chapters, the “bright” HFP sample (Dallacasa et al. 2000) still contains contaminant objects, like blazars in particular phases of their characteristic variability.

The properties of the polarized emission of young radio sources and blazars are very different. Statistical studies (e.g. Fanti et al. 2004) have led to the discovery that young radio sources show a monotonic reduction in their median polarization with decreasing frequency, consistent with substantial depolarization. In contrast, blazars show a relatively constant median polarization at all frequencies (Klein et al. 2003).

In these VLA data, 18 sources (Table 5.1) have significant ($m > 1\%$) polarized emission at all frequencies, while other 18 objects (Table 5.1) are completely unpolarized at all frequencies. Of the remaining sources, 4 (3 quasars J1424+2256, J2021+0515 and J2207+1652 and 1 BL Lac J1603+1105) have $>1\%$ of polarized emission at one/two frequencies only, and 5 (1 galaxy J0003+2129 and 4 quasars J0005+0524, J1800+3848, J1840+3900 and J2257+0243) are marginally polarized ($\sim 2\sigma$ noise level).

The fractional polarization m at each frequency is compared with the total intensity flux density variability V , as described in § 3.2.2 (Orienti, Dallacasa & Stanghellini 2007a; Tinti et al. 2005). Table 5.2 lists the median m at each frequency for *all* the sources and for those with $V < 3$ and $V > 3$.

There is a well established difference in the polarization percentage between sources with different variability index: 17 objects ($\sim 94\%$) of the polarized ($m > 1\%$) sources are strongly variable ($V \gg 3$) and among them 11 objects ($\sim 65\%$) do not show the

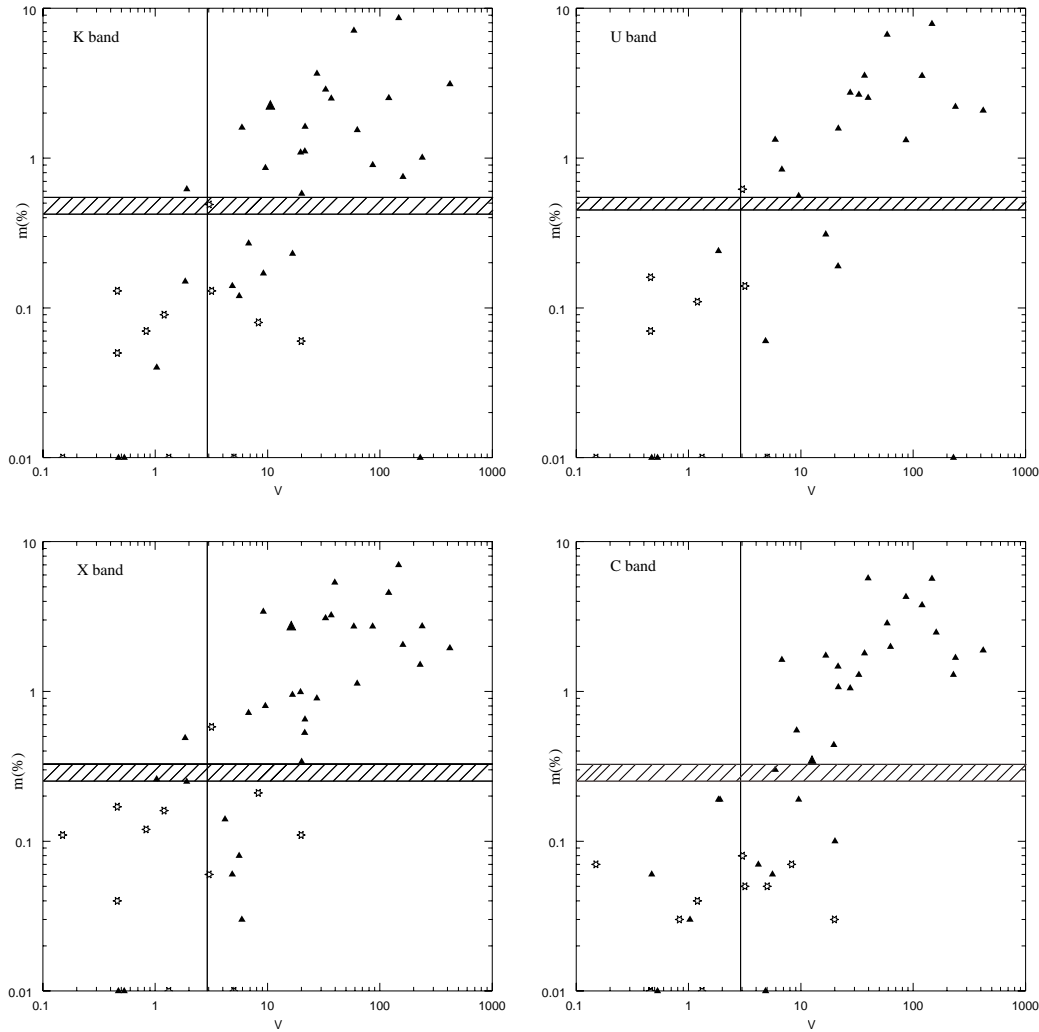


Figure 5.1: Polarization percentage in K, U, X and C band. The vertical line represents the total intensity flux density variability $V=3$. The horizontal lines indicate the detection limit. All the sources below this region are completely unpolarized. Empty stars and filled triangles represent sources with and without a CSO-like morphology, respectively. The error bars of the polarized objects are within the symbols, while in case of unpolarized objects error bars are not plotted, and they are as large as the panel.

convex radio spectrum anymore, while 18 objects (89%) of the unpolarized sources have $V < 3$ (Oriente & Dallacasa 2007b).

Fig. 5.1 shows the plots of the polarization percentage versus the total intensity flux density variability at the four frequencies.

From these diagrams it becomes clear that significant fractional polarization is found

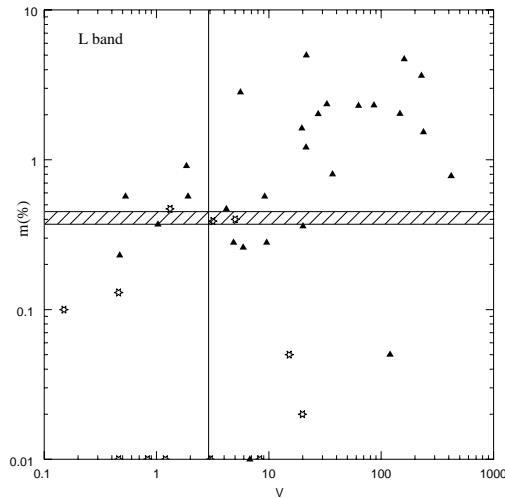


Figure 5.2: Polarization percentage at 1.4 GHz, derived from the NVSS data (Condon et al. 1998). The vertical line represents the total intensity flux density variability $V=3$. The horizontal lines indicate the detection limit. All the sources below this region are completely unpolarized. Empty stars and filled triangles represent sources with and without a CSO-like morphology, respectively. The error bars of the polarized objects are within the symbols, while in case of unpolarized objects error bars are as large as the panel, and they are not plotted

only among sources with $V > 3$. The median V of the sources with high m (i.e. larger than the median m of the sample) is more than 10 times higher than that of sources with low m , independent of frequency.

If the fractional polarization is compared to the pc-scale structure (Table 5.1), it results that 75% of the sources with a CSO-like morphology (represented by empty stars in Fig. 5.1), are unpolarized at all frequencies, while the majority (60%) of the sources without a CSO-like structure (filled triangles in Fig. 5.1) are polarized. Only one source with a CSO-like morphology (the galaxy J0003+2129) do show a significant ($>3\sigma$) polarized emission at the highest frequencies, while it is unpolarized in the C band, as expected in presence of a Faraday Screen.

Therefore, the comparison between the fractional polarization and the pc-scale structure (Orienti et al. 2006a), suggests that sources with or without a CSO-like morphology have a different degree of polarization.

At low frequency (1.4 GHz), the polarimetric information is from the NVSS (Condon et al. 1998). Although these data are not simultaneous with those presented here, and variability in polarization may play a role for sources with high V , there is still a

Band	All		V<3		V>3	
	m_{md}	Error	m_{md}	Error	m_{md}	Error
L	0.57	0.24	0.40	0.19	1.37	0.36
C	0.25	0.23	0.04	0.01	1.07	0.29
X	0.56	0.26	0.11	0.05	0.95	0.31
U	0.56	0.37	0.09	0.07	1.33	0.47
K	0.38	0.29	0.07	0.04	0.90	0.38

Table 5.2: Median degrees of percentage polarization and the statistical errors for all the sources in which polarized emission $>2\sigma$ -noise level has been detected. L-band data are from the NVSS (Condon et al. 1998).

Bands	All		V<3		V>3	
	DP_{md}	Error	DP_{md}	Error	DP_{md}	Error
C/X	0.60	0.12	0.30	0.07	0.90	0.15
C/K	0.53	0.26	0.24	0.08	0.63	0.18
X/K	0.73	0.25	0.22	0.20	0.85	0.27

Table 5.3: Median degrees of depolarization and the statistical errors for the sources in which polarized emission has been detected. Only upper limits at the lowest frequency have been considered.

segregation in the fractional polarization between sources with high and low values of the variability index (Fig. 5.2). Sources polarized at the highest frequencies do show polarization also at 1.4 GHz, while unpolarized sources have no polarization even in the L band, with the only exception of the source J0116+2422.

This source is completely unpolarized in these VLA data, while it possesses some degree of polarization (2.82%) at 1.4 GHz. This can be interpreted in terms of polarization variability, which is quite common in blazar objects. Although the small value of V suggests that this source is a genuine young HFP, there is also the possibility that it is actually a blazar object with variability on time-scale much longer (or shorter) than that investigated by our VLA multi-epoch monitoring program.

However it must be noted that there is a confusing unresolved source at a few arcseconds from J0116+2422, that may influence the NVSS measurements.

Source	z	RM _{oss}	RM _{int}	DP _X ^C
J0217+0144	1.715	59	435	0.6
J0329+3510	0.5	478	1076	1.7
J0357+2319		48	192	1.0
J0519+0848		134	536	2.0
J0625+4440		-44	-176	1.1
J0642+6758	3.18	-199	-3477	2.2
J0646+4451	3.396	54	1043	0.5
J1457+0749		28	112	1.1
J1505+0326	0.411	16	32	0.2
J1616+0459	3.197	267	4703	0.1
J1645+6330	2.379	-154	-1758	0.4
J1811+1704		1089	4356	0.8
J2024+1718	1.05	nf		0.2
J2101+0341	1.013	46	186	0.9
J2123+0535	1.878	432	3578	1.2
J2212+2355	1.125	-189	853	0.8
J2320+0513	0.622	67	176	1.7
J2330+3348	1.809	-1225	9666	2.6

Table 5.4: The Observed and the Intrinsic Rotation Measures RM_{obs} and RM_{int} based on measurements at four or three different frequencies and the Depolarization computed between C and X bands. nf: data not fitted by linear relation. When the redshift is unknown, we assume $z=1.0$ to compute the RM_{int} .

5.2.2 Depolarization and Rotation Measure

The Rotation Measure in radio sources as well as their depolarization derived from multi-frequency polarimetry is strictly related to the distribution of both the thermal plasma and the magnetic field inside and outside the source.

We compute the depolarization DP defined by Eq. 1.5:

$$DP = \frac{m_{\nu_1}}{m_{\nu_2}}, \quad \text{with } \nu_1 < \nu_2,$$

for all the sources with a detected polarized emission (only upper limits at the lowest frequency have been included).

The median values found among the various bands and obtained considering all the sources with detected polarization $> 2\sigma$ -noise level, are consistent with a slight depolarization (Table 5.3). The comparison becomes more significant if we consider sources with different variability. Sources with $V < 3$ are usually strongly depolarized, with median $\leq 0.30 \pm 0.07$ consistent with a homogeneous population of very slightly-

polarized sources.

On the other hand, sources with $V > 3$ have median $\sim 0.9 \pm 0.15$, consistent with a polarized-population characterized by an almost constant polarization at the various frequencies, but with inhomogeneous polarization percentage among the sources.

Since NVSS data are not simultaneous to the VLA observations presented here, no depolarization with the L band has been computed in order to avoid results affected by random effects.

For the 18 sources ($\sim 60\%$) with polarization $> 3\sigma$ at three or four frequencies we compute the Rotation Measure RM (§ 1.3).

In the observed sample 11 sources have χ measured at four frequencies and 7 at three frequencies only. When the signal-to-noise ratio was good enough, a separate analysis of each observing frequency in C and X bands was made in order to obtain 2 independent measurements per band.

To determine the RM I started verifying whether the χ at different frequencies were well interpolated by the linear fit. In a few cases the minimum number of $\pm n\pi$ had to be added such as to have the best linear fit (Fig. 5.3). Then, a least-square fit to the data was performed to check the reliability of the RM obtained.

All the sources with significant polarized emission were found to follow the relation $\chi \propto \lambda^2$, except the source J2024+1718 for which no linear fit could interpolate the data.

A KS-test has not found ($>99\%$) any correlation between the Rotation Measure and the Depolarization (Orienti & Dallacasa 2007b).

5.3 Polarimetry and the nature of the radio sources: summary

Measurements of the polarization of the radio emission from extragalactic radio sources provide a great deal of information on the physical conditions inside and outside the emitting region.

From the analysis of these multi-frequency polarimetric data we find that 43% of the sources show polarized emission $> 1\%$ at all the available frequencies, while other 43% are completely unpolarized. In a sample of compact sources such a high percentage of highly polarized objects reflects a strong contamination by blazar radio sources.

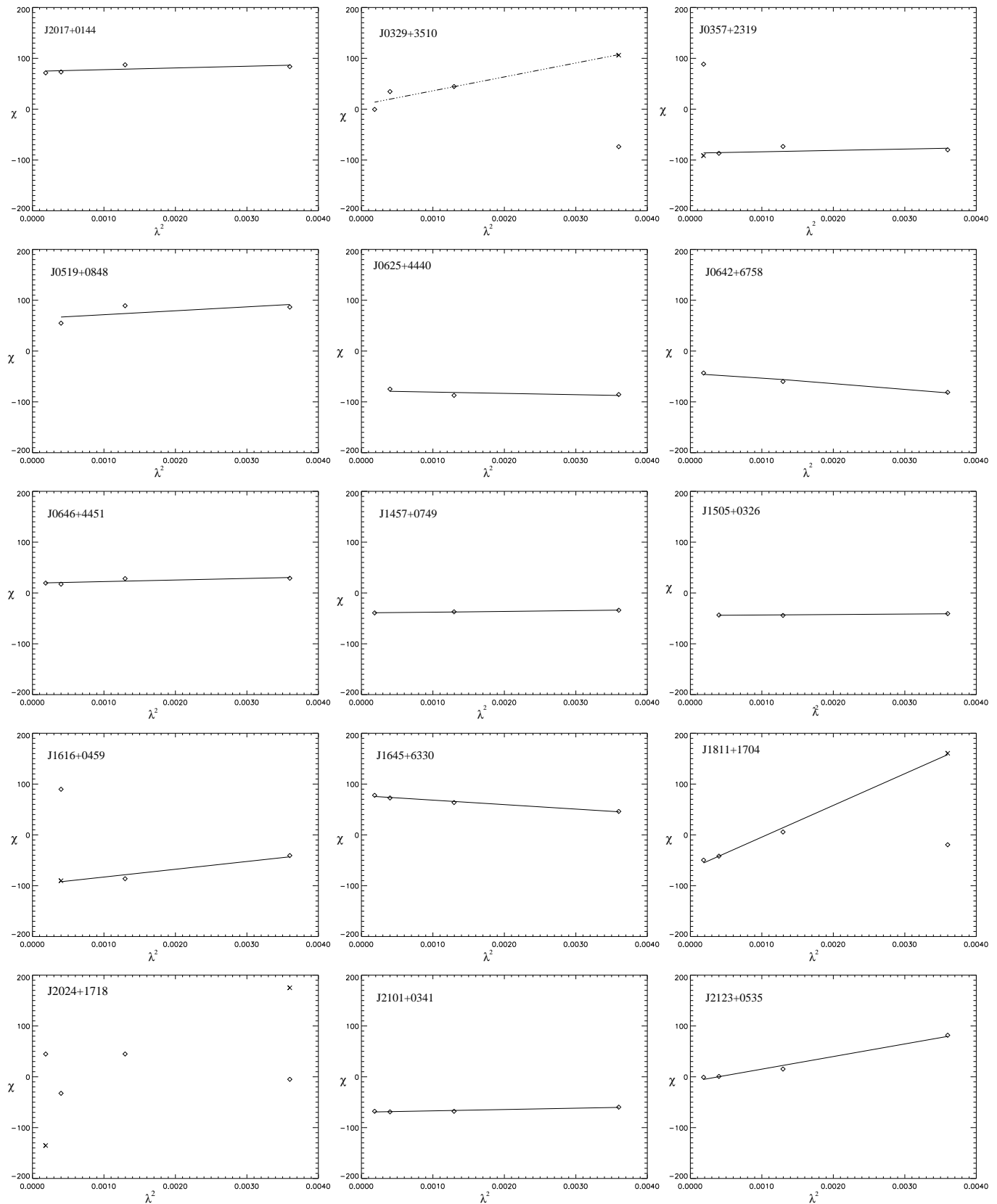


Figure 5.3: Fits of χ vs λ^2 for the 18 sources with χ measured at three or four frequencies. The diamonds represent the measured value of the polarization angle, while crosses indicate an addition of some $\pm n\pi$ ambiguities. In the case of the source J2024+1718 no RM could be fitted.

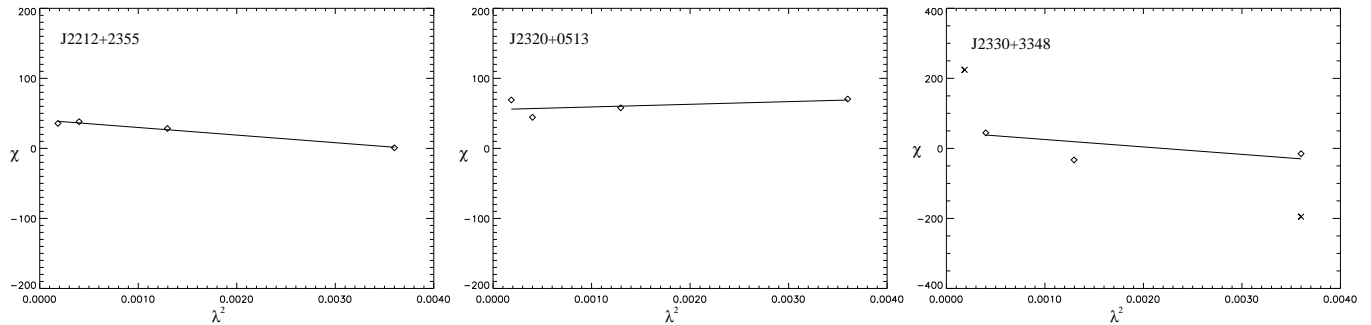


Figure 5.3: Continued.

In order to make the source classification more effective, the polarization properties are compared with flux-density and spectral-shape variability (§ 3; Tinti et al. 2005) and morphological information (§ 4, Orienti et al. 2006a).

The 89% of the unpolarized sources do not show any significant variability. On the contrary, the 94% of the highly-polarized sources have strong flux density variability and the 65% do not even show the convex shape of the spectrum in at least one of the observing epochs.

If the polarized emission is analyzed in relation to the pc-scale morphology (Orienti et al. 2006a), it results that HFPs with or without a CSO-like structure have different polarization properties: the 72% of the CSO-like sources are completely unpolarized at all frequencies, while the 60% of those without a CSO-like morphology have highly-polarized ($>1\%$) emission at each frequency.

All these pieces of evidence confirm the idea that the HFP sample is made of two different radio source populations. If all the selection “tools” described in § 3, 4, 5 are considered together, we obtain that a significant fraction (at least $\sim 60\%$) of the whole “bright” HFP sample is made of contaminant objects, and only the 40% can still be considered as young radio source candidates.

Chapter 6

Young radio sources and their ISM

The onset of radio activity is currently believed to be related to the availability and accumulation of fuel to feed the central Active Galactic Nucleus (AGN), likely provided by merger or accretion events in the host galaxy. As a result, the galaxy harbouring a radio source is likely to have a quite rich interstellar medium (ISM), at least during the initial phase of the radio emission and this is particularly true in the nuclear regions.

The presence of significant amount of gas in young radio galaxies is supported by a high incidence of HI absorption in these objects (Vermeulen et al. 2003; Pihlström et al. 2003) which is substantially larger than what typically found in the extended classical Doubles (Morganti et al. 2001), with typical linear sizes of hundred of kpc, and thus with radio-lobes mostly outside the ISM of the host galaxy.

Such a particular environment, although not dense enough to frustrate the radio emission for its whole lifetime, plays a major role in the growth and evolution of a small radio source. In the early-phase the radio emission resides within the innermost regions of the host galaxy and the jets have to make their way through the dense medium surrounding the nucleus.

During the expansion, it is possible that at least one of the jets impacts with a denser clump. A jet-cloud interaction usually produces a shock, which may then trigger a star formation (i.e. Begelman & Cioffi 1989) and/or maser processes. In particular, the OH-1720 MHz maser line is an indicator of interaction between radio plasma and molecular clouds (Lockett et al. 1999).

In this scenario young radio sources are the ideal targets to study the physical properties of the innermost regions of the Interstellar Medium, the role played by the ISM on the evolution of the radio emission as well as their interaction.

In this chapter I deal with the characteristics of the ISM by means of the study of the HI in absorption and the OH-1720 MHz maser line. Then I investigate whether the ISM can influence the source evolution, for instance by temporarily trapping or at least slowing down the source growth.

6.1 Young radio sources and HI absorption

The study of the 21-cm line of the atomic hydrogen in absorption provides important information on the neutral gas content of radio sources. The absorption observations have the advantage that the sensitivity is independent of the distance, depending only on the presence of a strong enough background radio source.

The strength of young radio sources, together with their compact sizes makes them good targets to trace the dense gas confined within the innermost regions of the host galaxy.

Statistical studies of the HI in absorption in a sample of CSS/GPS sources (Pihlström et al. 2003) have led to the discovery of an anti-correlation between the HI column density and the linear sizes ($N_{\text{HI}} \propto LS^{-0.43}$, Fig. 6.1a solid line): the smaller the source (<0.5 kpc), the larger the HI column density is. This result can be explained in a torus/disk scenario (Fig. 6.1b, from Mundell et al. 2003). In this case, the HI absorption is detected against the receding jet, when our line of sight passes through the circumnuclear disk/torus along its way toward the radio emission. As the radio source grows, the background emission of the counter-jet moves toward the outer and less dense part of the atomic structure, producing therefore a decrement of the HI column density. Furthermore, as the source grows its surface brightness decreases since the total energy is diluted over a larger area. Such a decrement of the flux-density of the background source requires larger amount of HI to be revealed.

Evidence of HI associated with circumnuclear disks and tori has been reported in some of the CSS/GPS (i.e. J0119+3210 (alias 4C 31.04) by Conway 1996; B1946+708 by Peck et al. 1999). The geometry and kinematic of HI distribution has been derived on the basis of pc-scale resolution images detecting several line profiles and different systemic velocities at various locations across the radio source. Surprisingly, the neutral hydrogen has been recently found to be associated also with fast outflows (Morganti et al. 2005), which have been interpreted in terms of

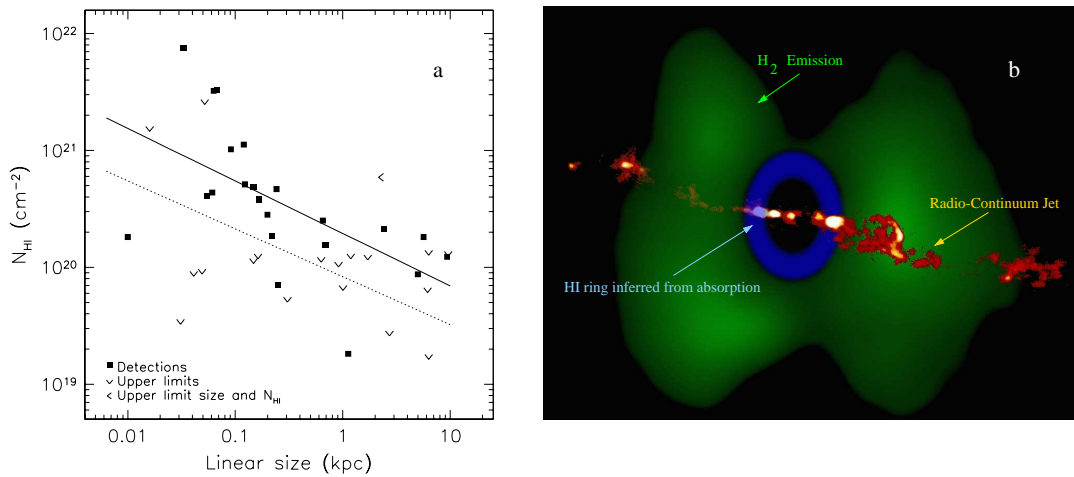


Figure 6.1: *a*: Absorbed HI column density versus projected linear size for CSS/GPS sources (Pihlström et al. 2003). The solid line represents the relationship $N_{\text{HI}} = 1.95 \times 10^{20} \text{LS}^{-0.45}$ where LS is in kpc, obtained considering detections only. The dotted line represents the relationship if also upper limits are taken into account. In this case $N_{\text{HI}} = 7.2 \times 10^{19} \text{LS}^{-0.43}$. *b*: A cartoon of the HI absorption in a torus-like scenario (Mundell et al. 2003)

interaction between the radio jet and a clumpy, unsettled ISM.

Given their young ages (even younger than GPS/CSSs studied so far) and their extremely compact sizes, genuine HFP sources are the ideal tool to investigate the characteristics of the ISM of the innermost regions of the host galaxy, and to determine whether such a medium is already organized in settled structures, such as circumnuclear disks/tori, or it is still unsettled in a clumpy phase.

6.1.1 WSRT observations of genuine HFPs

A radio source selection made of genuine young objects only, is of primary importance in order to perform a solid statistical analysis of the properties of their ISM.

In order to investigate the presence of HI in absorption in HFPs, a sub-sample of 6 objects has been selected (Table 6.1). The selection was based on:

1) the results obtained by the study of the discriminant properties (i.e. variability, morphology and polarization; § 3, 4 and 5) which characterize the nature of different

radio source populations, and only confirmed young radio sources have been selected; 2) the redshifted HI line must fall at frequencies suitable to be observed by the WSRT receivers and free of radio interference (RFI).

The availability of wide (20 MHz) and sensitive receivers together with the possibility to observe frequencies from 1.4 GHz down to a few hundred MHz, makes the WSRT the best instrument for the HI detection at redshift > 0.2 , when the shifted HI-line does not fall anymore within the frequency window of most radio interferometers like the VLA.

The WSRT observations have been carried out in different runs from 29 January to 12 September 2005 in dual orthogonal polarization mode. Two sources in the sample were already known to possess HI absorption: J0111+3906 (Carilli et al. 1996) and J1407+2827 (alias OQ 208; Vermeulen et al. 2003; Morganti et al. 2005). In these two sources, the goal of the new observations was to investigate the possible presence of variability in the HI profile and/or a broad component in their absorption spectrum.

Of the 6 observed sources in Table 6.1, those with $z < 0.3$ have been observed for 6 hours each, using the L-band receiver, with 1024 spectral channels covering a 20 MHz wide observing band. Sources with redshift higher than 0.4 have been observed using the UHF-high band, with 1024 spectral channels. Since the UHF-high band is affected by a higher noise level than that in the L-band, a longer observing time of 12 hours is required in order to achieve the same sensitivity as the L-band. The 20 MHz band led the coverage of the velocity range around the velocity centroid of about ± 2200 km/s at $z=0.07$ and ± 3500 km/s at $z=0.6$. Only the source J0003+2129 was observed with a 10-MHz wide band ($\sim \pm 1500$ km/s), since known RFI would have affected a wider bandwidth. Table 6.1 summarizes the observational and physical parameters of the observed sources.

The data reduction was carried out using the MIRIAD package. The quasars 3C 286, 3C 48 and 3C 147 were observed to calibrate the absolute flux density scale and the bandpass profile. Data were inspected for time-limited and baseline specific interference, and bad data were removed before solving for the gain- and bandpass calibrations.

The two orthogonal polarization were added together to improve the signal-to-noise ratio of the final spectrum. The continuum subtraction was done by using a linear fit

through the line-free channels (i.e. all the channels outside a range of ± 1000 km/s from the centroid velocity) of each visibility record and subtracting this fit from all the frequency channels (using the MIRIAD task “UVLIN”). Particular attention was paid in the case of OQ208 where a shallow absorption has been previously detected. After several attempts, for this source the final continuum subtraction was obtained using as line-free those channels outside the range $-1800/+600$ from the centroid frequency. The baselines of the spectra obtained after the continuum subtraction resulted flat, indicating that no broad and shallow line features have been included.

After the continuum subtraction, line cubes were produced using uniform weighting Hanning smoothing and inspected. For the two sources where HI absorption was detected (J0111+3906 and OQ208), the spectra obtained at the location of the peak of the radio continuum are shown in Figs. 6.2 and 6.4. For each source, the r.m.s. noise was estimated from the line cube and the values are reported in Table 6.1.

In order to make a reliable comparison between these values and what found in CSS/GPS samples, the upper limits to the optical depth and the HI column density have been computed following Vermeulen et al. (2003), i.e. assuming a peak corresponding to 2σ noise level, a line width of 100 km/s and T_{spin} of 100 K.

Finally the line-free channels were used to produce a continuum image of each source. The continuum emission is always unresolved at the resolution of the WSRT (typically about $20''$), with the only exception of J0111+3906 known to possess a relatively weak component on such angular scale (Baum et al. 1990; Tinti et al. 2005). The continuum emission derived from these data is slightly resolved to the East, consistent with the large-scale emission seen by Baum et al. (1990).

6.1.2 Results

Among the six galaxies observed, HI absorption has been detected only in the two sources (J0111+3906 and J1407+2827 alias OQ208) in which the presence of the absorption was already reported by previous studies. Furthermore, HI in emission has been found in two companion galaxies of J0655+4100 which occurs at almost the same redshift, a clear indication of a physical group. Below I discuss these three objects in more detail.

Source J2000 (1)	LS pc (2)	z_{opt} (3)	ν_{obs} MHz (4)	Resol. km s ⁻¹ (5)	r.m.s. mJy/b/ch (6)	S _{obs} mJy (7)	S _{HI} mJy (8)	τ_{peak} (9)	Δv km s ⁻¹ (10)	Log(N _{HI}) (11)	$z_{\text{HI,peak}}$ (12)
J0003+2129	22	0.452	977.96	4.3	6.1	50	<12.2	<0.15		<21.43	
J0111+3906	22 ^a	0.668	851.32	6.9	2.8	170	52.7	0.44	100	21.90	0.6687
J0655+4100	<1	0.02156	1390.03	4.3	0.7	239	<1.4	<0.006		<20.0	
J1407+2827	10	0.0766	1318.60	4.5	1.1	826	5	0.005	1800	20.9	0.0769
J1511+0518	7	0.084	1309.96	9.5	1.1	80	<2.2	<0.02		<20.6	
J1623+6624	<1	0.203	1180.38	4.5	0.7	129	<1.4	<0.01		<20.3	

Table 6.1: Physical and observational parameters of the 6 HFP galaxies observed with WSRT. Columns 1: source name; Column 2: projected linear sizes (Orienti et al. 2006a); Column 3: optical redshift; Column 4: central frequency; Column 5: channel resolution; Column 6: 1σ noise level in the line cube; Column 7: continuum flux density taken from our WSRT data at the observed frequency; Column 8: peak flux density of the absorption line, measured on the spectral image; Column 9: optical depth; Column 10: the width of the HI absorption line: for J0111+3906 the FWHM is given, in the case of OQ 208 we give the FWZI, due to the complexity of the line profile. Column 11: HI column density derived from $N_{\text{HI}} = 1.82 \times 10^{18} T_{\text{spin}} \tau_{\text{peak}} \Delta v \text{ cm}^{-2}$, a T_{spin} of 100 K has been assumed; Column 12: the redshift of the peak HI absorption. The line flux density, the optical depth and the HI column density upper limits have been computed assuming the 2σ noise level, a line width of 100 km s⁻¹ and T_{spin} of 100 K, as in Vermeulen et al. (2003). *a*: For the source J0111+3906, the projected linear size is taken from Owsianik et al. (1998b).

Evidence of a circumnuclear structure: the case of J0111+3906

The radio source J0111+3906 is associated with a narrow emission line galaxy at $z=0.668$ (Carilli et al. 1998). Although this source is classified as a CSO due to its pc-scale morphology (Taylor et al. 1996), it also shows an extended emission on the kpc-scale interpreted in terms of recurrency of the radio activity (Baum et al. 1990; Tinti et al. 2005, see Fig. 6.2 *left panel*).

HI absorption was already reported by Carilli et al. (1998), based on narrow-band WSRT observations. We detect a strong HI absorption line peaking at $\nu_{\text{HI,p}}=851.03$ MHz ($z_{\text{HI,p}}=0.6687$, see Fig. 6.2). HI absorption is only detected against the peak of the continuum, therefore coincident with the pc-scale structure. The line width is measured to be FWHM=100 km/s and the optical depth $\tau_p=0.44$. With these values, assuming a spin temperature of 100 K, we obtain an HI column density of $8.05 \times 10^{21} \text{ cm}^{-2}$. These results are in good agreement with those found by Carilli et al. (1998), indicating the absence of any significant variability between the two

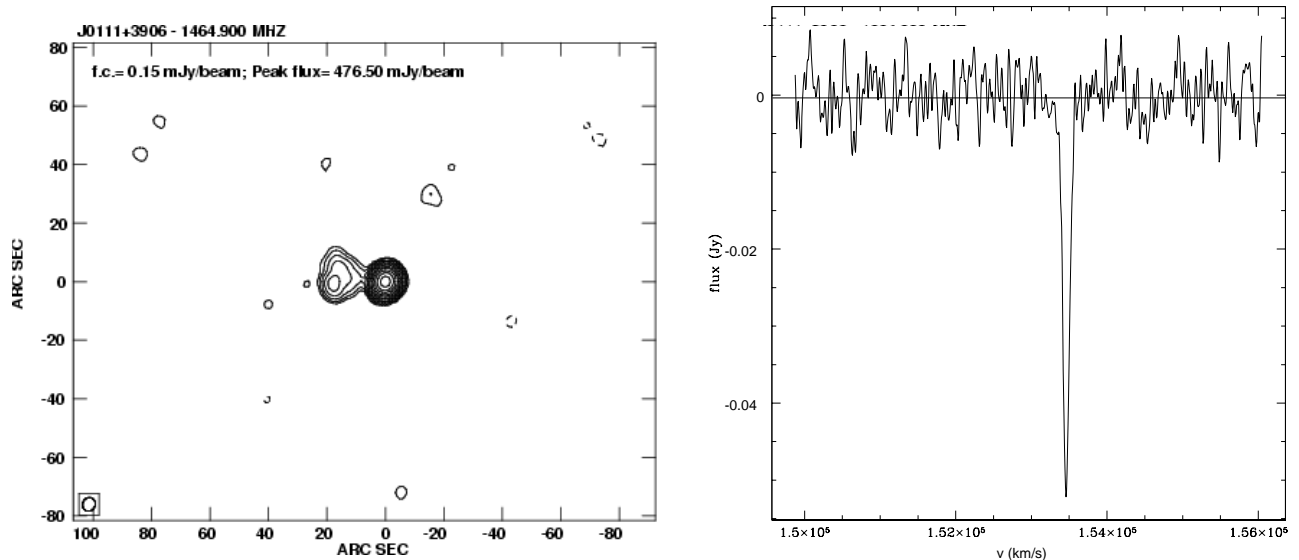


Figure 6.2: *Left panel:* VLA image at 1.4 GHz of the source J0111+3906. It is clearly visible a low-brightness extended emission on the Western part of the source (Tinti et al. 2005). *Right panel:* the HI absorption profile detected in J0111+3906. The velocity is in the optical heliocentric convention.

epochs.

No broad absorption (i.e. $\text{FWHM} > 100 \text{ km/s}$), with optical depth higher than $\tau_{2\sigma} \sim 0.03$ has been detected (Oriente et al. 2006b).

The HI absorption could in principle be due to unsettled foreground clouds. Using multi-epoch VLBI data spanning about 12 years, Owsianik et al. (1998b) estimated for this source a hot-spot separation velocity of $0.197c$. In the 8 years elapsed between these new observations and those from Carilli et al. (1998), the radio source should have grown of 0.3 pc. The lack of significant variability indicates that the absorbing medium does not have sub-structure on such scale.

In the Galactic ISM there are HI clouds of different size. The lack of variability excludes that the HI absorber is related to small AU-scale clouds (Brogan et al. 2005) and favours larger clouds like those associated to tidal debris (see e.g. Wakker et al. 2002).

However, the width of the absorption line ($\sim 100 \text{ km/s}$) is too broad compared with the typical values found for high velocity clouds (i.e. 4C 31.04; Conway 1999). Furthermore, the very high optical depth detected in J0111+3906 makes these clouds extremely unlikely as the absorber.

The characteristics of the absorption line can be better explained by means of a circumnuclear disk/torus. Indeed, the values derived from the spectra are similar to those found in other circumnuclear structures, such as in Cygnus A (Conway et al. 1995) and in the CSO 1946+708 (Peck et al. 1999). The detection of free-free absorption in J0111+3906 suggests the presence of a 100 pc radius nuclear disk with electron density of 500 cm^{-3} (Marr et al. 2001). The HI absorption could arise from the neutral hydrogen in the external parts of this structure.

Since the absorption is found across the pc-scale structure only, VLBI observations provide the unique possibility to identify the precise location where the absorption is occurring. Unfortunately, since the redshifted HI-frequency ($\sim 850 \text{ MHz}$) is covered only by the receiver of the WSRT, high-resolution observations searching for HI absorption cannot be carried out so far.

A clumpy medium: the case of J1407+2827 (OQ 208)

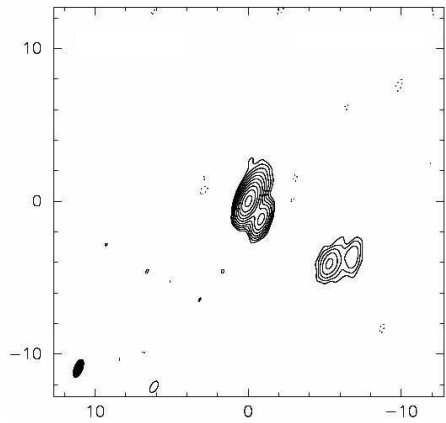


Figure 6.3: VLBA image at 15 GHz of the radio galaxy OQ 208 (Kellermann et al. 1998).

The radio source OQ 208 is associated with a broad emission line galaxy at $z=0.07658$. The radio structure is characterized by two compact lobes separated by $\sim 10 \text{ pc}$, highly asymmetric in terms of flux density ratio (Stanghellini et al. 1997). In the radio source OQ 208 a shallow ($\tau_p=0.005$) and very broad (FWZI $\sim 1800 \text{ km/s}$) HI absorption has been detected (Fig. 6.4a). This absorption extends from ~ 21650 to $\sim 23450 \text{ km/s}$, mostly blue-shifted as compared to the systemic velocity 22957 km/s derived from optical lines (Gallimore et al. 1999). The line profile has

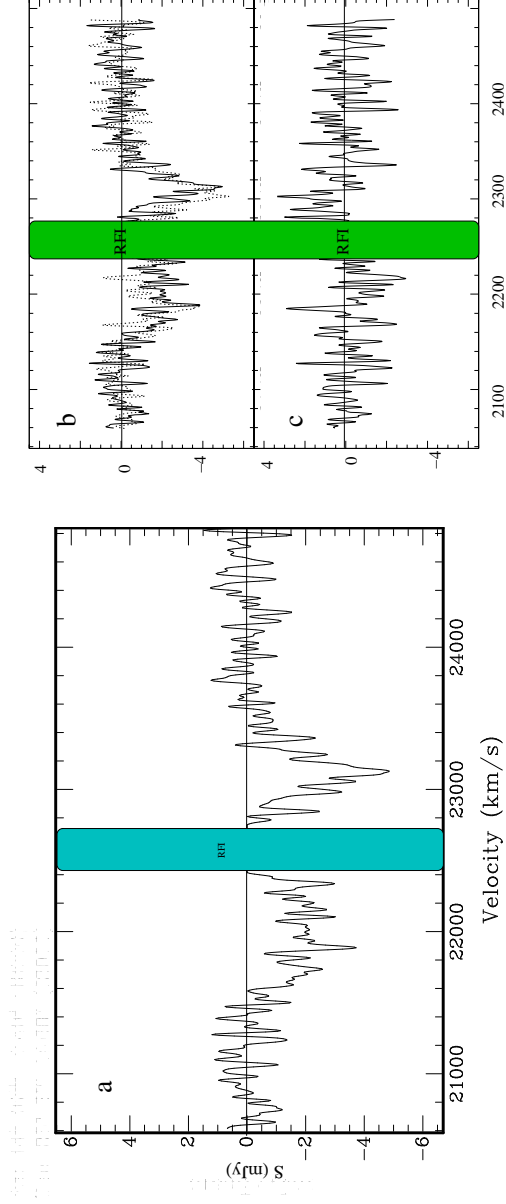


Figure 6.4: *a*: The HI absorption profile detected in OQ 208 from our new WSRT observations. The velocity is in the optical heliocentric convention. Strong RFI (*filled area*) is present in the line profile. *b*: The two-epoch line profiles of OQ 208 one superimposed to the other; the continuous line represents data from Morganti et al. (2005), while the dotted line represents these new data. *c*: the residuals obtained after subtracting the two-epoch line profiles.

a peak located at $\nu_{\text{HI,p}}=1318.6$ MHz ($z_{\text{HI,p}}=0.0773$). Assuming a T_{spin} of 100 K we obtain an HI column density of 8.0×10^{20} cm^{-2} .

The HI absorption was already detected by Vermeulen et al. (2003) and Morganti et al. (2005) though with different results. Vermeulen et al. (2003) found an HI absorption centred on the same frequency ($\nu_{\text{HI,p}}=1318.6$ MHz) as in these observations but with a width of 256 km/s only. The likely reason for such a discrepancy is the fact that the maximum available bandwidth (10 MHz) at the WSRT at the time of the survey of Vermeulen et al. (2003) was not large enough to allow the detection of broad features.

Gupta et al. (2006) re-observed OQ 208 with the GMRT, but with a narrower bandwidth (4 MHz), which did not allow them to detect the broad line-component. Their results are in good agreement with the line characteristics found by Vermeulen et al. (2003).

The presence of a broad HI absorption in OQ 208 was first reported by Morganti et al. (2005) and interpreted in terms of a fast outflow of neutral hydrogen possibly due to a jet-cloud interaction.

In this case the model assumes that the jet hits a (molecular) cloud in the ISM ionizing the gas by shocks. As the shock passes away, part of the ionized gas may have the chance to recombine and become neutral again while it is still moving at high velocity, originating the observed absorption.

Fast outflows of highly ionized gas have been detected in the optical (e.g. in 3C 293, Emonts et al. 2005). The detection of such fast outflows of neutral gas indicates that the gas can cool very efficiently, as suggested by numerical simulations (Mellema et al. 2002).

Fig. 6.4b shows the comparison between the HI profile derived from the observations presented here (dotted line) and those from Morganti et al. (2005; continuum line). In Fig 6.4c the residuals obtained after subtracting the profiles taken at the two epochs are shown. No significant evidence of changes in the HI profile have been detected with a corresponding optical depth upper limit of $\tau \sim 0.002$ (Oriente et al. 2006b).

It is worth mentioning that in OQ 208 X-ray observations (Guainazzi et al. 2004) proved the presence of a Compton-thick obscured AGN. As suggested by Guainazzi et al. (2004) in this source the jets are likely piercing their way through this Compton-thick medium which is pervading the nuclear environment. The outflow detected in HI could be used as a further evidence supporting this process.

J0655+4100: young radio source in a group of galaxies

Although no evidence of neutral hydrogen gas has been found in the radio galaxy J0655+4100, an elliptical galaxy at $z = 0.02156$ ($V_{\text{sys}} = 6464 \text{ km s}^{-1}$; Marcha et al. 1996), HI in emission has been found in two nearby galaxies. One companion is the spiral galaxy UGC 03593 where, centered at 6694 km/s, $\sim 2 \times 10^9 M_{\odot}$ of HI have been detected. This galaxy is located at a projected distance of 65 kpc South-East of J0655+4100. The second companion displays a systemic velocity of 6334 km/s and is located to the North-West at a projected distance of 55 kpc from the HFP source. In the Digitized Sky Survey (DSS) image it is associated with a faint galaxy for which an HI mass of $\sim 2 \times 10^8 M_{\odot}$ has been estimated. This galaxy has not been previously cataloged¹. The two galaxies form a physical compact group

¹Based on results from the NASA/IPAC Extragalactic Database (NED).

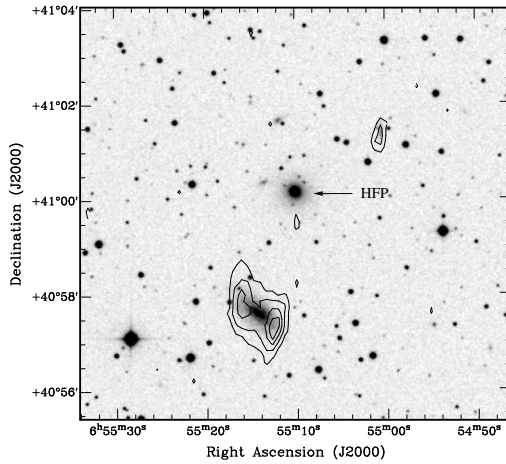


Figure 6.5: HI total intensity contours superimposed onto a DSS optical image centered on the radio galaxy J0655+4100. Two nearby galaxies with HI in emission are clearly detected. Contour levels are: 2.35 , 3.50 , 5.68 and 7.51×10^{20} atoms cm^{-2} .

with J0655+4100 (Fig. 6.5) supporting the idea that young radio sources reside in groups, as suggested by other works (Stanghellini et al. 1993) based on the excess of galaxy density in the optical images of GPS radio sources.

6.1.3 Discussion

The detection of HI absorption in only two of the six observed galaxies is somewhat surprising. From the analysis of a sample of 41 CSS/GPS radio sources, Pihlström et al. (2003) have found an inverse correlation between the source linear size and the HI column density: smaller sources (< 0.5 kpc) have larger HI column density than the larger sources (> 0.5 kpc). Furthermore, Fig. 6.1a also shows the existence of a correlation between the detection of HI absorption and the projected linear size: the smaller the source, the higher the probability to detect HI absorption is.

With new observations carried out with the GMRT Gupta et al. (2006) confirm such a trend.

Following this correlations, one would have expected very high N_{HI} in the smallest sources, like HFPs.

Fig. 6.6 shows the inverse correlation found by Pihlström et al. (2003) with the addition of the values obtained from the sources discussed here. The sensitivity

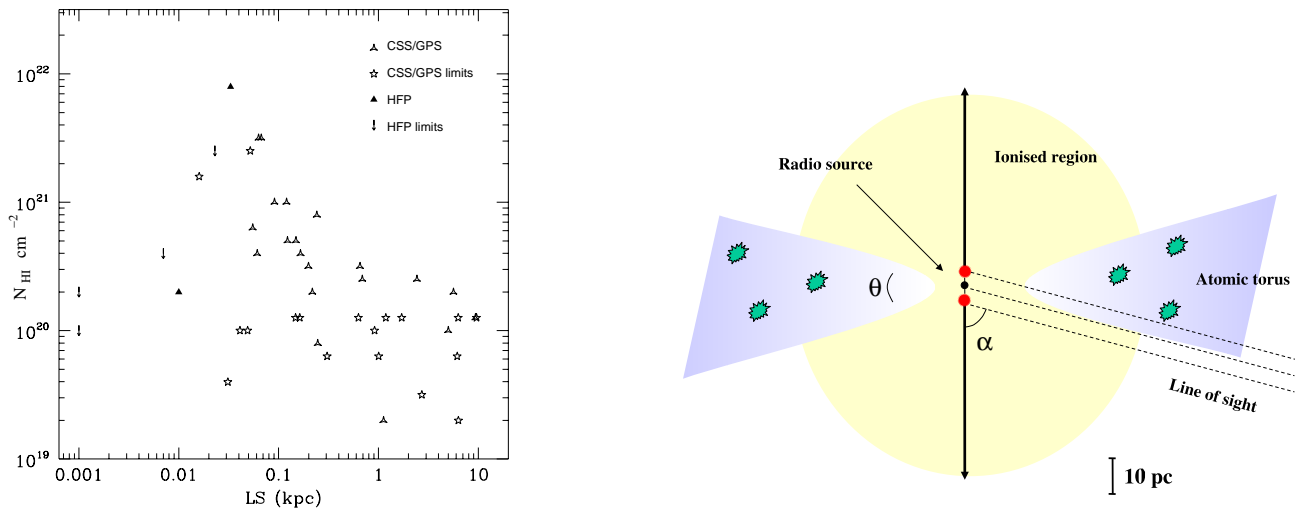


Figure 6.6: *Left:* Absorbed HI column density versus projected linear sizes. The HFP galaxies do not seem to follow the trend found for CSS/GPS sources. The CSS/GPS values have been taken from Pihlström et al. (2003). *Right:* Cartoon of a possible orientation of the HFP sources and circumnuclear torus. The toroidal structure is perpendicular to the source axis. The torus model is dependent on the opening angle θ and the viewing angle α . The scale shown is approximate: the inner radius of the torus and the sizes of the denser clumps are not known.

reached by the new observations enables us to set tight upper limits to the N_{HI} for the sources with no HI detection. Interestingly, in the HFP sub-sample the smallest sources (with size ≤ 10 pc) appear to deviate from the extrapolation of the trend found by Pihlström et al. (2003). Given the limited number of objects, it is not possible to establish whether for very compact radio sources a break down of such correlation occurs. If we consider that 15 out of 41 sources of Pihlström et al. (2003) sample have HI column density below $2 \times 10^{20} \text{ cm}^{-2}$, the probability to find two sources randomly chosen both below such limit is $\sim 13\%$. This means that the small column density is possibly a feature typical of extremely young radio galaxies. We also point out that the correlation from Pihlström et al. (2003) has a large scatter, and upper limits to the column density are present at all linear sizes. With all this in mind, it is interesting to consider the possible origin of the lack of HI absorption found in J0655+4100 and J1623+5524 (the two 1-pc objects).

The trend observed by Pihlström et al. (2003) has been explained with both a spherical and axi-symmetric gas distribution, with a radial power-law density profile, as well as a disk model. Indeed, a torus-like distribution of neutral gas has been

found to be consistent with the observations in a number of GPS sources (e.g. 4C 31.04 by Conway 1996; 1946+708 by Peck et al. 1999). In this scenario, the absence of high HI column density in very compact sources can be explained by both the orientation and the extreme compactness of the sources. Within the framework of the AGN unification scheme, the central engine is surrounded by a disk of ionized gas and shielded by a torus of atomic and molecular gas (i.e. Urry & Padovani 1995). Evidence of ionized disks with radii between a few tens and one hundred pc has been claimed in this class of sources (Kameno et al. 2000), as responsible of free-free absorption in the optically thick region of the radio spectrum, although an unambiguous evidence of such absorption could not be found.

The fundamental ingredient to trace HI absorption is the presence of background flux density. Given the extremely small linear sizes of the HFP sources (see Fig. 6.6 and Table 6.1), the line of sight likely passes mainly through the ionized region, piercing the torus only in its very inner part, if we are looking at the receding lobe. This could be the case if the torus axis is aligned to the radio jet, and its half-opening angle is, for example, $\theta \sim 20^\circ$ (as illustrated in Fig. 6.6), consistent with the constraint $\theta \leq 30^\circ - 40^\circ$ by Granato et al. (1997), and an orientation of the line of sight between 45° and 70° (with respect to the radio jet).

It should be noted that the gas closer to the central engine is hotter, both in terms of kinetic and spin temperature, therefore a longer path length would not necessarily imply a higher optical depth. Moreover, recent work by Hatziminaoglou et al. (2006) focused on the properties of the dusty tori in AGN, has shown the possible existence of tori with low optical depth. Therefore, in this scenario, it is possible that for these sources of a few pc in size (or even less), we are missing the HI absorption due to both sensitivity limitations and orientation effects.

As described in § 6.1, in addition to the presence of circumnuclear tori, in such young radio sources one could have expected to detect also the presence of unsettled gas, i.e. gas not necessarily located in a circumnuclear torus or disk-like structure but still enshrouding the radio source, such as the clumpy component of the Narrow-Line Region.

No evidence for such an unsettled medium has been found. Again, this could be partly due to the very small emitting area of the background radio source, that

decreases the probability to detect the absorption. Clouds indicating the presence of a rich and clumpy interstellar medium in the centre of the radio source have been found, as in the case of 4C 12.50 (Morganti et al. 2004) and 3C 49 and 3C 286.3 (Labiano et al. 2006). In 4C 12.50 a cloud of $\sim 20 \times 60$ pc has been detected: such a cloud, if properly located along the line of sight, would have covered most of the HFPs in the sample. Thus, these results are possibly indicating that the covering factor of such clouds is low, as it could be the case in 4C 12.50.

Finally, the great majority of the fast outflows detected in both pc- and kpc-scale radio galaxies have an HI optical depth of only $\tau < 0.006$ (Morganti et al. 2005). These observations are not sensitive enough to reach such a low values due to receiver sensitivity, therefore the lack of detection of broad absorption (except for the case of OQ 208 where the continuum is indeed strong enough to allow a good sensitivity) indicates that HI outflows are characterized by low optical depths.

6.2 Extragalactic hydroxyl: jet-cloud interaction?

Extragalactic Maser emission from hydroxyl molecules (OH) was first detected in the early eighties (i.e. Baan 1985). Galaxies displaying Maser emission show enhanced core activity in the form of nuclear starburst or an Active Galactic Nucleus.

Maser emission takes place when an overpopulation of an excited molecular level is produced via pumping to a higher energy level. The lifetime of the excited level is relatively short and the de-excitation to an intermediate energy level with a longer lifetime takes place almost immediately, which results in the overpopulation of that state.

In a cloud, when a photon interacts with an atom or a molecule that is in such an excited state, the photon can de-excite this state, triggering the emission of another photon moving in the same direction. This process can lead to the intense coherent radiation in the direction of the original photon and originates a Maser which is highly anisotropic.

So far, hydroxyl maser emission has been detected at several rotation levels. The ground state transitions, where most of the research has been done, comprise four maser lines: the main lines at 1665 and 1667 MHz, and the satellite lines at 1612 and 1720 MHz.

The pumping mechanism of these lines is related to the presence of intense infra-

red radiation fields (e.g. Elitzur 1992). Indeed, OH-maser emission is commonly observed in star-forming regions.

The only exception is the OH-1720 MHz line, which is the least commonly observed transition and it is usually found in supernova remnants. This is the only OH line which is pumped by a collisional mechanism induced by shocks (Lockett et al. 1999). In extragalactic radio sources this satellite line may be the tracer of the physical conditions during a jet-ISM interaction.

6.2.1 A WSRT search for OH-1720 MHz in HFPs

As the study of the HI in absorption provides important tools on the kinematic and distribution of the ISM, the detection of the OH-1720 MHz satellite line may give us strong clues on the physical conditions occurring during the interaction between the radio jet and the ISM.

For this purpose 7 HFPs have been observed with the WSRT. Such sources have been selected on the basis of:

- 1) the results obtained by the study of the discriminant properties (i.e. variability, morphology and polarization; § 3, 4 and 5) which characterize the nature of different radio source populations, and only confirmed young radio sources have been selected;
- 2) the redshifted 1720-MHz OH line must fall at frequencies suitable to be observed by the WSRT receivers and free of radio interference (RFI).

Source	ID	z	ν_{obs} MHz	Resol. km/s	$S_{1.7\text{GHz}}$ mJy
J0003+2129	G	0.452	1182.4948	5.0	120
J0428+3259	G	0.479	1163.3062	5.1	202
J0650+6001	Q	0.455	1182.4948	5.0	625
J0655+4100	G	0.02156	1684.2182	3.6	244
J1407+2827	G	0.0769	1597.6692	3.8	1100
J1511+0518	G	0.084	1587.2048	3.8	115
J1623+6624	G	0.203	1430.1995	4.2	175

Table 6.2: Physical and observational parameters of the 7 HFP sources observed. Column 1: source name; Col. 2: optical identification; Col. 3: optical redshift; Col. 4: central frequency; Col. 5: channel resolution; Col. 6: VLA total flux density at 1.7 GHz.

WSRT observations have been carried out in different runs from 29 July to 5 October 2005 in dual orthogonal polarization mode. Each source has been observed for two hours, using the L-band receiver with 512 channels and 10 MHz bandwidth.

The 10 MHz bandwidth led to the coverage of the velocity range around the velocity centroid of about ± 900 km/s at $z=0.02$ and ± 1300 km/s at $z=0.479$. Table 6.2 summarizes the observational and physical parameters of the sources.

The quasars 3C 48 and 3C 286 have been observed at the beginning and at the end of each observing run typically for 15 min each, to calibrate the absolute flux density scale and the bandpass profile. Data were inspected for time-limited and baseline specific interference, and bad data were removed before solving for the gain- and bandpass calibrations. The two orthogonal polarizations were added together to improve the signal-to-noise ratio of the final spectrum. The continuum subtraction was done by using a linear fit through the spectral channels expected to be without any line features (i.e. all the channels outside a range of ± 1000 km/s for the objects at highest redshift and ± 600 km/s for those at low redshift) of each visibility record and subtracting this fit from all the frequency channels (using the MIRIAD task “UVLIN”). The baselines of the spectra obtained after the continuum subtraction resulted to be flat, indicating that no broad and shallow features have been included. Then, line cubes were produced using uniform weighting Hanning smoothing and then were finally inspected. For each source, the 1σ noise level was estimated from the line cube and it is about 1.5-2.0 mJy for all the data cubes.

Despite the good signal-to-noise ratio reached by these WSRT observations, no OH-1720 MHz satellite line has been detected in any targets. This result does not imply the absence of jet-ISM interaction, but rather means that either the OH mass is not enough to be detected, or the shocks produced by the collision between the jet and the ISM are not efficient enough to trigger the maser emission.

Alternatively, given the large anisotropies related to this phenomenon, we can consider the possibility that the maser emission happens in directions not covered by our line of sight, as for HI (§ 6.1.3).

6.3 The X-ray emission in HFPS: the case of J1511+0518

The origin of the X-ray continuum in young radio sources as well as the role played by the warm gas in their growth is still not completely understood.

The discrimination between the thermal and non-thermal nature of the X-ray emission is the first step toward the knowledge of the physical mechanisms which are taking place. A non-thermal X-ray emission implies the Comptonization to be the dominant mechanism, as often found in blazars or even in a few unbeamed radio galaxies (Guainazzi et al. 2004). On the other hand, a thermal nature of the X-ray emission can provide important constraints on the physical properties of the warm gas responsible for such an emission, and its role played on the evolution of the radio emission.

So far there are not systematic studies of the X-ray properties in large samples of young radio sources. In past ROSAT observations, GPS galaxies appeared to have $L_X < 10^{44}$ erg/s and in some cases there were detection of the order of $L_X \sim 10^{42}$ erg/s (i.e. 4C12.50 and 2352+495, O’Dea et al. 1996b). Only recent studies of hard X-ray by *Chandra* and XMM-Newton observations of a small sample of GPS sources have shown that a significant fraction of the observed sources (80%) have X-ray luminosities of a few times 10^{44} erg/s, with an intrinsic column density $N_H > 10^{21.5}$ cm $^{-2}$ in addition to the Galactic absorption (Guainazzi et al. 2006).

Furthermore, Guainazzi et al. (2004) have found a Compton-thick ($N_{HI} \sim 10^{24}$ cm 2) medium pervading the HFP source OQ208. Although this ambient medium could interact with the expanding jet, its density is not enough to frustrate the source growth for its whole lifetime, causing the radio expansion to only slow down.

Among the candidate HFPS from the “bright” HFP sample which have been confirmed by the criteria described in the previous chapters (variability, morphology and polarization; § 3, 4 and 5), archival *Chandra* data are available only for the galaxy J1511+0518.

Although the short observing time (2 ks), there is clearly a detection which allows us to set tight constraints on the X-ray flux density of the source.

The best result is obtained by fitting the 0.5-10 keV with a single power-law with a photon index $\Gamma=1.83\pm 0.32$. This means an unabsorbed 0.5-10 keV flux density $\sim 1.23 \times 10^{-13}$ erg cm $^{-2}$ s $^{-1}$ and a galactic $N_{HI} \sim 3.4 \times 10^{20}$ cm $^{-2}$, which corresponds to

a 0.5-10 keV luminosity of $(2.15 \pm 0.86) \times 10^{42}$ erg/s. Given the short observing time it is not possible to unambiguously infer whether the emission is due to thermal or non-thermal mechanisms.

We start considering that all the X-ray emission comes from thermal emission from a warm gas ($T \sim 10^6$ - 10^7 K). Assuming that the radio emission is in equilibrium with its environment, we can constrain the density of the external medium by assuming a one-dimensional ram-pressure model (Eq. 1.6):

$$p_i \sim n_{ext} m_p v^2$$

where n_{ext} is the particle density of the external medium, m_p the proton mass, p_i the internal pressure of the radio source and v its advance speed. We assume that the ambient medium follows a King-profile (Eq. 1.8; Trinchieri et al. 1986), and that the hot gas completely resides within the core radius (< 1 kpc) where n_{ext} can be considered constant. Assuming the internal pressure found in § 4 in minimum energy condition (Oriente et al. 2006a), and the expansion velocity ~ 0.2 , as commonly derived for other young radio sources (i.e. OQ 208, Polatidis & Conway 2003), we find that n_{ext} must be $> 15 \text{ cm}^{-3}$ to be able to frustrate the source growth. In a hot ($T \sim 10^7$ K) gas this implies a $L_X > 2 \times 10^{44}$ erg/s, which is almost two orders of magnitude higher than what inferred from *Chandra* data.

We consider now the possibility that the X-ray emission is due to a non-thermal Inverse Compton mechanism. The high magnetic field (~ 0.1 G) derived from the radio observations in equipartition condition (§ 4) suggests that the X-ray emission can be likely due to Synchrotron-Self Compton (SSC). From the Comptonization in the X-rays of the synchrotron radiation we find:

$$L_{X,SSC} = \frac{24\pi L_{syn}^2}{AcH^2} \quad (6.1)$$

where $L_{X,SSC}$ is the X-ray luminosity due to SSC, L_{syn} is the bolometric synchrotron radio luminosity, A the emitting area, c the light speed and H the magnetic field. From the radio observations (see § 3 and 4; Oriente et al. 2006a) we obtain a bolometric radio luminosities $L_{radio} \sim 1.6 \times 10^{43}$ erg/s. If in Equation 6.1 we consider the information obtained from the radio observations (§ 4; Oriente et al. 2006a) we find a $L_{X,SSC} \sim 2.3 \times 10^{42}$ erg/s, in good agreement with the data.

6.4 Very asymmetric CSOs: influence of the ambient medium

High-resolution observations have shown that a significant fraction of two-sided young radio sources present very asymmetric morphologies, with very different arm-length and flux-density ratios between the two lobes (Saikia et al. 2001).

In cases where the core component has been unambiguously identified, it is possible to measure the expansion velocity of each jet separately. In some cases apparent differences between the two lobes are seen (e.g. 1943+546, Polatidis & Conway 2003). Assuming that both jets are powered in the same way, such a difference implies that jet expansions may vary during the source lifetime. Temporary variations could be produced by hydro-dynamically introduced internal pressure changes or changes in external density.

To investigate such possibilities the radiative age is used to derive the individual hot-spot advance speeds in the two very asymmetric CSOs B0147+400 and B0840+424 from the B3-VLA CSS sample (Fanti et al. 2001).

6.4.1 Observations and data reduction

Pc-scale resolution observations were carried out in two different runs using the VLBA plus a single VLA antenna, on September 6th (B0147+400) and November 24th (B0840+424), in full polarization mode with a recording bandwidth of 16 MHz at 128 Mbps, for a total of 18 hours. Each source was observed at 1.4 and 1.6 GHz (L band), 4.5 and 4.9 GHz (C band), 8.1 and 8.5 GHz (X band).

The correlation was performed at the VLBA correlator in Socorro, and data reduction was carried out with the NRAO AIPS package. After the application of the system temperature and antenna gain information, the amplitudes were checked using data on DA 193 (J0555+398) which is unresolved on a large subset of baselines at all frequencies, and whose flux density is monitored at the VLA in C and X bands. In both observations the sources DA 193 and J0927+3902 were both used to generate the bandpass correction.

The error on the absolute flux density scale can be estimated within 3% - 5% on the basis of the fluctuations of the amplitude gain solutions.

In C and X bands the instrumental polarization was removed by using the AIPS

Source	Comp.	S _L mJy	S _C mJy	S _X mJy	α_L^C	α_C^X	θ_{maj} mas	θ_{min} mas	p.a. °
B0147+400	S	208	157	122	0.3	0.5	2.4	2.2	126
	C		15	19		-0.5	1.5	0.3	176
	N	243	77	24	1.1	2.3	11.0	6.0	120
B0840+424	S	208	68	36	1.0	1.2	26.0	14.0	160
	C		31	31		-0.03	5.0	2.6	161
	N	968	410	252	0.8	0.9	6.9	2.9	176

Table 6.3: VLBA observations parameters of the sources B0147+400 and B0840+424. Column 1: source name; Col. 2: source component; Col 3, 4 and 5: the VLBA flux density measured in L, C and X bands; Col. 6 and 7: spectral indices between L and C bands, and between C and X bands; Col. 8 and 9: deconvolved angular size of the major and minor axis; Col. 10: the position angle of the major angle.

task PCAL; the absolute orientation of the electric vector of DA 193 and J0927+3902 was compared with the VLA/VLBA polarization calibration database to derive the corrections. The values derived from the two sources were in excellent agreement ($\leq 2^\circ$). The calibration of the instrumental polarization was not performed for the L band data.

The images at each individual frequency were obtained after a number of phase-only self-calibration iterations and they are presented in Fig. 6.7. Stokes' U and Q images were produced by using the final dataset.

As the last step images at all the 6 frequencies have been produced using natural grid weighting and the same *uv-range* common to all observing frequencies for each source (1.05 - 41 M λ and 0.88 - 40 M λ for B0147+400 and B0840+424 respectively), in order to have almost the same *uv* and image sampling, as well as the restoring beam.

For each source these *low-resolution* images were combined to produce a multi-frequency data cube, which was then analyzed by the Synage++ software (Murgia 2000) for subsequent spectral studies. Image registration was checked by comparing the location of optically thin bright features.

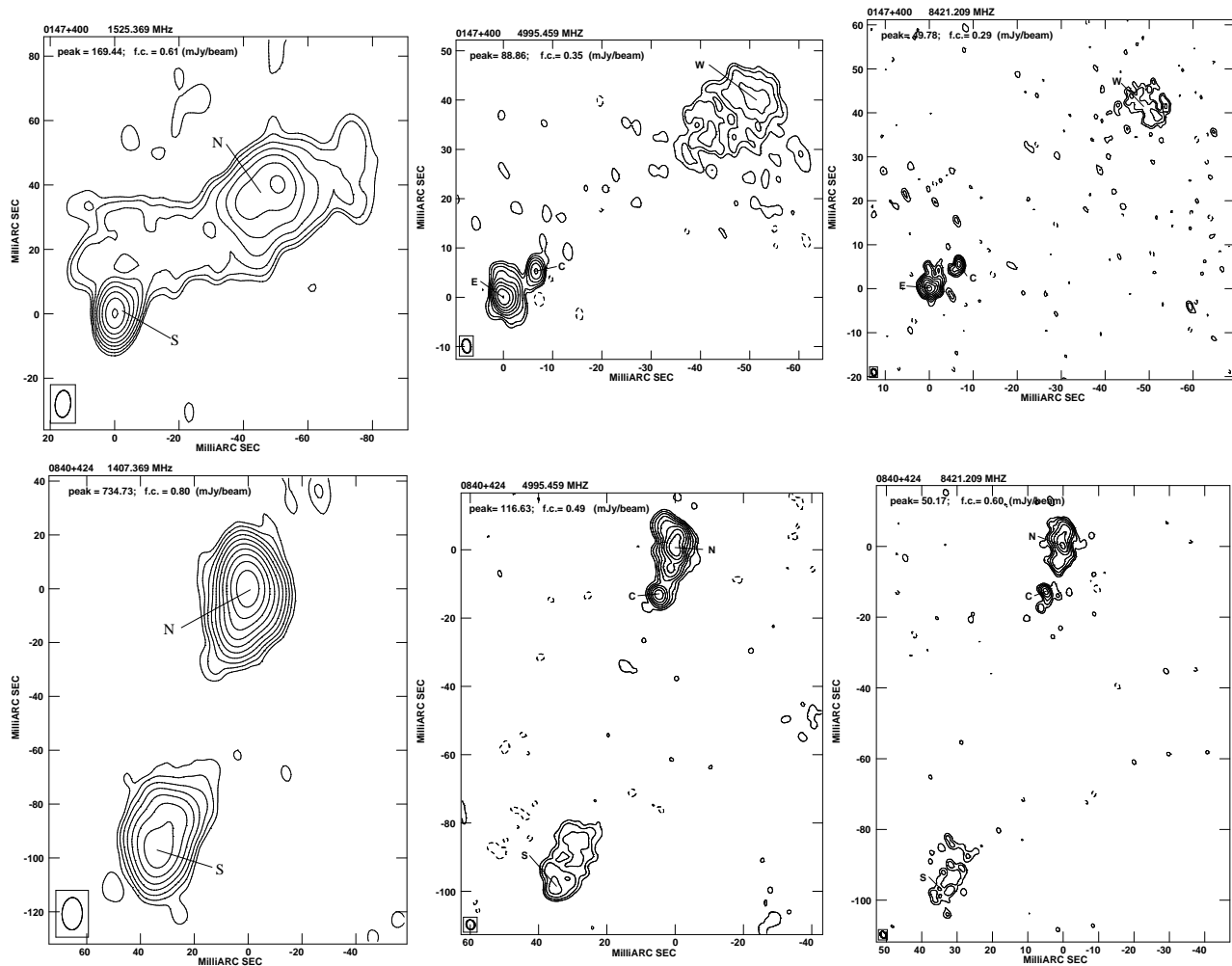


Figure 6.7: VLBA images in L, C and X bands of the sources B0147+400 (*upper panel*) and B0840+424 (*lower panel*). For each image we give the following information on the plot itself: **a)** peak flux density in mJy/beam; **b)** first contour intensity (*f.c.*) in mJy/beam, which is generally 3 times the rms noise on the image plane; contour levels increase by a factor of 2; **c)** the restoring beam is plotted on the bottom left corner of each image.

6.4.2 Multi-frequency spectral analysis

Synchrotron spectral ageing is based on the determination of the spectral break, which occurs at progressively lower frequencies as time passes. According to various source growth models (e.g. JP, Jaffe & Perola 1974; KP, Kardashev 1962; Pacholczyk 1970), relativistic electrons located in different regions have been deposited at different times, and the electron age measures locally the time elapsed since their production and/or latest acceleration (t_{syn}) when they crossed the hot-spot during its outward motion. The radiative age can be easily computed once the break frequency (ν_{br}) and the magnetic field (B) are known:

$$t_{syn} \propto B^{-3/2} \nu_{br}^{-1/2}. \quad (6.2)$$

So far, most if not all the works on the measurement of the source radiative age are based on the spectral break derived from the source integrated spectra (Murgia et al. 1999). One disadvantage of this approach is that the contributions of the various source components (core, jets, hot-spots and lobes), each one with its own spectral shape, are all mixed together. The brightest component is the one that influences the age determination the most; if we consider a source whose emission is dominated by the hot-spots where electrons are likely to be re-accelerated, the spectral age derived can be completely unrelated to the source age.

On the other hand, the radiative age of the back-flow tail in the lobes measures the time elapsed since the last acceleration, namely when the hot-spot crossed this location during its outward expansion. The best (i.e. oldest) measurement of the radiative age then comes from the innermost edges of the lobes where the electrons were deposited at the very beginning.

A previous work on the spectral ageing in two CSOs (Murgia 2003) has shown that the break frequency decreases if we move from regions near the hot-spot toward those located at the inner edges of the lobes, in the core direction. This is consistent with the dynamical scenario in which the source is expanding with time and the principal site of particle acceleration is the hot-spot.

Using multi-frequency images with pc-scale resolution it is possible to distinguish regions where electrons are injected/accelerated (core, hot-spots) from those in which electrons age (lobes). However, spectral index imaging is a quite hard task for VLBI experiments, since it is difficult to obtain well-matched uv -coverages at the

various observing frequencies. In particular there is a lack of short spacing at high frequencies, which sample the largest components, i.e. the inner edges of the lobes. In these VLBA observations, the addition of a single VLA antenna makes the differences in the sampling density at short spacing less effective, allowing the production of high-resolution spectral index images. The availability of 6 independent frequencies allows the determination of the nature of each component and thus the source age by fitting the spectra in each resolution element with the appropriate model.

Indeed, although radiative losses always imply a high-frequency steepening, the local spectral shape is strongly related to the evolution of the emission from an electron population and by the possible presence of injection of fresh relativistic particles. For example, in the hot-spots one would expect that the observed spectra are well fitted by models predicting a continuous injection of fresh particles, while lobes and extended features are better fitted by single-injection models (i.e. JP and KP).

6.4.3 Constraining the age from the radio spectra

A detailed spectral ageing study is performed on the CSO sources B0147+400 and B0840+424 from the B3-VLA CSS sample (Fanti et al. 2001). Both radio sources are characterized by a weak core and two very asymmetric, both in arm-length ratio and brightness, well-resolved mini-lobes. In B0147+400 the two mini-lobes lie roughly in SE-NW direction, and are connected by an extended, steep-spectrum ($\alpha > 2$) bridge visible in the L band only (Fig. 6.7), while in B0840+424 the mini-lobes are deployed roughly in the NS direction.

In the standard source model, the brightest component is also the farthest from the core, since differences in brightness and arm-length ratio are usually due to beaming effects and path delay. In a radio galaxy where the radio axis is oriented at large angles to the line of sight, such asymmetries are expected to be quite small, with expected ratios around 1. On the contrary, in these two CSOs, the brightest lobe is the one closest to the core, while the faintest is much farther away, suggesting a strong influence likely exerted by the ambient medium, which can be quite complex and inhomogeneous on such small scales.

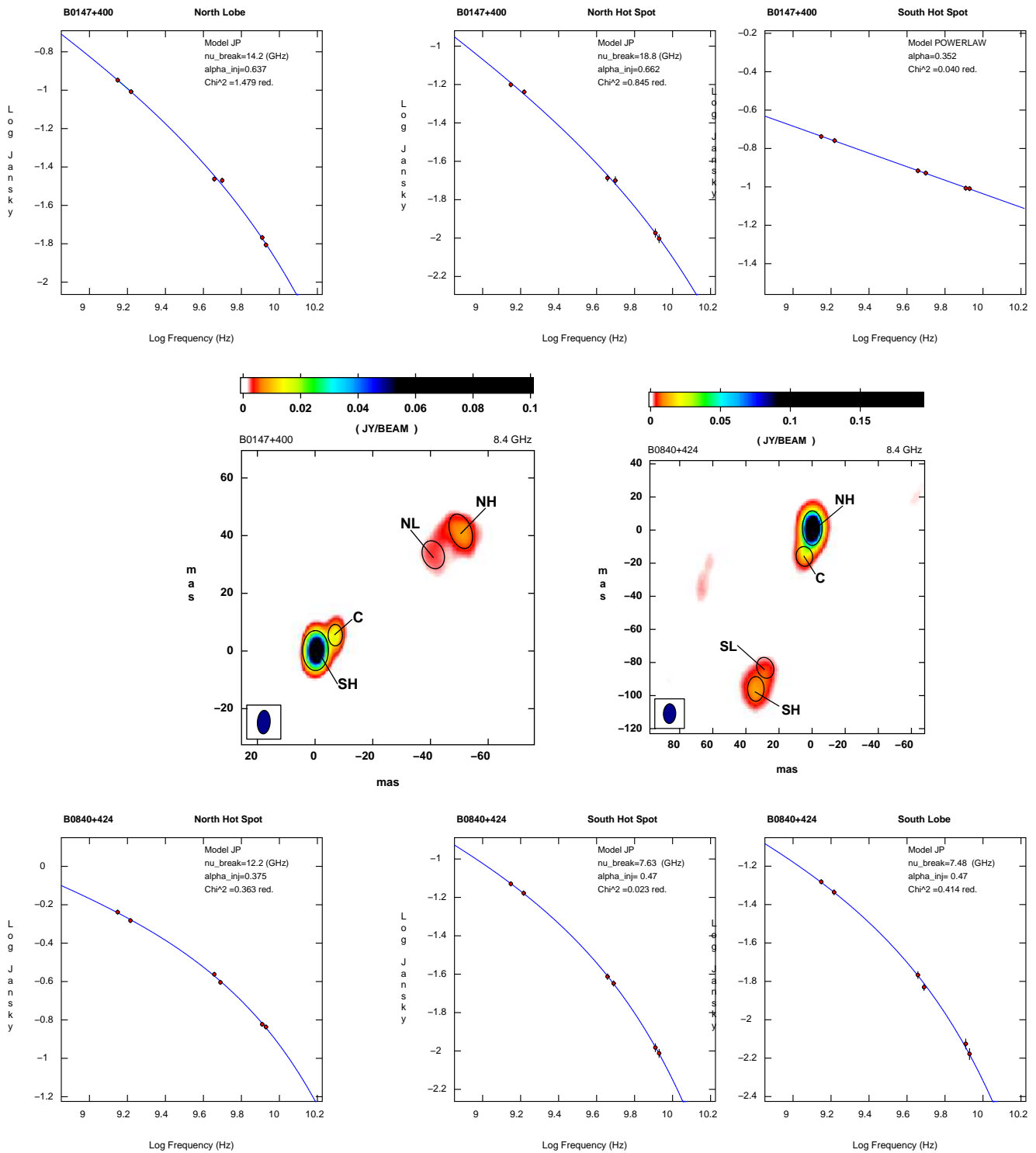


Figure 6.8: The spectral fits in the lobes and hot-spots of B0147+400 and B0840+424. On each fit we report the model, the injection spectral index, the break frequency and reduced-chi-squared. The *upper panel* shows, left to right, the local spectra in the Northern lobe (NL), Northern hot-spot (NH) and Southern hot-spot (SH) of the source B0147+400. The *bottom panel* shows, left to right, the local spectra in the Northern hot-spot (NH), Southern hot-spot (SH) and Southern lobe (SL) of the source B0840+424. The spectra of the core components are not shown, and they can be found in Orienti et al. (2004). The restoring beam (HPBW) is 8.20×4.46 mas in pa -3.59 and 1.198×0.753 in pa -1.94 for B0147+400 and B0848+424 respectively.

The hot-spots

The radio source B0147+400 displays two rather compact features that can be interpreted as hot-spots located ~ 9 mas South-East and ~ 55 mas North-West of the core, with a flux density ratio $S_{SE}/S_{NW} \sim 2.1$ and 5.2 in C and X bands respectively (Oriente et al. 2004).

The brightest hot-spot (labeled SH in Fig. 6.8) is embedded in the SE component and dominates the radio emission ($\sim 68\%$) in C and X bands (Table 6.3). It is best fitted by a power-law with an *injection* spectral index of $\alpha_{inj} \sim 0.40$. This implies that a continuous supply and re-acceleration of fresh particles occur, in agreement with what predicted by source growth models.

We point out that Fermi acceleration of particles produces $\alpha_{inj} \geq 0.5$. In order to match the observed value, synchrotron self-absorption together with acceleration mechanisms likely occur.

On the other hand, the faint hot-spot embedded in the NW component (labeled NH in Fig. 6.8) is well fitted by a higher injection spectral index of $\alpha_{inj} \sim 0.65$.

In the source B0840+424 the Northern and Southern components are ~ 15 and ~ 100 mas apart from the core, with a flux density ratio of $S_N/S_S \sim 6.0$ and 7.1 in C and X bands.

The brightest hot-spot (labeled NH in Fig. 6.8) is located at the centre of the Northern component. The hot-spot can only be fitted by a single-injection model but with an $\alpha_{inj} \sim 0.40$, which is similar to what is found in the brightest hot-spot of B0147+400. The single-injection model found in this hot-spot can be easily explained by considering a strong contamination by the lobe emission. The hot-spot embedded in the Southern component (labeled SH in Fig. 6.8) is not as bright and well-defined as the one in the Northern lobe, and it displays a higher $\alpha_{inj} \sim 0.50$.

In both sources, the faintest hot-spots have α_{inj} steeper than those found by a previous work from Oriente et al. (2004). However, that work, based on 3 independent frequencies only, provided good fits for a range of injection spectral indices. The availability of 6 independent spectral points in this study allows us to set tighter constraints on the fits and their parameters.

The lobes

The lobes represent the ideal loci where the radiative age can be computed with a high degree of accuracy. To estimate the source age, the variation of the break frequency across different regions of the lobes have been determined. To improve the reliability of the analysis, only those regions with a good signal-to-noise ratio at all frequencies have been considered. Indeed, at high frequency (i.e. X band), low surface brightness regions are almost completely resolved out, causing the fits to fail.

This effect is also caused by the spectral steepening itself due to synchrotron losses that make the oldest regions appear much fainter at higher frequencies.

Since the electrons in the lobe have likely received the last acceleration in the corresponding hot-spot, we fit their spectra with a single-injection model with the α_{inj} derived for the hot-spot.

The radiative age estimated in this way is the time elapsed since the electron population has left the hot-spot, or conversely the time elapsed since the hot-spot passage at that location during its outward motion.

Fits with both the JP and KP models have been used. The JP model assumes that the *pitch angle* θ_p between the electron velocity and the magnetic field direction is continuously re-isotropized, making the electrons age in the same way. In the KP model, the *pitch angles* of the electron populations are constant, making the electrons with different θ_p age in slightly different ways and timescales.

Although both models provide similar fits to our spectra, the fits with the JP model have smaller reduced χ^2 than the KP.

In B0147+400, the break frequency across the Northern lobe (labeled NL in Fig. 6.8) has been studied. Using the injection spectral index of $\alpha_{\text{inj}} = 0.65$ as derived from the northern hot-spot, the minimum break frequency is $\nu_{\text{br}} = 14$ GHz.

In the case of B0840+424, the spectra across the Southern lobe (labeled SL in Fig. 6.8) are fitted with α_{inj} of 0.50, which gives the lowest break frequency at 7.5 GHz. For both sources different regions across the lobe have been taken into account, and the final choice was made on the best compromise between the largest distance from the hot-spot and the need for significant emission at the highest frequencies.

In both sources the lobe related to the brightest hot-spot is almost completely resolved out and no spectral analysis could be provided.

The cores

In both B0147+400 and B0840+424 the core, labeled C in Figs. 6.7 and 6.8 has been definitely identified by means of the inverted spectrum displayed ($\alpha_{4.5}^{8.4} \sim -0.5$ and -0.03 for B0147+400 and B0840+424 respectively; Table 6.3).

These compact components are better visible in the full resolution images at the highest observing frequency.

In both cases, in the X band they account for almost 10% of the total flux density of the whole source.

Neither core shows any significant flux density variability in the X band between these new data and those presented by Orienti et al. (2004).

Linearly Polarized Emission

Images in the Stokes' U and Q parameters have been derived for both the target sources, as well as for the calibration objects in C and X bands. Calibration sources proved to have integrated VLBA polarized emission in agreement with VLA measurements carried out at a very close epoch, as available from the VLA/VLBA polarization calibration database.

No significant ($\geq 3\sigma$ noise level) polarized emission was detected for the target sources in both C and X bands, consistent with previous VLA (Fanti et al. 2001) and VLBA observations (Orienti et al. 2004) at the same frequencies.

The local upper limits are of 0.03% and 0.14% for the Southern and Northern components of B0147+400 respectively, and of 0.01% and 0.08% for the Northern and Southern components of B0840+424.

These results are in good agreement with those found by Fanti et al. (2004). Indeed, although the redshift of both sources is unknown, their projected linear sizes can be estimated to be ≤ 520 and 900 pc for B0147+400 and B0840+424 respectively (Table 6.4). Following the work of Fanti et al. (2004), both sources fall in the interval of unpolarized CSS sources even in the X band, suggesting that the source size is not large enough to lead the radio emission to emerge out of the "Faraday Screen".

Source	z	LLS pc	B_{eq} mG	t_{syn} 10^3yr	LS pc	Dist_{fhs} pc	v_{fhs} c	Age 10^3yr	Dist_{bhs} pc	v_{bhs} c
(1)	(2)	(3)	(4)	(5)	(6)	(7)	(8)	(9)	(10)	(11)
B0147+400	0.20	210	3.0	2.6	64	188	0.08	7.5	29	0.01
	0.35	316	3.0	2.6	97	258	0.13	7.5	44	0.02
	0.40	344	3.0	2.6	106	307	0.13	7.5	48	0.02
	0.60	429	3.3	2.2	132	383	0.19	6.5	60	0.03
	0.80	488	3.6	2.0	149	432	0.25	5.6	67	0.04
	1.00	518	4.0	1.7	159	462	0.31	4.8	72	0.05
B0840+424	0.20	362	1.2	14.0	64	301	0.015	70.0	49	0.002
	0.35	544	1.6	9.4	97	452	0.034	44.0	73	0.005
	0.40	592	1.6	9.1	106	492	0.038	42.0	79	0.006
	0.60	740	1.7	8.3	132	614	0.052	38.0	100	0.009
	0.80	834	1.9	7.0	149	692	0.069	32.5	112	0.011
	1.00	892	2.1	6.0	159	740	0.086	28.0	120	0.014

Table 6.4: Source ages. Column 1: source name; Column 2: redshift; Column 3: the total linear size; Column 4: the equipartition magnetic field, computed assuming the source parameters from Orienti et al. (2004); Column 5: the radiative age, computed using equation 6.2 and the lowest break frequency as described in § 6.4.2; Column 6: the projected linear size, in pc, between the region considered to derive radiative age and the location of the corresponding hot-spot; Column 7: the projected distance, in pc, between the core component and the faintest hot-spot; Column 8: the mean advance speed of the faintest hot-spot; Column 9: the source age; Column 10: the projected distance between the core and the brightest hot-spot; Column 11: the mean advance speed of the brightest hot-spot.

6.4.4 The radiative age

Equation 6.2 shows that the synchrotron age is strictly related to the break frequency ν_{br} , which can be derived from the fits to the observed radio spectrum, and the magnetic field B . Direct measurements of the magnetic field are very difficult, often impossible to carry out. Ideally, it can be measured from the turnover frequency and component sizes, if both are known, but the uncertainties remain quite large. Alternatively, we can measure it by comparing the synchrotron and inverse Compton losses, but X-ray observations of small and young radio sources have not provided strong constraints so far, except a few cases like the one discussed in § 6.3.

In the following discussion, the magnetic field of the source components has been computed assuming minimum energy and equipartition conditions, and using standard formulae (Pacholczyk 1970). Furthermore, proton and electron energies have been assumed to be equal, with a filling factor of unity (i.e. the source volume is fully and homogeneously filled by relativistic plasma); an ellipsoidal geometry and an average optically thin spectral index of 0.7 have been adopted. The observational parameters involved in such a computation are reported in Table 6.3.

We also point out that the magnetic field of CSS sources (Table 6.4, Column 4) is at least two orders of magnitude stronger than that 'equivalent' to the Cosmic Microwave Background radiation photons:

$$\frac{H_{\text{CMB}}^2}{8\pi} = u_{\text{CMB}}(1+z)^4 \quad (6.3)$$

where $u_{\text{CMB}} = 0.26 \text{ eV/cm}^3$. Inverse Compton losses are therefore neglected, synchrotron being the main cooling mechanism.

Furthermore, even adiabatic losses are negligible, since the energy spent due to adiabatic expansion is three orders of magnitude smaller than the synchrotron losses. Unfortunately both sources lack spectroscopic redshifts. The source B0147+400 has no optical identification, while B0840+424 can be identified with a galaxy in the Sloan Digital Sky Survey (SDSS). The HyperZ code (Bolzonella et al. 2000) was used to infer the photometric redshift by means of the magnitudes provided by the SDSS for the source B0840+424. A photometric redshift of 0.35 was obtained with a probability of 83%.

Since most of the intrinsic physical parameters, such as the magnetic field (B_{eq}) and the linear size (LS), critically depend on redshift, for each source a set of values is provided, which considers a few cases in which z is in the range of 0.2 - 1.0 (Table 6.4). The radiative ages found in this way are in the range of 10^3 - 10^4 years. However, as previously mentioned, this should not be considered as the source age. Models of source evolution predict that relativistic electrons are deposited in the region of last acceleration, where they age, while the hot-spot continues its way through the interstellar medium. Therefore, the electrons considered for the previous computation have no memory of the original injection by the core, since they have already been re-accelerated by the hot-spot. The radiative ages derived give us an indication of the time elapsed since the last acceleration in the hot-spot.

Source	Component	$S_{8.4}$ mJy	θ_{maj} mas	θ_{min} mas	P_{min} dyne/cm ²
B0147+400	HS	119	3	2	3.4×10^{-6}
	HN	22	9	6	4.9×10^{-7}
B0840+424	HN	249	8	3	2.1×10^{-6}
	HS	26	13	8	1.4×10^{-7}

Table 6.5: The hot-spot pressure. Column 1: source name; Column 2: source component; Column 4: VLBA flux density at 8.4 GHz; Columns 5, 6: deconvolved angular size of the major and minor axis of the source component; Column 7: the minimum pressure, computed assuming the minimum energy condition, and an indicative redshift of 0.35.

By measuring the distance between the region considered for the radiative age and the hot-spot, we can estimate the hot-spot advance speed. In both sources, the hot-spot has covered a distance of ~ 20 mas from the region where we could measure the radiative age, implying a range of *mean* hot-spot velocities of 0.08c to 0.31c for B0147+400 and 0.038c and 0.086c for B0840+424, depending on the source redshift (Table 6.4). Since we know the distance between the hot-spot and the core component, assuming an average hot-spot velocity over the whole lifetime of the source (Polatidis & Conway 2003), we can constrain the true source age. In the case of B0147+400, the core-hot-spot separation is 53 mas, which leads to a source age of 4.8×10^3 and 7.5×10^3 years. For the source B0840+424, the distance between the core and the hot-spot is larger (97 mas), and we derive an age between 2.8×10^4 and 7.0×10^4 years (4.4×10^4 years, considering the photometric redshift 0.35).

We can also estimate the mean advance speed of the brightest hot-spot, dividing its distance from the core by the source age. We obtain velocities ranging from 0.01c and 0.05c for B0147+400 and 0.002c and 0.014c for B0840+424 (Table 6.4).

6.4.5 Influence of the ambient medium

From the analysis of the synchrotron spectra in the two CSOs B0147+400 and B0840+424 (Oriente et al. 2007c), the source radiative ages have been estimated about $\sim 5 \times 10^3$ and 5×10^4 years, in good agreement with kinematic and radiative

studies carried out on the same class of objects (Polatidis & Conway 2003; Murgia et al. 1999). The approach used to infer the source age, described in the previous Section, is based on the strong assumption that the hot-spot velocity derived is truly representative of the *mean individual hot-spot advance speed*. However, there are several mechanisms that could cause the *instantaneous* hot-spot velocity to vary, such as hydro-dynamically introduced internal pressure changes (Norman 1996), as well as an inhomogeneous external medium.

The large asymmetries both in arm-length ratio and brightness shown by B0147+400 and B0840+424 strongly suggest that at least one of the two aforementioned possibilities applies. Table 6.5 reports the hot-spot internal pressure computed assuming that the source components are in the minimum energy condition. Contrary to expectations in both sources the hot-spot with the highest pressure is also the slowest one, suggesting that the asymmetric morphology is more likely due to an inhomogeneous clumpy medium.

Using simple one-dimensional ram-pressure arguments, the hot-spot advance speed v is determined by the equilibrium between the internal pressure p_i and the ram-pressure of the external medium (Eq. 1.6):

$$p_i \propto n_{\text{ext}} m_p v^2$$

Since the total linear size of the sources is smaller than the core radius (<1 kpc), we assume a roughly constant external density.

If in equation 1.6 we consider the average hot-spot velocity (Table 6.4) and the minimum pressure (Table 6.5), computed at an indicative redshift of 0.35, for both sources we find that the brightest and closest hot-spot is likely digging its way through a quite dense medium ($n_{\text{ext}} \sim 5.7$ and 50.0 cm^{-3} for B0147+400 and B0840+424 respectively), similar to what expected in a cloud. On the other hand, the farthest hot-spot is likely moving through an inter-cloud medium ($n_{\text{ext}} \sim 0.02$ and 0.08 cm^{-3} for B0147+400 and B0840+424 respectively) where the external density is about 3 orders of magnitude smaller, consistent with the tenuous warm medium.

Such clouds, indicating the presence of a rich and clumpy interstellar medium interacting with a CSS/GPS radio source, have been found by means of high-resolution spectral studies of neutral hydrogen (Morganti et al. 2004; Labiano et al. 2006).

In the GPS ULIRG galaxy 4C 12.50, Morganti et al. (2004) detected a cloud with an HI mass of a few 10^5 to $10^6 M_{\odot}$ and $\sim 20 \times 66$ pc in size, corresponding to an average density of $\sim 2 \times 10^3 \text{ cm}^{-3}$.

Labiano et al. (2006) studied the HI in the two very asymmetric CSS sources 3C 49 and 3C 268.3, in which the brightest lobe is also the closest one to the core, as in our targets.

In both sources HI absorption was detected only against the brightest and closest (to the core) component. The absorber medium has been interpreted in terms of clouds which are in the environment of the CSS/GPS radio sources, with densities of $220/c_f$ ($0.04 < c_f < 1$, for 3C 49) and $360/c_f$ ($0.025 < c_f < 1$, for 3C 268.3), where c_f is the covering factor.

These values are in good agreement with the characteristics of the ISM in the Narrow-Line Region (NLR; Fanti et al. 1995), in which the hot-spots of the aforementioned sources actually reside.

Our results on B0147+400 and B0840+424 are consistent with a picture in which one side of the radio source is strongly interacting with a dense clump, while the other is expanding through an intercloud medium. The interaction with the cloud causes the lobe to slow down its propagation, and favours radio emission by means of compression and shocks (Jeyakumar et al. 2005; Bicknell et al. 2003), which increase the energy production efficiency. Furthermore, the ionized clouds can also act as a Faraday Screen, leading to the observed depolarization as found in both sources.

The detection of such asymmetric CSOs may be favoured by a selection effect. The interaction with a dense ambient medium may enhance the radio emission, making these objects more likely detectable in flux-limited samples. This is in agreement with other studies based on asymmetries in CSOs (Saikia et al. 2003), in which on such a small scale, the probability that the brightest lobe is also the closest one to the core is higher than in larger sources.

From this result, we infer that the knowledge of the properties of the ambient medium surrounding the radio source is of fundamental importance in order to draw a complete and reliable picture of the individual source evolution.

Chapter 7

What are High Frequency Peakers?

High Frequency Peaker radio sources are an extreme class of active galactic nuclei whose nature has not been well understood yet. These sources have simple convex radio spectra with turnover frequencies well above a few GHz (Dallacasa et al. 2000). They are intrinsically compact with linear sizes $\ll 1$ kpc and thus reside within the innermost region of the host galaxy.

In the framework of self-similar evolution models (e.g. Fanti et al. 1995; Snellen et al. 2000), these sources are interpreted to represent the earliest stage in the radio source evolution. However, not all the objects selected on the basis of their radio spectrum are genuine compact young radio sources. The population of blazar objects, although usually characterized by flat spectra, occasionally display a convex spectrum during a particular phase of their variability (i.e. when their radio emission is dominated by a knot in a jet).

As widely described in the previous chapters, for most of their lifetime these two radio source populations show very different radio properties. Blazars are variable and possibly large radio sources which appear small due to projection effects together with some amount of beaming which enhances the core region making the low-surface brightness emission hardly visible. Their radio emission mainly comes from the core and the jet base and thus they usually have a Core-Jet or a complex morphology and their radio emission is often substantially polarized.

On the other hand, as already pointed out by a conspicuous number of works (Fanti et al. 1990; O’Dea et al. 1991; Dallacasa et al. 1995; O’Dea 1998; Stanghellini et al. 2005) genuine young radio sources are the least variable class of compact

extragalactic objects. Their radio emission mainly originates from the radio lobes and it has a two-sided morphology. They are completely unpolarized or display very low amount of radio polarization at least at low frequencies.

Among the 55 sources from the “bright” HFP sample (Dallacasa et al. 2000), 25 ($\sim 45\%$) objects have these characteristics and can be considered young radio source candidates (Table 7.1), while 30 ($\sim 55\%$) match the characteristics of blazar objects (Oriente & Dallacasa 2007b, submitted).

The optical identification of HFPs is a mixture of galaxies, quasars and BL Lac objects. HFPs with different optical counterparts tend also to have different radio properties, suggesting two distinct radio source populations: the majority ($\sim 88\%$) of the HFPs identified with quasars have the typical characteristics shown by blazar objects, while all the galaxies display the properties of the class of young radio sources.

This suggests that HFP quasars are intrinsically similar to the flat-spectrum sources whose emission is related to the core components, while HFP galaxies are likely genuine young objects whose radio emission mainly originates from non-variable components (mini-lobes and hot-spots).

7.1 A connection between HFP and CSS/GPS sources?

The expected number of very young sources (~ 100 years old) can be determined from the ratio of their typical age and the average age of extended radio sources ($\sim 10^7$ years), once expansion velocity and luminosity have been assumed constant during the source lifetime.

This would imply a fraction of the order of 0.001%. In the case of the 87GB catalogue (Gregory et al. 1996), 1740 sources with 4.9-GHz flux-density > 300 mJy and $|b| < 10^\circ$ (the selection criteria used to define the “bright” HFP sample) would form a comparable “old” radio source population. Considering the 25 objects which are still young radio source candidates, an HFP/OLD $\sim 1\%$ is obtained, i.e. three orders of magnitude higher than what expected. Such a discrepancy requires more appropriate determination of the initial conditions.

To check whether HFPs are related to the class of GPS/CSS radio sources ($\sim 10^3$ - 10^5), other samples must be used. I consider the B3-VLA sample (Vigotti et al.

Source	ID	z	Morph.	V	m(%)	ν_p GHz
J0003+2129	G	0.452	CSO	3.32	0.6 _U	5.2
J0005+0524	Q	1.887	CSO	2.16	0.58 _X	3.5
J0037+1109	G		CSO	1.47	-	6.0
J0111+3906	G	0.668	CSO	4.63	-	6.0
J0428+3259	G	0.479	CSO	2.40	-	6.6
J0638+5933	EF		CSO	3.74	-	10.2
J0650+6001	Q	0.455	CSO	3.12	-	5.4
J0655+4100	G	0.02156	Un	3.73	n.i.	8.0
J0722+3722	Q	1.63	MR	4.76	n.i.	4.0
J1045+0624	Q	1.507	Un	5.75	n.i.	4.7
J1148+5254	Q	1.632	CSO	9.74	n.i.	7.9
J1335+4542	Q	2.449	CSO	4.64	n.i.	5.1
J1335+5844	EF		CSO	2.84	n.i.	6.0
J1407+2827	G	0.0769	CSO	2.84	n.i.	5.0
J1412+1334	EF		Un	0.97	-	4.3
J1430+1043	Q	1.710	MR	1.37	-	6.2
J1511+0518	G	0.084	CSO	10.24	-	10.1
J1526+6650	Q	3.02	MR	2.04	-	5.5
J1623+6624	G	0.203	Un	11.16	-	5.0
J1735+5049	G		CSO	2.07	-	5.6
J1800+3848	Q	2.092	Un	1.92	0.6 _K	13.0
J1850+2825	Q	2.56	Un	2.15	-	9.9
J1855+3742	G		CSO	1.32	-	4.0
J2203+1007	G		CSO	1.94	-	4.6
J2257+0243	Q	2.081	Un	3.27	-	14.0

Table 7.1: Summary of the main characteristics derived from the investigation of the morphology, variability and polarimetry of the sources which can still be considered candidate HFPs. Column 1: source name; Col. 2: optical identification; Col. 3: redshift; Col. 4: VLBA Morphology (MR=Marginally Resolved, Un=Unresolved, CSO=CSO-like; see § 4); Col. 5: the variability index (see § 3); Col. 6: the highest fractional polarization and the band where is detected (n.i.= no information available so far); Col. 7: the peak frequency.

1989) and its B3-VLA CSS sub-sample (Fanti et al. 2001; § 2). The B3-VLA comprises 1049 sources with RA between $23^h00'$ - $03^h00'$ and $07^h00'$ - $15^h00'$ and DEC between $37^\circ15'$ - $47^\circ37'$ (§ 2.1.4).

To make a reliable comparison among the B3-VLA samples and the “bright” HFP sample, only those young HFP candidates which reside in the same area of the B3-VLA are considered. Among the 25 HFPs candidates, only 6 are within the

area covered by B3-VLA. On the other hand, in the case of the B3-VLA only those sources with a 4.9-GHz flux-density > 300 mJy are selected. With this selection tool 107 objects have been selected: 21 out of them are part of the B3-VLA CSS sample, while the remaining 86 objects can be considered the “old” radio source population. From the comparison between the typical ages of the different radio source populations one would expect $\text{HFP/CSS} \sim 0.01$ and $\text{CSS/OLD} \sim 0.001$. In this case: $\text{HFP/CSS} \sim 0.3$, $\text{CSS/OLD} \sim 0.24$ and $\text{HFP/OLD} \sim 0.07$, which largely exceed the expected fractions.

In the case in which the radio luminosity (or the expansion velocity) is not constant during the lifetime of the radio source, but it decreases as the radio source grows (Baldwin 1982), it is possible to reproduce the number counts in a more appropriate way.

Furthermore, it has been recognized (Jeyakumar et al. 2005; Orienti et al. 2007c) that the characteristics of the ambient medium can strongly influence the radio source evolution, for example when a jet-cloud interaction takes place.

Such an interaction, although quite rare given the small fraction of the total volume occupied by the clumpy medium, has higher probability to take place when the jet is still expanding through the innermost part of the host galaxy (Alexander 2000), i.e. the radio emission is still in an early stage (HFP, GPS or CSS) of its evolution/growth. In this scenario the high number counts of young objects is likely the result of a selection effect: the interaction between a jet and a dense cloud temporarily enhances the synchrotron luminosity shifting the source at higher flux densities and then increasing the fraction of such objects in flux density limited catalogues.

To check this hypothesis, a sample of young HFP candidates (Table 7.1; Dallacasa et al. 2000), GPS (Stanghellini et al. 1998), CSS (Fanti et al. 2001) and the “old”, powerful extended classical Doubles (Laing et al. 1983) has been constructed. All the selected sources have a Double morphology (i.e. their radio emission is dominated by lobe and hot-spots) and are optically identified with galaxies in order to avoid orientation effects, according to the Unified Models of AGNs (Antonucci 1993).

For each source the flux-density ratio r_S between the two components (lobe+hot-spot) have been considered, while radio jets and core provide negligible contribution to the total radio emission.

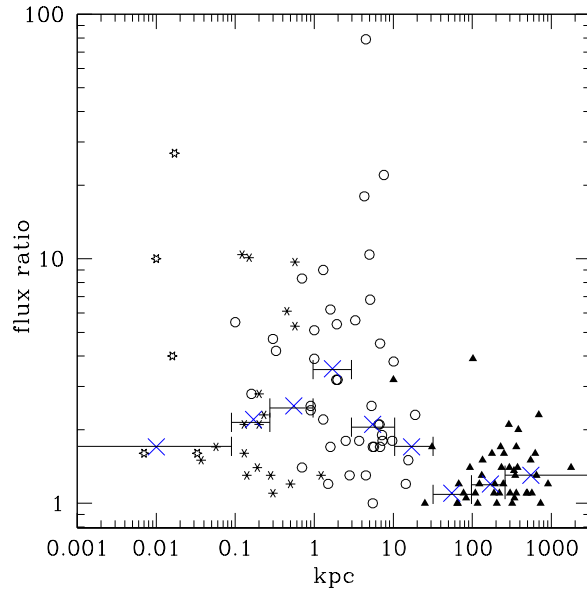


Figure 7.1: The flux-density ratio of the components versus the source linear size. Empty stars are HFPs from Dallacasa et al. (2000), asterisks GPSs from Stanghellini et al. (1998), empty circles CSSs from Fanti et al. (2001) and filled triangles “old” extended Doubles from Laing et al. (1983). Blue crosses represent the median values computed on various ranges of linear sizes. All objects are optically identified with galaxies and display a Double radio morphology.

If the two jets expand through an ambient medium with similar conditions a $r_S \sim 1$ is expected. On the other hand, r_S significantly different from unity is expected in the case of a jet-cloud interaction. In this case r_S strictly depends on the characteristics of the cloud (§ 7.2.2).

Fig. 7.1 plots the observed r_S against the linear size for the radio galaxies from the aforementioned sample. There is a clear segregation in the flux-density ratio between sources larger and smaller than ~ 15 kpc. The former have r_S which ranges from 1 to 3, while the latter have r_S spread over almost one order of magnitude with a few objects displaying very large ratios. This result is in agreement with the idea that the ISM is much denser and richer than the IGM.

7.2 Modeling the evolution of the radio emission

A complete picture relating the various steps in the radio source growth, from its birth to its oldest phase, is one of the biggest challenges in astrophysics.

In the early '70s Scheuer (1974) proposed the first model which relates the changes in the radio source properties as the radio emission evolves.

In the next decade Baldwin (1982) modified the seminal paper by Scheuer introducing the information on the ambient medium available at that time. Its main result was the discovery of a decrement of the radio luminosity as the source grows.

The discovery of the population of GPS/CSS young radio sources yielded to an improvement of the theories suggested to interpret the early stages in the radio source evolution.

So far different models (i.e. Fanti et al. 1995; Readhead et al. 1996; Snellen et al. 2000; Alexander 2000) based on the original idea of Baldwin (1982) have been developed. All these models take into account the characteristics of the environment, as derived from X-ray observations (e.g. Trinchieri et al. 1986), which naturally lead to a decrement in the radio luminosity as the radio source grows. As already discussed in previous sections, such a decrement is required to explain the high number counts of young radio sources with respect to the “old” large-size classical Doubles. However, when results predicted by the models are compared with the data, there are various aspects concerning the smallest and youngest objects which require some more work on the models developed so far.

Different works on CSS/GPS sources (i.e. Saikia et al. 2003; Fanti et al. 1990) remarked that a large number of objects display substantial asymmetries in both arm-length and flux-density ratio between the two lobes. Furthermore, on such a small scales the probability that the brightest lobe is also the closest one to the core is much higher than in larger sources, which is opposite to the expectations of the “standard” source model.

To reproduce the observed asymmetries Jeyakumar et al. (2005) proposed a model in which the two jets propagate through an ambient medium with different density profiles on the two sides.

However, in recent spectral-line observations of two very asymmetric CSS galaxies (3C 49 and 3C 268.3; Labiano et al. 2006) HI in absorption has been detected only

against the brightest and closest lobe. Such a result strongly indicates that, despite the small filling factor of the clumpy medium if compared to the total volume, a jet-cloud interaction can actually take place and reproduce the observed asymmetries.

In the following discussion I propose a new analytical model based on previous works, in which the radio emission evolves in a self-similar way through a two-phase medium which consists of both a clumpy and a smooth component filling the inter-cloud space.

7.2.1 A simple self-similar evolution model

The main ingredient at the basis of the radio source evolution is the balance between the jet power and the ram-pressure exerted by the surrounding medium on an expanding bubble in supersonic motion.

Following the approach from Kaiser & Alexander (1997) we assume a constant jet power P_j and a constant rate of rest-mass transported along the relativistic jet \dot{M} :

$$\dot{M} = \frac{P_j}{(\gamma_j - 1)c^2} \quad (7.1)$$

Given their small sizes, young radio sources entirely reside within the Interstellar Medium of the host galaxy, whose density is described by a King profile (Eq. 1.8):

$$n_{ext} \propto n_0 \left(1 + \frac{r^2}{r_0^2} \right)^{-\frac{\beta}{2}}$$

where n_0 is the average density within the core radius r_0 , i.e. the Narrow-Line Region (≤ 1 kpc), as suggested by X-ray observations of early-type galaxies (Trinchieri et al. 1986). We then approximate with a constant density $n_{ext} \sim n_0$ up to r_0 (i.e. $\beta=0$) and with $n_{ext} \propto r^{-\beta}$ beyond r_0 . No cosmological evolution of the characteristics of the host galaxy population has been considered, in agreement with the currently available data (Tinti et al. 2006; Snellen et al. 2000).

Given the above assumptions, for $r \leq r_0$, the characteristic quantities P_j , \dot{M} and n_0 lead us to define a characteristic length scale:

$$R_0 = \left(\frac{n_0^2 P_j}{\dot{M}^3} \right)^{-\frac{1}{4}} \quad (7.2)$$

and a corresponding time scale:

$$t_0 = R_0^{\frac{5}{3}} \left(\frac{n_0}{P_j} \right)^{\frac{1}{3}} \quad (7.3)$$

For a typical galaxy environment with $n_0 \sim 0.1 \text{ cm}^{-3}$, a jet power $P_j \sim 10^{44} \text{ erg/s}$ (Fanti et al. 1995) and $\gamma_j \sim 2$ (Kaiser & Alexander 1997), we find $R_0 \sim 1 \text{ pc}$ and $t_0 \sim 5 \text{ yr}$. Sources with linear size (and lifetime) larger than R_0 (t_0) are growing in a self-similar way (Falle 1991), and R_0 (t_0) can be considered as the initial condition of the self-similar evolution model.

If the thrust of each relativistic jet is balanced by the ram-pressure of the surrounding medium we have:

$$v \propto \left(\frac{P_j}{n_{ext} c A} \right)^{\frac{1}{2}} \quad (7.4)$$

where v is the hot-spot advance speed, A the cross-section area and c the speed of light. The energy density u of the radio source is:

$$u \propto \left(\frac{P_j t}{V} \right) \quad (7.5)$$

where V is the volume of the radio source and t the time elapsed since the characteristic time t_0 . Assuming equipartition conditions, the luminosity L of the radio source is:

$$L \propto \left(\frac{P_j t}{V^{\frac{3}{7}}} \right)^{\frac{7}{4}} \quad (7.6)$$

We consider the two regimes $r < r_0$ and $r > r_0$ separately.

If the radio emission grows in a self-similar way as suggested by theoretical works (Kaiser & Alexander 1997; Carvalho & O’Dea 2002) and observations (Jeyakumar et al. 2000), we find that in both regimes $A \propto v^2 t^2$ and $V \propto v^3 t^3$.

1) $r < r_0$: the radio emission is within the core radius. In this case:

$$v \propto t^{-\frac{1}{2}} \quad (7.7)$$

$$L \propto t^{\frac{5}{8}} \quad (7.8)$$

the advance speed of the radio emission decreases with time, while the luminosity increases. Such results reproduce the same trend found by other self-similar evolution models (i.e. Fanti et al. 1995; Snellen et al. 2000) but with different dependences. Fanti et al. (2003) pointed out that the strong deceleration expected by these models is inconsistent with the observations and different assumptions on the ambient medium should be taken into account.

2) $r > r_0$: the radio source size exceeds the core radius:

$$v \propto t^{-\frac{2-\beta}{4-\beta}} \quad (7.9)$$

$$L \propto t^{-\frac{2+\beta}{16-4\beta}} \quad (7.10)$$

From X-ray observations of nearby ellipticals like the host of young radio sources, β is estimated to be ~ 2.0 . In this case the growth velocity becomes constant with time and the luminosity decreases as $L \propto t^{-\frac{1}{2}}$.

Both results are in agreement with the data available. As already mentioned, the decreasing luminosity is required from the number counts of young radio sources with respect to the largest ones. On the other hand, from spectral studies of the extended classical radio source population (Fanti et al. 1995), it seems that the propagation velocity does not exhibit any significant dependence with the overall linear size of the source, and therefore with the age.

7.2.2 The source growth in a clumpy medium

During its earliest stages the radio emission is expanding within the innermost part of the host galaxy: the Narrow-Line Region. In this region the environment is characterized by both a clumpy component with temperature $T \sim 10^4$ K and high density $n_e \sim 10^4 \text{ cm}^{-3}$, but small filling factors $\phi < 10^{-4}$ (Forbes et al. 1990); and a diffuse component, less dense $n_e \sim 10^{-3} \text{ cm}^{-3}$ and hotter (Forman et al. 1985) which fills the inter-cloud space. Despite of the small filling factor of the clumpy component of the gas, in some sources (i.e. the GPS 4C12.50, Morganti et al. 2004; the CSS galaxies 3C49 and 3C286.3, Labiano et al. 2006) there are strong indications of jet-cloud interaction. In the two CSS galaxies 3C49 and 3C286.3 HI has been revealed only against the brightest (and closest to the core) lobe. The radio

lobes with the HI absorption are preferentially associated with optical emission line gas, suggesting that the HI is located in the atomic cores of the clouds (Labiano et al. 2006).

This result indicates that the asymmetries in the flux-density and arm-length ratio could be explained in terms of interactions between the radio emission and a clumpy medium, rather than multi-phase media with different density profiles.

The probability that a jet-cloud interaction occurs is higher within the dense and rich medium of the NLR, rather than in the outer regions of the ISM.

When a jet interacts with a cloud its propagation is substantially slowed down, since the external density increases making the ram-pressure stronger. This means that when the jet impacts a cloud, its propagation velocity becomes:

$$\bar{v}_{jc} \propto v \left(\frac{n_0}{\bar{n}_{cl}} \right)^{\frac{1}{2}} \quad (7.11)$$

where \bar{v}_{jc} is the mean velocity of the jet when is piercing a cloud with mean density \bar{n}_{cl} and v is the velocity in the smooth plasma with constant density n_0 .

The same happens to the hot-spot luminosity:

$$L_{jc} \propto \bar{n}_{cl}^{\frac{9}{16}} t^{-\frac{1}{2}} \quad (7.12)$$

In this model n_{cl} is not constant through the cloud: the outer regions are likely to be of ionized plasma, while in the innermost region may reside a denser atomic core (Labiano et al. 2006). This scenario implies a decrement of the propagation velocity and an abrupt increment of the luminosity when the jet impacts the cloud.

As soon as the radio emission emerges from the denser clump, its velocity increases of a factor $(\bar{n}_{cl}/n_0)^{1/2}$, becoming again the same the jet had before the interaction took place. On the other hand, the luminosity abruptly decreases.

It is worth noting that a jet-cloud interaction can induce instabilities within the jet and hence its disruption.

The maximum stable length (Alexander 2000) is:

$$\frac{R_{\max}}{2.5\text{kpc}} \sim \left(\frac{P_j}{10^{44}\text{erg/s}} \right)^{1/2} \left(\frac{\bar{n}_{cl}}{0.1\text{cm}^{-3}} \right)^{-1/2} \quad (7.13)$$

and Fig. 7.2 plots the limit conditions which preserve the jet stability.

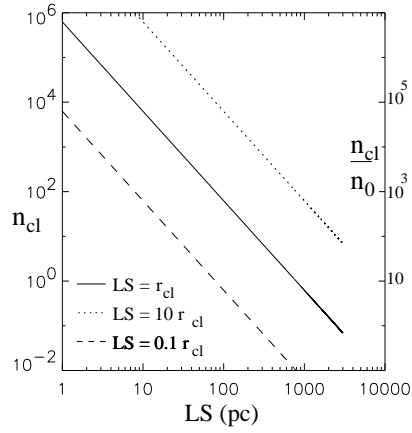


Figure 7.2: Jet linear size LS versus the density n_{cl} of a cloud with radius r_{cl} . The lines represent the limiting cases in which a jet remains stable: values of n_{cl} above such limits creates instabilities which causes the disruption of the jet itself.

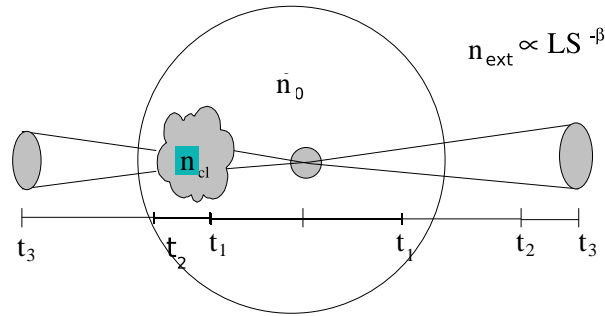


Figure 7.3: A cartoon of a possible radio source growth in a two-phase plasma, where one of the jets interacts with a cloud while the other one continues its way through a smooth medium with a King density profile. The size of both the NLR and denser clump, as well as its location are not known.

In the scenario of a stable jet, we want to understand how long the jet-cloud interaction can last and hence which range of asymmetries can build up.

Initial conditions are assumed as from § 7.2.1 ($\gamma \sim 2$, $R_0 \sim 1$ pc, $t_0 \sim 5$ yr, P_j and \dot{M} constant) and the two jets are expanding with the same physical properties through a medium with a King-like profile with $r_0 \sim 0.5$ kpc (Fig. 7.3).

Different snapshots of the radio source growth are considered. After ~ 500 years of unperturbed expansion one of the jets hits a denser clump with a diameter of ~ 10

pc and a density ~ 1000 times higher than that of the diffuse medium. During this period of unperturbed expansion each jet has covered a distance of ~ 70 pc.

Although clouds located in the NLR should have smaller linear size, a diameter of ~ 10 pc has been considered in order to pinpoint the maximum effect on the asymmetries.

Phase 1: Both jets propagate through a symmetric medium.

Both jets grow with the same physical characteristics within a symmetric medium with a constant density. For $t_0 < 500$ years, both jets have the same velocity and luminosity:

$$v_{jA,0} = v_{jB,0}$$

$$l_{jA,0} = l_{jB,0}.$$

Phase 2: Jet-cloud interaction

At $t_1 = 500$ years both jets are still propagating with a velocity:

$$v_{jA,1} = v_{jB,1} \sim 0.10c.$$

and the hot-spots are located at about 70 pc far from the core.

Then, Jet A impacts with a cloud of linear size $LS_{cl} \sim 10$ pc and $n_{cl}/n_0 \sim 1000$.

From Eq. 7.11 the velocity of Jet A instantaneously becomes:

$$v_{jA,2} \propto v_{jA,1}(n_0/n_{cl})^{1/2} \sim 0.003c.$$

Assuming that Jet A keeps a roughly constant velocity during its path through the cloud (Mellema et al. 2002), it takes 1.1×10^4 years to emerge from the clump.

As jet A impacts the cloud, its luminosity has an abrupt increment:

$$l_{jA,2} \sim l_{jA,1}((n_{cl}/n_0)^{9/8}).$$

followed by a smoother decline with time (Eq. 7.12; Fig. 7.4 dotted line).

In the meantime, Jet B is expanding through the diluted component of the NLR.

It takes ~ 3000 more years to reach the edge of the NLR, where it gets a velocity $v_{jB,2} \sim 0.038c$ (Eq. 7.7) and a luminosity $l_{jB,2} \sim 75 \times L_0$ (Eq. 7.8), where L_0 is the luminosity at the characteristic time t_0 .

Out from the NLR the ambient properties allow the jet propagation velocity to become constant and the instantaneous luminosity starts decreasing as $t^{-1/2}$ (Eq. 7.10).

At $t_2 = 1.1 \times 10^4$ years, Jet A emerges from the cloud, reaching a linear size of ~ 80 pc.

At the same time Jet B has grown ~ 600 pc, leading to an arm-length ratio:

$$r_{jB,2}/r_{jA,2} \sim 7.5.$$

while the luminosity ratio is $l_{jA,2}/l_{jB,2} \sim 70$.

If in this picture synchrotron losses are included, a higher decrement of the instantaneous luminosity with respect to those from Eq. 7.12 is expected. If the magnetic field B is frozen in the plasma, its value decreases as the source expands. Given the higher ram-pressure exerted by the dense clump than that due to the smooth medium, Jet A grows more slowly than Jet B. The slower expansion rate of Jet A is reflected in a slower decrement of its magnetic field, and therefore higher synchrotron losses with respect to Jet B. Such a condition makes the instantaneous flux-density (luminosity) ratio between A and B smaller than those predicted if synchrotron losses are not taken into account.

Phase 3: Both jets grow through the inter-cloud medium.

For $t > t_3$ both jets are traveling through the inter-cloud medium. As Jet A has emerged from the cloud and reached the intercloud medium with density n_0 its velocity becomes the same it had before the interaction, and it is higher than the velocity of jet B. For the next 3000 years its expansion through the NLR causes a decrement in velocity (Eq. 7.7), and a progressive decline of the arm-length ratio. On the other hand, the increment of the luminosity (Eq. 7.8) increases the flux-density ratio.

When eventually Jet A reaches the edge of the NLR $v_{jA} = v_{jB}$ and the arm-length ratio approaches unity more slowly. The luminosity starts decreasing (Eq. 7.10) leading the flux-density ratio to progressively approach ~ 1 .

In this example a particular configuration for the cloud (i.e. distance, density and linear size) has been assumed.

Fig. 7.4 plots various normalized instantaneous luminosity profiles concerning jet-cloud interaction with different characteristics. The dotted and dashed lines represent various jet-cloud interactions where $n_{cl}/n_0 = 1000$ occurring 10, 100, 500 and 1000 years after the characteristic time t_0 .

In a scenario of jet-cloud interactions only those clouds with linear sizes less than the linear size of the jet must be considered, in order to preserve the stability of the jet (Eq. 7.13, Fig. 7.2).

The continuum line describes the case in which no jet-cloud interaction takes place (i.e. unperturbed jet).

From Fig. 7.4 it is clear that interactions occurring at different times produce asymmetries which last for different periods of time. If the jet impacts a cloud at the very beginning (i.e. 10 years after the characteristic time t_0) when its propagation velocity has not decreased very much, the asymmetry can be almost totally recovered with time. On the other hand, if the interaction happens after a few hundred years, the flux-density ratio is not completely compensated when the jet emerges from the NLR.

Even the cloud size (and/or density) play a major role on the asymmetries: the smaller the LS_{cl} (and/or n_{cl}), the smaller the flux-density ratio is.

Furthermore, in this analytic model the jet-cloud interaction has been described with a density discontinuity. However, it is relevant to note that any realistic situation would have a steep gradient, with a density profile which likely increases moving toward the central region of the cloud. In this way the increment in luminosity taking place when the jet hits the cloud is not as abrupt as in Fig. 7.4, but it rather occurs in a smoother way.

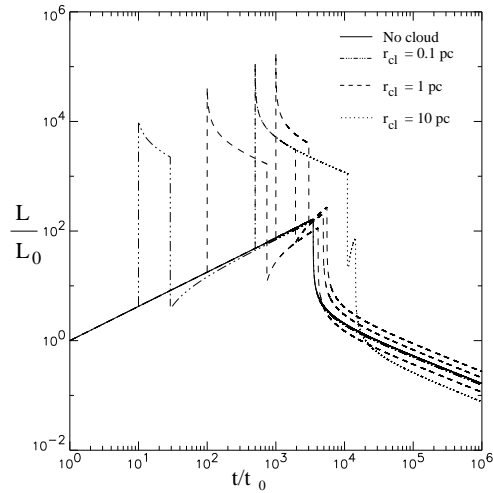


Figure 7.4: Log-log plot of the normalized instantaneous luminosity versus time produced by jet-cloud interactions. The continuum line represent the case where no interaction takes place and the jet is freely expanding through the inter-cloud medium. The abrupt luminosity increment obtained when the jet hits the cloud is produced by the density discontinuity assumed in this model.

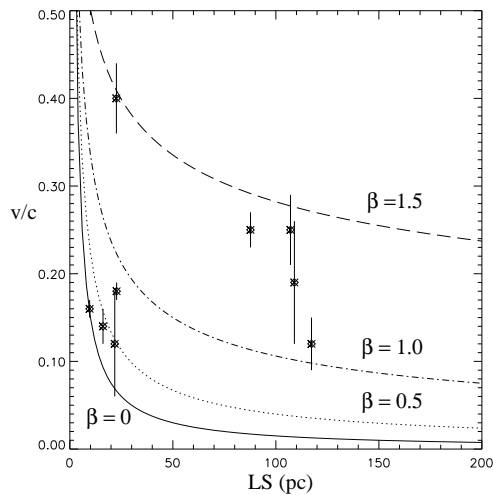


Figure 7.5: Different “double- β ” models are plotted together with measurements of hot-spot advance speed of CSOs from Polatidis & Conway (2003). Models have been computed assuming the initial condition as from § 7.2.1 ($\gamma \sim 2$, $R_0 \sim 1$ pc, P_j and \dot{M} constant).

7.2.3 Model versus observations: a double King-profile?

The model presented in the previous sections is based on the strong assumption that the ISM of the host galaxy has a double King-profile:

$$n = \sqrt{n_{\text{NLR}}(1 + (r/r_0)^2)^{-\frac{\beta_{\text{NLR}}}{2}} + n_{\text{ISM}}(1 + (r/r_1)^2)^{-\frac{\beta_{\text{ISM}}}{2}}} \quad (7.14)$$

where $\beta_{\text{NLR}} = 0$ within the NLR, and $\beta_{\text{ISM}} \sim 2.0$ beyond r_1 which is the radius of the NLR.

To check whether the model is in agreement with the observations the velocity trend expected from the model has been compared with the measurements of the hot-spot advance speeds currently available (Polatidis & Conway 2003). Fig. 7.5 reports the propagation velocity versus the source linear size ($\text{LS} = 2r_j$) assuming a double King-profile, where $\beta_{\text{NLR}} < 2$ for $r < r_{\text{NLR}}$ and $\beta_{\text{ISM}} \sim 2.0$ for $r > r_{\text{NLR}}$, and the measurements of the hot-spot advance speeds available (empty diamonds). A part in one case, the velocity trend predicted in the case of a NLR with a constant density ($\beta_{\text{NLR}} = 0$ solid line) is a few factors below the data.

Such a discrepancy is retrieved when $\beta_{\text{NLR}} > 0$ is assumed, in agreement with recent *Chandra* observations of nearby early-type galaxies (i.e. Humphrey et al. 2006), which point out a decreasing (and not constant) density in the inner regions.

We stress that all the changes due to a “double β -model” concern only the NLR. The ISM beyond the NLR is still fitted with $\beta_{\text{ISM}} \sim 2.0$, in agreement with the X-ray observations.

The different β -models used to fit the data within the NLR can set strong constraints on n_{NLR} and r_{NLR} . Recent X-ray observations (Vink et al. 2006) have shown that in young radio sources not only the radio emission has just switched on, but also the central engine has just started to ionize its surroundings. The optical narrow-line regions are found to be significantly underluminous (and show a trend with the source age), indicating that the NLR is still growing/settling down (Vink et al. 2006). Different propagation velocity can be reproduced by either different β_{NLR} or same β_{NLR} but different r_{NLR} , providing us important information on the physical condition of the NLR.

In a “double β ”-model both the propagation velocity and luminosity are not described by Eqs. 7.7 and 7.8 anymore, but they follow the trends reported in Table 7.6.

β	v	L
0	$t^{-1/2} LS^{-1}$	$t^{5/8}$
0.5	$t^{-3/7} LS^{-3/4}$	$t^{-5/28}$
1.0	$t^{-1/3} LS^{-1/2}$	$t^{-1/4}$
1.5	$t^{-1/5} LS^{-1/4}$	$t^{-7/20}$
2.0	constant	$t^{-1/2}$

Table 7.2: The evolution of the propagation velocity and luminosity within the NLR with different β_{NLR} .

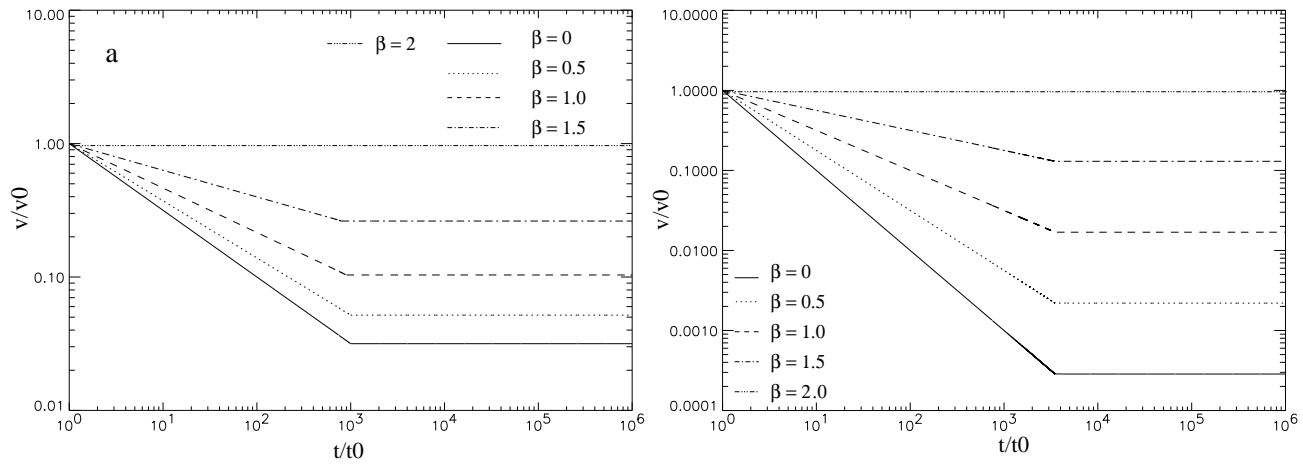


Figure 7.6: Log-log plot of the normalized instantaneous velocity versus time (*left panel*) and versus linear size (*right panel*). The NLR has been modeled with various King-profiles with $\beta_{\text{NLR}} \leq 1.5$, while the ISM is assumed with $\beta_{\text{ISM}} \sim 2.0$ in all the “double β ”-models.

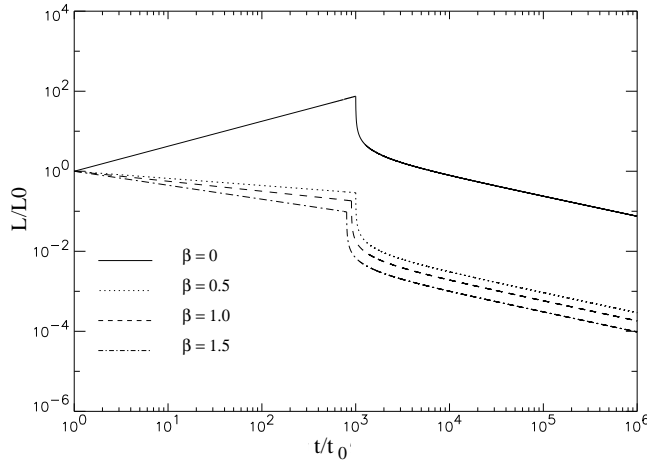


Figure 7.7: Log-log plot of the normalized instantaneous luminosity versus time. The NLR has been modeled with various King-profiles with $\beta \leq 1.5$, while the ISM is assumed with $\beta_{\text{ISM}} \sim 2.0$ in all the “double β ”-models.

The propagation velocity has a decrement within the NLR (Fig. 7.6), which is smoother than the previous case, and consequently better agrees with the data.

On the other hand, the luminosity does not increase as in the case of a constant density ($\beta_{\text{NLR}}=0$; Eq. 7.8), but it has a slight decrement depending on β_{NLR} (Fig. 7.7). This result is in good agreement with the number counts of different class of young radio sources. The number counts of HFPs with respect to CSSs (§ 7.1) is ~ 30 times higher than what expected from the ratio between their ages, assuming a constant luminosity. This discrepancy is even more critical if an increasing luminosity within the NLR is assumed. A model where a luminosity decrement takes place also when the radio emission is still embedded within the NLR is a better compromise between data and model predictions.

Conclusions

Flux density limited catalogues are well known to possess a significant fraction ($\sim 10\%$ - 30%) of intrinsically compact extragalactic radio sources with a convex synchrotron radio spectrum: the Compact Steep-Spectrum (CSS) and GHz-Peaked Spectrum (GPS) objects. Their discriminant characteristics (compact sizes, turnover frequencies between ~ 100 MHz to a few GHz, and powerful radio emission) have been deeply investigated in order to understand the nature of this class of objects.

Such an amount of work has led to the conclusion that these objects are young radio sources with ages $\sim 10^3$ - 10^5 years, and represent an early-stage in the individual radio source evolution.

The empirical anti-correlation found between the peak frequency and the linear sizes tells us that the newly born radio sources (with ages of about a few hundred years or even less) must be sought out among those objects with the highest turnover frequency (higher than a few GHz), termed High Frequency Peakers (HFP).

Since recently, the low-selection frequency of the surveys available has precluded the selection of a statistically complete sample of such an *extremely* young population.

During this work the analysis of the only one (to date) statistically complete sample of 55 candidate HFPs has been carried out.

For the selection tools are based on the characteristics of the radio spectra at high frequency, it is possible that the sample comprises also a significant fraction of contaminant objects. Indeed, flat-spectrum blazar objects can temporarily display a convex spectrum during a particular phase of their characteristic variability.

However, for the majority of their lifetime genuine young radio sources and blazars have very different characteristics.

Blazar objects have:

- significant flux-density and spectral-shape variability;
- Core-Jet morphologies;
- significant amount of linearly (and circularly) polarized radio emission.

On the other hand, genuine young radio sources have:

- neither flux-density nor spectral-shape variability;
- a Double/Triple morphology;
- almost unpolarized radio emission.

In order to discriminate genuine HFPs from contaminant blazars I have studied in detail:

- the variability properties of each source by means of a multi-epoch monitoring campaign of multi-frequency VLA observations;
- the pc-scale morphologies by means of high-resolution multi-frequency VLBA observations;
- the linear polarization characteristics with multi-frequency high-sensitivity VLA observations.

I found that:

- the majority of the sources with significant flux-density and spectral variability also show high degree of linearly polarized emission.
- All the sources with a Core-Jet structure have significant variability and usually a flat spectrum.
- Almost all the unpolarized sources do not even display any kind of variability.
- All the sources with a Double/Triple morphology have neither variability nor polarized emission.

If all these pieces of evidence are compared together we find that of the originally 55 sources of the sample, only 25 (40%) can still be considered candidates to be

genuine young radio sources, indicating a very strong contamination of blazars.

The selection of a statistically complete sample of extremely young radio sources only is of fundamental importance in order to investigate the characteristics of the Interstellar Medium of the host galaxy, and then to understand the role played by the environment on the radio source evolution.

The kinematic and physical properties of the ISM have been investigated by means of WSRT observations searching for both HI in absorption in 6 genuine HFP galaxies, and OH-1720 MHz maser line in 7 genuine HFPs. These two sub-samples have been selected on the basis of the redshifted frequency which must fall within the receivers available at the telescope and in a region free from known RFI.

From the analysis of the data I found that only two of the six observed sources show HI absorption in their spectra, although with very different characteristics: one displays a very large optical depth (~ 0.44), likely due to a disk/torus structure, while the other shows a broad (~ 1800 km/s) blue-shifted and shallow (~ 0.005) HI absorption, interpreted in terms of fast-outflows of neutral gas.

In all the 7 sources observed searching for OH-1720 maser line, no detection of such a line has been found.

The main role played by the ambient medium on the evolution of the radio sources has been investigated by means of multi-frequency high-resolution VLBA observations of two very asymmetric CSOs. The observations have shown that contrary to what expected from beaming effects and path delay, the brightest component with the highest internal pressure (if minimum energy condition is assumed) is also the closest one to the core. This is easily explained by an inhomogeneous environment rather than a change in the hot-spot internal pressure. The densities of the media surrounding the two source components inferred from the data suggests that the brightest and closest (to the core) component is likely interacting with a denser clump, which slows the jet propagation velocity and enhances the radio emission, while the faintest and farthest component is expanding through a less dense intercloud medium.

This result must be kept in mind in order to draw a complete and reliable picture

of the individual source evolution.

If we consider self-similar evolution model in which both jets are propagating through a smooth medium whose density has a King profile, we cannot reproduce all the observed aspects.

For example, the assumption of an environment with a King profile naturally produces the decrement in luminosity necessary to reproduce the higher number counts of young radio sources with respect to the classical and old Doubles, but it completely fails when we want to reproduce some kind of arm-length and flux-density asymmetries.

In order to better reproduce the observational data, I have developed a self-similar evolution model which takes into account a two-phase medium consisting of both a clumpy medium and a smooth plasma with a King profile filling the inter-clump space.

This model predicts an increasing luminosity and a decreasing velocity with time, when the radio emission is still confined within the NLR. Such results, although similar to those obtained by other models, have problems to reproduce the observations. A better compromise is reached when also the environment in the NLR has not a constant density, but it also follows a King profile with a slope less steep than that of the outer ISM, as suggested by new X-ray observations. In this case the velocity is still decreasing, but more slowly, and it is able to reproduce quite well the observed measurements of the hot-spot advance speeds available so far. On the other hand, the luminosity is already decreasing even in the NLR, better explaining the higher fractions of HFPs with respect to CSS/GPS, which was completely in disagreement with a scenario of an increasing luminosity.

As the radio jets emerge from the NLR reaching the outer regions of the ISM, the velocity predicted by the model becomes constant, in agreement with observed velocity of large doubles, and the luminosity decreases, as required to explain the higher number counts of young sources. If we introduce the clumpy medium, we are able to reproduce different arm-length and flux-density asymmetries assuming clouds with several characteristics, such as linear size, density and location with respect to the origin of the radio emission.

Although evolution models can reproduce several phase of the radio source growth,

our knowledge on the mechanism at the origin of the onset of the radio emission, as well as its duration, is still not well understood. Future work carried out to describe and compare the physical condition of the ISM of the host galaxy of different radio source populations (HFPs, GPSs, CSSs and classical doubles) may give some more clues in order to eventually answer at these opening questions.

Bibliography

- Alexander, P. 2000, MNRAS, 319, 8
- Antonucci, R. 1993, ARA&A, 31, 473
- Baan, W.A. 1985, Nature, 315, 26
- Baldwin, J.E. 1982, IAUS, 97, 21
- Baum, S.A., O'Dea, C.P., de Bruyn, A.G. et al. 1990, A&A, 232, 19
- Begelman, M.C., Cioffi, D.F. 1989, ApJ, 345, 21
- Bicknell, G.V., Dopita, M.A., O'Dea, C.P. 1997, ApJ, 485, 112
- Bicknell, G.V., Saxton, C.J., Sutherland, R.S. 2003, PASA, 20, 102
- Bolzonella, M., Miralles, J.-M., Pellò, R. 2000, A&A, 363, 476
- Brogan, C.L., Zauderer, B.A., Lazio, T.J. et al. 2005, AJ, 130, 698
- Browne, I.W.A., Patnaik, A.R., Wilkinson, P.N., Wrobel, J.A. 1998 MNRAS, 293, 257
- Browne, I.W.A., Wilkinson, P.N., Jackson, N.J.F. et al. 2003, MNRAS, 341, 13
- Burn, B.F. 1966, MNRAS, 133, 67
- Carilli, C.L., Menten, K.M., Reid, M.J. et al. 1998, ApJ, 494, 175
- Carvalho, J.C. 1985, MNRAS, 215, 463
- Carvalho, J.C., O'Dea, C.P. 2002, ApJS, 141, 371
- Chavushyan, V., Mujica, R., Gorshkov, A.G. et al. 2001, ARep, 45, 79
- Condon, J.J., Cotton, W.D., Greisen, E.W. et al. 1998, AJ, 115, 1693
- Conway, J.E., Blanco, P.R. 1995, ApJ, 449, 131
- Conway, J.E. 1996, IAUS, 175, 92
- Conway, J.E. 1999, NewAR, 43, 509
- Cotton, W.D., Dallacasa, D., Fanti, C. et al. 2003, PASA, 20, 12
- Dallacasa, D., Fanti, C., Fanti, R., Schilizzi, R.T., Spencer, R.E. 1995, A&A, 295, 27
- Dallacasa, D., Stanghellini, C., Centonza, M., Fanti, R. 2000, A&A, 363, 887

- Dallacasa, D., Falomo, R., Stanghellini, C. 2002, *A&A*, 382, 53
- Dallacasa, D., Venturi, T., Stanghellini, C. et al. 2005, *MemSAIt*, 76, 134
- Dallacasa, D., Falomo, R., Stanghellini, C. 2007, in preparation
- de Vries, W.H., Barthel, P.D., O’Dea, C.P. 1997, *A&A*, 321, 105
- De Young, D.S. 1993, *ApJ*, 402, 95
- Edge, A.C., Jones, M., Saunders, R., Pooley, G., Grainge, K. 1996, in *Proceedings of the Second Workshop on GPS and CSS Radio Sources*, ed. I.A.G. Snellen et al. (Leiden: Leiden Observatory), 208
- Edwards, P.G., Tingay, S.J. 2004, *A&A*, 424, 91
- Elitzur, M. 1992, *ARA&A*, 30, 75
- Emonts, B.H.C., Morganti, R., Tadhunter, C.N. et al. 2005, *MNRAS*, 362, 3
- Falle, S.A.E.G. 1991, *MNRAS*, 250, 581
- Fanaroff, B.L., Riley, J.M. 1974, *MNRAS*, 167, 31
- Fanti, R., Fanti, C., Schilizzi, R.T. et al. 1990, *A&A*, 231, 333
- Fanti, C., Fanti R., Dallacasa D. et al. 1995, *A&A*, 302, 31
- Fanti, C., Pozzi, F., Fanti, R. et al. 2000, *A&A*, 358, 499
- Fanti, C., Pozzi, F., Dallacasa, D., et al. 2001, *A&A*, 369, 380
- Fanti, C., Fanti, R. 2003, *ASPC*, 300, 81
- Fanti, C., Branchesi, M., Cotton, W.D. et al. 2004, *A&A*, 427, 465
- Ficarra, A., Grueff., G., Tomassetti, G. 1985, *A&AS*, 59, 255
- Forbes, O.A., Crawford, C.S., Fabian, A.C., Johnstone, R.M. 1990, *MNRAS*, 244, 680
- Forman, W., Jones, C., Tucker W. 1985, *ApJ*, 293, 102
- Gallimore, J.F., Baum, S.A., O’Dea, C.P., Pedlar, A., Brinks, E. 1999, *ApJ*, 524, 684
- Gilbert, J.A., Conway, R.G. *Nature*, 1970, 223, 1252
- Granato, G.L., Danese, L., Franceschini, A. 1997, *ApJ*, 486, 147
- Gregory, P.C., Condon, J.J. 1991, *ApJS*, 75, 1011
- Gregory, P.C., Scott, W.K., Douglas, K., Condon, J.J. 1996, *ApJS*, 103, 427
- Guainazzi, M., Siemiginowska, A., Rodriguez-Pascal, P., Stanghellini, C. 2004, *A&A*, 421, 461
- Guainazzi, M., Siemiginowska, A., Stanghellini, C. et al. 2006, *A&A*, 446, 87
- Gugliucci, N.E., Taylor, G.B., Peak, A.B., Giroletti, M. 2005, *ApJ*, 622, 136

- Gupta, N., Salter, C.J., Saikia, D.J., Ghosh, T., Jeyakumar, S. 2006, MNRAS, 373, 972
- Hatziminaoglou, E. et al. 2006, ASP Conference Series (astro-ph/0603359)
- Heckman, T.M., Smith, E.P., Baum, S.A., et al. 1986, ApJ, 311, 526
- Homan, D.C., Wardle, J.F.C. 1999, AJ, 118, 1942
- Humphrey, P.J., Buote, D.A., Gastaldello, F., et al. 2006, ApJ, 646, 899
- Jaffe, W.J., Perola, G.C. 1974, A&A, 26, 463
- Jenkins, C.M., Pooley, G.G., Riley, J.M. 1977, MmRAS, 84, 61
- Jeyakumar, S., Saikia, D.J., Pramesh Rao, A., Balasubramanian, V. 2000, A&A, 362, 27
- Jeyakumar, S., Wiita, P.J., Saikia, D.J., Hooda, J.S. 2005, A&A, 432, 823
- Kaiser, C.R., Alexander, P. 1997, MNRAS, 286, 215
- Kameno, S., Horiuchi, S., Shen, Z.-Q. et al. 2000, PASJ, 52, 209
- Kardashev, N.S. 1962, SvA, 6, 317
- Kellerman, K.I., Pauliny-Toth, I.I.K. 1981, ARA&A, 19, 373
- Kellermann, K.I., Vermeulen, R.C., Zensus, J.A., Cohen, M.H. 1998, AJ, 115, 1295
- Klein, U., Mack, K.-H., Gregorini, L., Vigotti, M. 2003, A&A, 406, 579
- Kudnic, T., Hogg, D.W., Blandford, R.D. et al. 1997, AJ, 114, 2276
- Kühr, H., Witzel, A., Pauliny-Toth, I.I., Nauber, U. 1981, A&AS, 45, 367
- Labiano, A., Vermeulen, R.C., Barthel, P.D. et al. 2006, A&A, 447, 481
- Laing, R.A., Riley, J.M., Longair, M.S. 1983, MNRAS, 204, 151
- Lockett, P., Gauthier, E., Elitzur, M. 1999, ApJ, 511, 235
- Marcha, M.J.M., Browne, I.W.A., Impey, C.D., Smith, P.S. 1996, MNRAS, 281, 425
- Marecki, A., Spencer, R.E., Kunert, M. 2003, PASA, 20, 46
- Marr, J.M., Taylor, G.B., Crawford, F. III 2001, ApJ, 550, 160
- McCarthy, P.J. 1993, ARA&A, 31, 639
- Mellema, G., Kurk, J.D., Röttgering, H.J.A. 2002, A&A, 395, 13
- Morganti, R., Oosterloo, T.A., Tadhunter, C.N. et al. 2001, MNRAS, 323, 331
- Morganti, R., Oosterloo, T.A., Tadhunter, C.N. et al. 2004, A&A, 424, 119
- Morganti, R., Tadhunter, C.N., Oosterloo, T.A. 2005, A&A, 444, 9
- Mundell, C.G., Wrobel, J.M., Pedlar, A., Gallimore, J.F. 2003, ApJ, 583, 192
- Murgia, M., Fanti, C., Fanti, R. et al. 1999, A&A, 345, 769
- Murgia, M. 2000, PhD Thesis

- Murgia, M. 2003, PASA, 20, 19
- Mutoh, M., Makoto, I., Kameno, S., et al. 2002, PASJ, 54, 131
- Miyoshi, M., Moran, J., Herrnstein, J., et al. 1995, Nature, 373, 127
- Norman, M. 1996, ASPC, 100, 405
- O'Dea, C.P., Baum, S.A., Stanghellini, C. 1991, ApJ, 380, 66
- O'Dea, C.P., Worrall, D.M., Baum, S.A., Stanghellini, C. 1996a, AJ, 111, 92
- O'Dea, C.P., Stanghellini, C., Baum, S.A., Charlot, S. 1996b, ApJ, 470, 806
- O'Dea, C.P., Baum, S.A. 1997, AJ, 113, 148
- O'Dea, C.P. 1998, PASP, 110, 493
- O'Dea, C.P., De Vries, W.H., Worrall, D.M., Baum, S.A., Koekemoer, A. 2000, AJ, 119, 478
- Orienti, M., Dallacasa, D., Fanti, C. et al. 2004, A&A, 426, 463
- Orienti, M., Dallacasa, D., Tinti, S., Stanghellini, C. 2006a, A&A, 450, 959
- Orienti, M., Morganti, R., Dallacasa, D. 2006b, A&A, 457, 531
- Orienti, M., Dallacasa, D., Stanghellini, C. 2007a, submitted to A&A
- Orienti, M., Dallacasa, D. 2007b, submitted to A&A
- Orienti, M., Dallacasa, D., Stanghellini C. 2007c, A&A, 461, 923
- Owsianik, I., Conway, J. 1998a, A&A, 337, 69
- Owsianik, I., Conway, J.E., Polatidis, A.G. 1998b, A&A, 336, 37
- Pacholczyk, A.G. 1970, Radio Astrophysics, Freeman & Co., San Francisco
- Patnaik, A.R., Browne, I.W.A., Wilkinson, P.N., Wrobel, J.M. 1992a, MNRAS, 254, 655
- Patnaik, A.R., Browne, I.W.A., Walsh, D. et al. 1992b, MNRAS, 259, 1
- Patnaik, A.R., Kembell, A.J., Porcas, R.W., Garrett, M.A. 1999, MNRAS, 307, 1
- Pauliny-Toth, I.I.K., Witzel, A., Preuss, E. et al. 1978, AJ, 83, 451
- Peck, A.B., Taylor, G.B., Conway, J.E. 1999, ApJ, 521, 103
- Peck, A.B., Taylor, G. B. 2000, ApJ, 534, 90
- Peacock, J.A., Wall, J.V. 1982, MNRAS, 198, 843
- Perley, R.A., Dreher, J.W., Cowan, J.J. 1984, ApJ, 285, 35
- Phillips, R.B., Mutel, R.L. 1982, A&A, 106, 21
- Pihlström, Y.M., Conway, J.E., Vermeulen, R.C. 2003, A&A, 404, 871
- Polatidis, A.G., Wilkinson, P.N., Xu, W., Readhead, A.C.S. et al. 1999, NewAR, 43, 657

- Polatidis, A.G., Conway, J.E. 2003, PASA, 20, 69
- Readhead, A.C.S. 1994, ApJ, 426, 51
- Readhead, A.C.S., Taylor, G.B., Pearson, T.J., Wilkinson, P.N. 1996, ApJ, 460, 634
- Rengelink, R.B., Tang, Y., de Bruyn, A.G., et al. 1997, A&AS, 124, 259
- Rossetti, A., Mantovani, F., Dallacasa, D., Fanti, C., Fanti, R. 2005, A&A, 434, 449
- Saikia, D.J., Salter, C.J. 1988, ARA&A, 26, 93
- Saikia, D.J., Jeyakumar, S., Salter, C.J., Thomasson, P., Spencer, R.E. 2001, MNRAS, 321, 37
- Saikia, D.J., Jeyakumar, S., Mantovani, F., et al. 2003, PASA, 20, 50
- Scheuer, P.A.G. 1974, MNRAS, 166, 513
- Shimmings, A.J., Searle, L., Andrew, B.H., Brandie, G.W. 1968, ApJ, 1, 167
- Siemiginowska, A., Cheung, C.C., LaMassa, S. et al. 2005, ApJ, 632, 110
- Snellen, I.A.G., Schilizzi, R.T., de Bruyn, A.G., et al. 1998, A&AS, 131, 435
301, 985
- Snellen, I.A.G., Schilizzi, R.T., Miley, G.K. et al. 2000, MNRAS, 319, 445
- Stanghellini, C., O’Dea, C.P., Baum, S.A., Laurikainen, E. 1993, ApJS, 88, 1
- Stanghellini, C., Bondi, M., Dallacasa, D., et al. 1997, A&A, 318, 376
- Stanghellini, C., O’Dea, C.P., Dallacasa, D. et al. 1998, A&AS, 131, 303
- Stanghellini, C., O’Dea, C.P., Murphy, D.W. 1999, A&A, 134, 309
- Stanghellini, C., Dallacasa, D., O’Dea, C.P., et al. 2001, A&A, 377, 377
- Stanghellini, C. 2003, PASA, 20, 118
- Stanghellini, C., O’Dea, C.P., Dallacasa, D. et al. 2005, A&A, 443, 891
- Stickel, M., Kühr, H. 1996, A&AS, 115, 11
- Tadhunter, C., Robinson, T.G., Gonzalez Delgado, R.M., Wills, K., Morganti, R. 2005, MNRAS, 356, 480
- Taylor, G.B., Readhead, A.C.S., Pearson, T.J. 1996, ApJ, 463, 95
- Tinti, S., Dallacasa, D., de Zotti, G., Celotti, A., Stanghellini, C. 2005, A&A, 432, 31
- Tinti, S., De Zotti, G. 2006, A&A, 445, 889
- Tribble, P.C. 1991, MNRAS, 250, 726
- Trinchieri, G., Fabbiano, G., Canizares, C.R. 1986, ApJ, 310, 637
- Urry, C.M., Padovani, P. 1995, PASP, 107, 803
- van Breugel, W., Miley, G., Heckman, T. 1984, AJ, 89, 5

Vermeulen, R.C., Pihlström, Y.M., Tschager, W. et al. 2003, *A&A*, 404, 861

Vigotti, M., GruEFF, G., Perley, R. et al. 1989, *AJ*, 98, 419

Vink, J., Snellen, I., Mack, K.-H., Schilizzi, R. 2006, *MNRAS*, 367, 928

Wakker, B., Oosterloo, T.A., Putman, M. 2002, *AJ*, 123, 1953

Wilkinson, P.N., Browne, I.W.A., Patnaik, A.R., et al. 1998, *MNRAS*, 300, 790

Xiang, L., Stanghellini, C., Dallacasa, D., Haiyan, Z. 2002, *A&A*, 385, 768